



A WIND TUNNEL INVESTIGATION OF  
JOINED WING SCISSOR MORPHING

THESIS

CHRISTOPHER DIKE, ENSIGN, USN

AFIT/GAE/ENY/06-J02

**DEPARTMENT OF THE AIR FORCE  
AIR UNIVERSITY**

**AIR FORCE INSTITUTE OF TECHNOLOGY**

**Wright-Patterson Air Force Base, Ohio**

APPROVED FOR PUBLIC RELEASE; DISTRIBUTION UNLIMITED

The views expressed in this thesis are those of the author and do not reflect the official policy or position of the United States Air Force, Department of Defense, or the United States Government.

AFIT/GAE/ENY/06-J02

A WIND TUNNEL INVESTIGATION OF  
JOINED WING SCISSOR MORPHING

THESIS

Presented to the Faculty

Department of Aeronautics and Astronautics

Graduate School of Engineering and Management

Air Force Institute of Technology

Air University

Air Education and Training Command

In Partial Fulfillment of the Requirements for the  
Degree of Master of Science in Aeronautical Engineering

Christopher Dike, BSME

Ensign, USN

June 2006

APPROVED FOR PUBLIC RELEASE; DISTRIBUTION UNLIMITED

AFIT/GAE/ENY/06-J02

A WIND TUNNEL INVESTIGATION OF  
JOINED WING SCISSOR MORPHING

Christopher Dike, BSME  
Ensign, USN

Approved:

---

Dr. Milton Franke (Chairman)

---

Date

---

Dr. Mark F. Reeder (Member)

---

Date

---

Lt Col Eric J. Stephen (Member)

---

Date

### **Abstract**

The Air Force Research Laboratory's Munitions Directorate has been looking to extend the range of its small smart bomb. Corneille [6] has conducted tests to determine the aerodynamic characteristics of joined wings on a missile and determine if joined wings are more beneficial than a single wing configuration. The concept of retrofitting wings on the bomb introduced an interesting problem: storage before deployment. This study conducted steady-state low speed wind tunnel testing of a joined wing configuration that morphed from a compact configuration for storage to a full extension. These steady-state tests examine differing sweep angles of the same joined wing configuration. The lift and drag as well as pitching moments and rolling moments were determined and analyzed for the effects of morphing.

*To my mother, father and brother for all their love and support throughout my life.*

## **Acknowledgements**

I would like to thank Dr. Franke for the encouragement, direction, and experience he shared with me. I would also like to thank Dr. Reeder for taking time out of his schedule to consult with me about data analysis. I would like to express my sincere gratitude to Dwight Gehring, AFIT/ENY, John Hixenbaugh, AFIT/ENY, and Jay Anderson, AFIT/ENY, for all of their help in this project. Mr. Gehring and Mr. Hixenbaugh conducted the set-up, calibration, and operation of the wind tunnel. Mr. Anderson deserves a vast amount of credit for the set-up and operation of the ENY rapid prototype machine.

## Table of Contents

	Page
Abstract.....	iv
List of Figures.....	ix
List of Tables .....	xiv
List of Symbols.....	xv
I. Introduction .....	1
Background.....	1
Current Studies .....	2
Problem Statement.....	3
II. Literature Review.....	5
Overview.....	5
Weight Reduction and Improved Structural Integrity .....	6
Lift .....	9
Drag .....	10
Stability & Control.....	11
Morphing Technologies.....	11
This Study .....	14
III. Experimental Equipment .....	15
The Missile Model .....	15
Wind Tunnel .....	22
Strain Gage Balance.....	25
Dantec Hot-wire Anemometer.....	26
IV. Experimental Procedures .....	27
Balance Calibration.....	27
Test Plan .....	27

	Page
Computation of Parameters .....	30
Lift.....	30
Drag.....	31
Pitching Moment.....	32
Rolling Moment .....	33
Compressibility Analysis .....	33
Tare .....	34
Blockage Correction .....	34
V. Results & Analysis.....	37
Wind Tunnel Blockage Correction .....	37
Wing Configuration Comparison.....	38
VI. Summary.....	58
Appendix A.....	59
Appendix B .....	92
Bibliography .....	109

## List of Figures

Figure	Page
Figure 1 No. 1737. Waco ASO (N4W c/n X3103). Photographed at Evergreen Airfield, Washington, August 2002 [20].	1
Figure 2 Compact and full positions of retrofit joined wings.	4
Figure 3 Negative stagger configuration using wing connectors [1].	5
Figure 4 Positive stagger configuration with wings connected to each other [21].	6
Figure 5 Single cantilever wing box versus joined wing structural box [23].	7
Figure 6 Fuel volume comparison [10].	8
Figure 7 Asymmetrical wing box [14].	8
Figure 8 Theoretic span efficiency factor for joined wings with or without symmetrical winglets [15].	11
Figure 9 Variable sweep on a general aircraft [13].	12
Figure 10 Wing sweep mechanism [13].	13
Figure 11 Wright Brothers' 1899 Wright Kite wing warping design [8].	14
Figure 12 Bare missile model in the wind tunnel.	15
Figure 13 Five wing configurations of 30° swept wing morphing from 90°, against the body, to 30° full extension.	16
Figure 14 Profile for all the swept wings.	18
Figure 15 This diagram shows the difference between the profile and the chord.	18
Figure 16 The 90° swept wing showing the wing gap of 2 inches.	19
Figure 17 Top profile of the five wing morphing configurations of the 30° swept wing.	20
Figure 18 Different view of the five wing morphing configurations of the 30° swept wing.	21
Figure 19 Wind tunnel convergence dimensions [11].	23

	Page
Figure 20 AFIT 3' x 3' wind tunnel schematic [11]. .....	24
Figure 21 Test Section of tunnel from Figure 20 with the tunnel axis as defined by the hot-wire traverse grid. [9] .....	24
Figure 22 Comparison between the 60° swept plastic and aluminum wings.....	28
Figure 23 Wind axis and body axis forces.....	31
Figure 24 Diagram of lifting forces on the missile.....	33
Figure 25 Shows placement of hotwire anemometer [16]. .....	35
Figure 26 Hotwire test pattern [9].....	36
Figure 27 Hotwire vs. transducer velocity measurements.....	37
Figure 28 Comparison between Corneille [6] and this study's results for the 30° joined wing made of aluminum. .....	39
Figure 29 Lift and drag relations of the 60° joined wing, not morphed, aluminum. ....	40
Figure 30 Comparison of 30° joined wing, plastic and aluminum at 60 mph. .....	42
Figure 31 Comparison of 30° joined wing, plastic and aluminum at 80 mph. .....	42
Figure 32 Comparison of 30° joined wing, plastic and aluminum at 100 mph. .....	43
Figure 33 Comparison of 30° joined wing, plastic and aluminum at 130 mph. .....	43
Figure 34 Comparison of 30° joined wing, plastic and aluminum at 145 mph. .....	44
Figure 35 Lift comparison of the morphing wing set at 60 mph. .....	45
Figure 36 Lift comparison of the morphing wing set at 80 mph. .....	46
Figure 37 Lift comparison of the morphing wing set at 100 mph. .....	46
Figure 38 Lift comparison of the morphing wing set at 130 mph. .....	47
Figure 39 Lift comparison of the morphing wing set at 145 mph. .....	47
Figure 40 Drag comparison of the morphing wing set at 60 mph. .....	48

Figure 41 Drag comparison of the morphing wing set at 80 mph. ....	49
Figure 42 Drag comparison of the morphing wing set at 100 mph. ....	49
Figure 43 Drag comparison of the morphing wing set at 130 mph. ....	50
Figure 44 Drag comparison of the morphing wing set at 145 mph. ....	50
Figure 45 Comparison of 60° joined wing plastic morphed and the aluminum at 60 mph. ....	52
Figure 46 Comparison between two runs on the 60° plastic morphed wing testing for repetition at 145 mph. ....	53
Figure 47 Pitching moment comparison of the morphing wing set at 60 mph.....	54
Figure 48 Pitching moment comparison of the morphing wing set at 80 mph.....	55
Figure 49 Pitching moment comparison of the morphing wing set at 100 mph.....	55
Figure 50 Pitching moment comparison of the morphing wing set at 130 mph.....	56
Figure 51 Pitching moment comparison of the morphing wing set at 145 mph.....	56
Figure 52 Rolling Moment versus angle of Attack for 30° swept, plastic joined wing....	57
Figure 53 Lift and drag relations of the bare missile. ....	60
Figure 54 Drag relations of the bare missile. ....	61
Figure 55 Lift and drag Relations of 30° swept single wing located forward of CG, wings on bottom, aluminum. ....	62
Figure 56 Drag and pitch relations of the 30° swept single wing located forward of the CG, wings on bottom, aluminum. ....	63
Figure 57 Lift and drag relations of the 30° swept single wing located forward of the CG, wings on bottom, plastic. ....	64
Figure 58 Drag and pitch relations of the 30° swept single wing located forward of the CG, wings on bottom, plastic.....	65
Figure 59 Lift and drag relations of 30° swept single wing located aft of CG, wings on top, aluminum. ....	66

	Page
Figure 60 Drag and pitch relations of the 30° swept single wing located aft of CG, wings on top, aluminum .....	67
Figure 61 Lift and drag relations of the 30° swept single wing located aft of CG, wings on top, plastic .....	68
Figure 62 Drag and pitch relations of the 30° swept single wing located aft of CG, wings on top, plastic .....	69
Figure 63 Lift and drag relations of 30° swept joined wing, aluminum .....	70
Figure 64 Drag and pitch relations of the 30° joined wing, aluminum.....	71
Figure 65 Lift and drag relations of 30° swept joined wing, plastic.....	72
Figure 66 Drag and pitch relations of the 30° joined wing, plastic.....	73
Figure 67 Lift and drag relations of the 45° single wing swept forward, plastic.....	74
Figure 68 Drag and pitch relations of the 45° single wing swept forward, plastic.....	75
Figure 69 Lift and drag relations of the 45° joined wing, plastic. ....	76
Figure 70 Drag and pitch relations of the 45° joined wing, plastic.....	77
Figure 71 Lift and drag relations of the 60° joined wing, plastic. ....	78
Figure 72 Drag and pitch relations of the 60° joined wing, plastic.....	79
Figure 73 Lift and drag relations of the 60° joined wing, plastic. Second Run. ....	80
Figure 74 Drag and pitch relations of the 60° joined wing, plastic. Second Run. ....	81
Figure 75 Lift and drag relations of the 60° joined wing, not morphed, aluminum. ....	82
Figure 76 Drag and pitch relations of the 60° joined wing, not morphed, aluminum. ....	83
Figure 77 Lift and drag relations of the 75° joined wing, plastic. ....	84
Figure 78 Drag and pitch relations of the 75° joined wing, plastic.....	85
Figure 79 Lift and drag relations of the 90° joined wing, plastic. ....	86

Figure 80 Drag and pitch relations of the 90° joined wing, plastic.....	87
Figure 81 Comparison of 60° joined wing between plastic morphed and the aluminum at 80 mph. ....	88
Figure 82 Comparison of 60° joined wing between plastic morphed and the aluminum at 100 mph. ....	88
Figure 83 Comparison of 60° joined wing between plastic morphed and the aluminum at 130 mph. ....	89
Figure 84 Comparison of 60° joined wing between plastic morphed and the aluminum at 145 mph. ....	89
Figure 85 Comparison between two Runs on the 60° plastic morphed wing testing for repetition at 60 mph. ....	90
Figure 86 Comparison between two Runs on the 60° plastic morphed wing testing for repetition at 80 mph. ....	90
Figure 87 Comparison between two Runs on the 60° plastic morphed wing testing for repetition at 100 mph. ....	91
Figure 88 Comparison between two Runs on the 60° plastic morphed wing testing for repetition at 130 mph. ....	91
Figure 89 Comparison of L/D vs Alpha for the 30° Joined wing and Single wings at 60 mph. ....	92
Figure 90 Comparison of L/D vs Alpha for the 30° Joined wing and Single wings at 80 mph. ....	92
Figure 91 Comparison of L/D vs Alpha for the 30° Joined wing and Single wings at 100 mph. ....	93
Figure 92 Comparison of L/D vs Alpha for the 30° Joined wing and Single wings at 130 mph. ....	93
Figure 93 Comparison of L/D vs Alpha for the 30° Joined wing and Single wings at 145 mph. ....	94

## List of Tables

Table	Page
Table 1 Various parameters of the model configurations.....	17
Table 2 Fan and motor specifications [11]. .....	22
Table 3 Maximum loads of AFIT's 25 lb balance.....	25
Table 4 Model Test Configurations .....	29
Table 5 Difference in velocity between the transducer and hotwire. ....	37

## List of Symbols

a – Distance from the force  $N_1$  to the center of gravity

A – Axial force

AR – Aspect ratio

AR<sub>F</sub> – Aspect ratio of front wing

AR<sub>R</sub> – Aspect ratio of rear wing

b – Span; Distance from the force  $N_2$  to the center of gravity

c – Chord

C<sub>D</sub> – Drag coefficient

C<sub>Di</sub> – Induced drag coefficient

C<sub>Do</sub> – Incompressible drag coefficient

CG – Center of gravity

C<sub>L</sub> – Lift coefficient

C<sub>Lmax</sub> – Maximum lift coefficient

C<sub>Lo</sub> – Incompressible lift coefficient

C<sub>M,0</sub> – Initial pitching moment coefficient

C<sub>M</sub> – Pitching moment coefficient

D – Drag

e – Span efficiency factor

h – Maximum distance between joined wings

L – Lift

L' – Rolling moment

M – Pitching moment

$M_\infty$  - Free stream Mach number

$N$  – Total normal force

$N_1$  – Normal force measured at location 1

$N_2$  – Normal force measured at location 2

$Re$  – Reynolds number

$S$  – Reference area

$S_F$  – Area of the front wing

$S_R$  – Area of the rear wing

$U_{OT}$  – Free stream velocity, Open tunnel

$U_{Tr}$  – Free stream velocity, Transducer (Beginning of tunnel)

$V_\infty$  - Free stream velocity

$\alpha$  – Angle of attack

$\varepsilon_{tc}$  – Total blockage

$\Lambda_{LE}$  – Sweep angle of the leading edge of the wing

$\rho_\infty$  – Free stream density

$X$  – Tunnel axis coordinate

$Y$  – Tunnel axis coordinate

$Z$  – Tunnel axis coordinate

# A WIND TUNNEL INVESTIGATION OF JOINED WING SCISSOR MORPHING

## I. Introduction

### Background

Multiple lifting surfaces provide more lift over the single lifting surface concept. Early biplanes are a perfect example. The multiple wings gave more lifting surfaces and thus more lift, but the draw back was more profile drag. This profile drag came from the struts and wires, which can be seen in Figure 1. These struts and wires give the multiple wings extra support which would void the lifting benefits gained. The concept of multiple wings lost favor as structural technology advanced [3].



**Figure 1 No. 1737. Waco ASO (N4W c/n X3103). Photographed at Evergreen Airfield, Washington, August 2002 [20].**

The lift to drag ratio is a very important ratio in considering the aircraft's aerodynamic efficiency. The higher the lift to drag ratio, the farther the aircraft can fly or

more weight it can carry for the same amount of fuel used. Structural advancements led to the single wing cantilever wing being dominantly used in aircraft over the last few decades. Cantilever wings remove more profile drag than the lift that is lost due to less lifting surfaces which results in a higher lift to drag ratio.

Due to continuing structural advancement, the idea of multiple wings is resurfacing. The joined wing idea, specifically, is more structurally sound with less profile drag and induced drag. With the proper design, the joined wing configuration can weigh less than its single wing counter part if constrained by same lift to drag ratio [3]. In addition to the aerodynamic improvements, there are more control surfaces which give more control to the aircraft.

## **Current Studies**

The concept of multiple wings began resurfacing in the early 1980s with the studies and patents of Wolkovitch [22]. Many studies are being done by companies such as Boeing and Lockheed Martin, to put the benefits of the joined wing concept to use. Boeing has a joined wing design that could replace the Navy's E-2C Hawkeye. Tests have been conducted in a LaRC 16 foot transonic wind tunnel [6]. Lockheed Martin has proposed a new joined wing tanker design with two booms. The purpose is to carry more fuel per tanker and reduce the amount of tankers needed to refuel aircraft [6]. CFD programs have also been developed to analyze joined wing designs [15].

The Air Force Research Laboratory (AFRL) Munitions Division would like to extend the range of smart bombs to allow the delivery aircraft to deploy the missile from a much safer distance from the enemy defenses [6].

The Air Force Institute of Technology (AFIT) has conducted an investigation on a missile model with joined wings to see if the added benefits would be better than adding cantilever wings to the missile.

## **Problem Statement**

Tests conducted by Corneille [6] showed that joined wing configurations increase range by 30% or more. The difficulty with wings on missiles is the carriage ability of the aircraft that delivers the missile. Wings increase the area required for storage. This is unacceptable. The wings need to be able to morph, or change shape, to take up less space in storage. When these missiles are dropped from the delivery aircraft, the wings will then morph from their compact position against the missile body to their extended position. One concept that this study will look at is the scissors morph. The scissors morph maintains the connecting points to the missile rather than having moveable connection points. This should simplify the design because the morphing will be contained solely in the wings that are attached. There are four axis points. Two of the axis points where the wings connect to the missile and two moving axis points that are the wing connectors, shown in Figure 2. As the wings swing out from the missile body, the wing connectors will move along the centerline to each of the wing's wingtips. This study will look at the effects this morphing, or change in configuration, will have on lift, drag and stability of the missile.

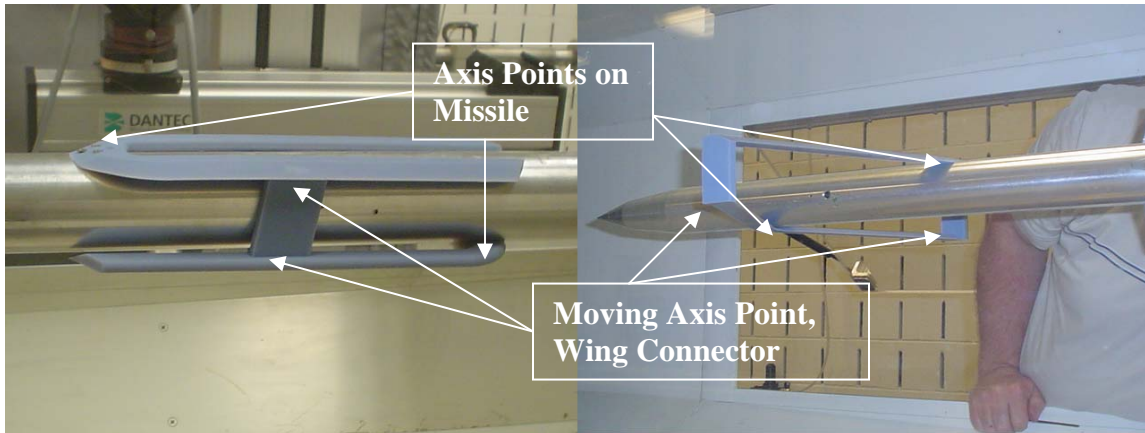


**Figure 2 Compact and full positions of retrofit joined wings.**

## **II. Literature Review**

This section reviews previous tests and inspections, one of which is Corneille's [6] investigation because this is a direct follow-on to her work.

### **Overview**

Wolkovitch stated that, "the joined-wing airplane may be defined as an airplane that incorporates tandem wings arranged to form diamond shapes in both plan and front views" [23]. There are many configurations that will achieve this definition. One configuration is known as negative stagger. It attaches the front wing forward and low on the fuselage and swept back. The aft wing is attached back and high on the fuselage. The wings then can be joined together by having wing connectors, structural components for rigidity, or by having dihedral on both wings such that they attach directly to each other. Figure 3 shows this negative stagger configuration with wing connectors.



**Figure 3 Negative stagger configuration using wing connectors [1].**

The wing configuration known as positive stagger switches the forward wing from the bottom of the fuselage to the top of the fuselage and the aft wing from the top to the bottom of the fuselage. Figure 4 shows the positive stagger configuration with the dihedral for them to directly connect to each other without wing connectors.



**Figure 4 Positive stagger configuration with wings connected to each other [21].**

The joined wing has many claimed advantages over the single wing cantilever that is currently used for almost every aircraft. Some of these advantages include lighter weight, higher stiffness, higher  $C_L$  max, lower drag, and good stability and control [23].

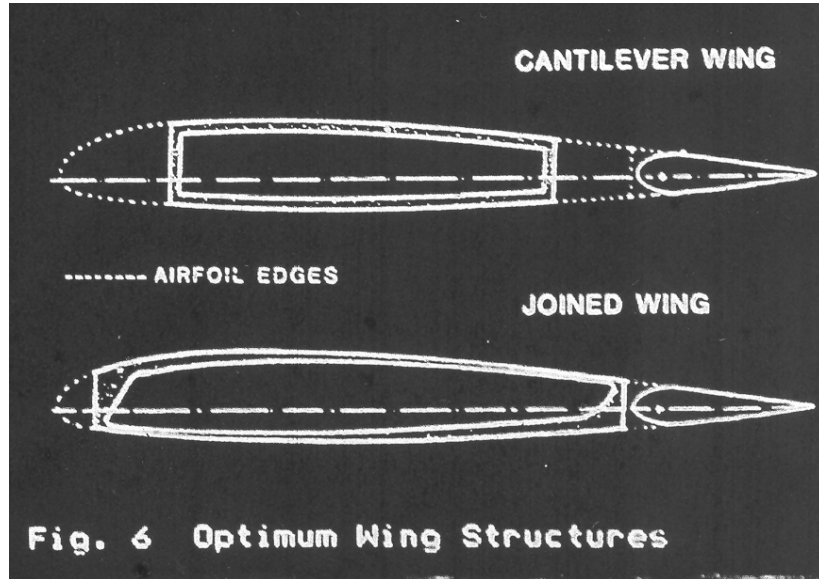
### **Weight Reduction and Improved Structural Integrity**

Studies have shown that the joined wing configurations with the same projected areas, sweep angles, and taper ratios give large weight savings over their single wing counterpart [23]. The joined wing configuration can be 65% to 78% lighter in comparison to the single wing [10, 23].

It is important to note that to achieve this weight savings over the single wing, the geometric parameters must be properly chosen and the internal wing structure must be optimized [23]. The wing box must occupy the section of the airfoil between 5% and 75% of the chord [23]. Typically the wing box only extends from 15% to 65% of the

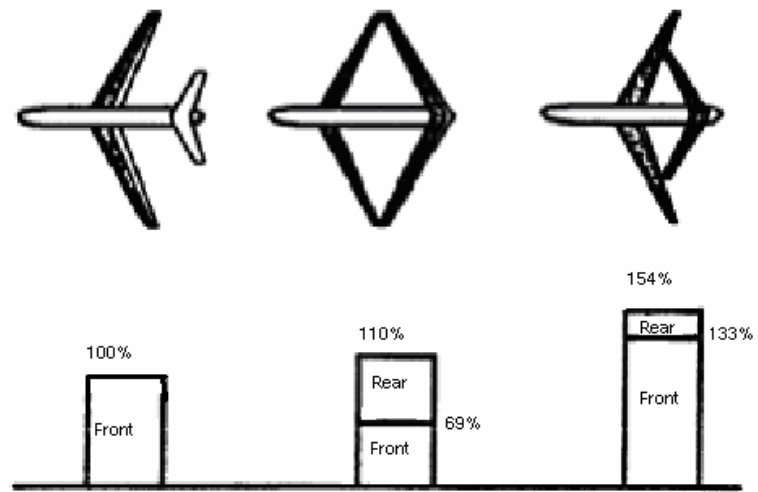
chord because of the need for larger skin thickness to increase structural integrity [23].

Figure 5 shows the wing box comparison between the cantilever single wing and the joined wing.



**Figure 5 Single cantilever wing box versus joined wing structural box [23].**

The larger wing box for the joined wing configuration is possible because of the increased structural integrity the box shape gives the wings. This allows for less skin thickness and thus a larger wing box. A larger wing box and multiple wings also means more fuel capacity as shown in Figure 6.



**Figure 6 Fuel volume comparison [10].**

The box shape of the wings not only adds rigidity to the structure but also resists longitudinal and vertical loads [18]. Studies show that the most desired arrangement for a joined wing box is asymmetric, putting more material in the corners that need it to resist bending [14]. The asymmetric box is shown in Figure 7.

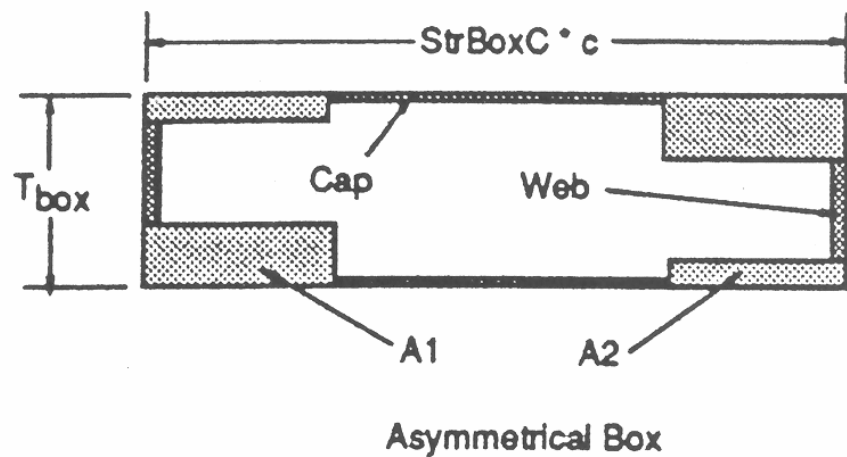


**Figure 7 Asymmetrical wing box [14].**

The joined wing structure is much more complex than its single wing counterpart. Selberg and Cronin [21] have found that the structural complexity of joined wings leads to an increased number of natural frequencies that produce modes of vibration containing an unexplainable variety of behaviors.

Tests have also shown that adding cant and twist to the wings can achieve even higher aerodynamic efficiencies [3]. Again, any improvements that the joined wing configurations show are dependent on the proper wing properties being chosen, such as placement, span, and surface area.

## Lift

One of the advantages noted earlier is the higher  $C_L$  max the joined wing configuration has at trimmed flight [23]. In the joined wing configuration, the front wing has a tendency to stall, or reaches its  $C_L$  max at lower angles of attack than the rear wing [23]. This condition gives the joined wing very good recovery properties, but it is undesirable because it doesn't fully utilize the potential lifting capability of the rear wing. If the rear wing is not reaching its  $C_L$  max, it is oversized, meaning excess weight that is not being utilized [23]. It is ideal to have a joined wing design that the front wing stalls when the rear wing stalls [23]. While this improves efficiency it also decreases the wetted area while maintaining the same lifting properties [23]. Decreasing the area can also extend the range since range is a function of lift and drag [2, 4].

Joined wing configurations allow for variation depending on the mission at hand. They can maintain the same flying weight as a single wing by lengthening the span or chord, and still have better lifting properties. The joined wing can also carry heavier loads than the single wing with the same lifting properties [23].

Joined wing configurations induce camber. This is caused by the flow being curved and varies based upon gap and stagger angles [7, 22, 23]. When the single wing is compared to the joined wing using the same airfoil, the joined wing has shown premature flow detachment [22]. Specifically for missiles, variable camber has been recommended for best performance. The camber needs to be reduced to maintain the highest possible lift to drag, which will maximize the range [22].

## **Drag**

As mentioned in the Introduction, biplanes had a high profile drag issue due to the extensive structural wiring. Joined wings actually have lower total drag than single wing configurations. This is due to the lower induced drag than the single wing counterpart at equal lift, span, and dynamic pressure [2, 14, 18, 22, 23]. This is true for two reasons. The first reason is that sweeping wings increase induced drag. Although, swept wings that have the same aspect ratio as straight wings also have the same induced drag provided the lift distribution is the same [10, 18, 22, 23]. The second reason is the Prandtl-Munk biplane theory shows that the span efficiency factor can be greater than one for biplanes [10, 18, 22, 23]. This theory actually predicts efficiency factors for joined wings to be much lower than wind tunnel tests have shown [22, 23]. For this reason, Kuhlman and Ku developed a program, summarized by Figure 8, which accurately predicts the efficiency factor for joined wings [15]. This is important because the higher the efficiency factor, the lower the induced drag.

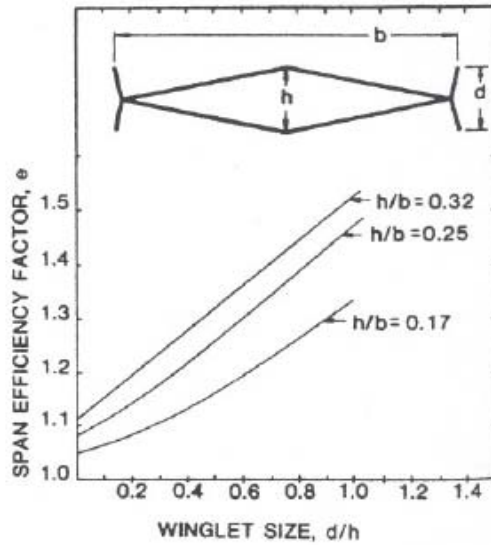


**Figure 8** Theoretic span efficiency factor for joined wings with or without symmetrical winglets [15].

## Stability & Control

Joined wings have four controlling surfaces where the single wing configuration has only two controlling surfaces. More control surfaces mean more control and stabilizing surfaces. More control leads to better maneuverability [22]. Joined wings have good spiral stability and no Dutch roll, but do have some pitch down when at high lift coefficients [22]. Wolkovitch [23] found that adding strakes reduces this pitch down and increases the maximum lift coefficient.

## Morphing Technologies

Traditionally, when wings change sweep they are considered variable sweep. This definition generally refers to aircraft that have wings at one sweep for flight at low Mach numbers and another for Mach numbers near and above one. An example is shown in Figure 9. The F-14, used for decades by the US Navy, uses this technology. It would use the low sweep for carrier landing and subsonic cruise, and use the high sweep for

supersonic flight [13]. According to Raymer [19], variable sweep has a weight penalty in that the mission might not be acceptable in comparison to the benefits.

An example of a specific variable wing system mechanism for the XF10F-1 is shown in Figure 10. The wings translate forward at their base and also pivot in when increasing the wing sweep [13]. This mechanism was considered trouble free by Kress [13].

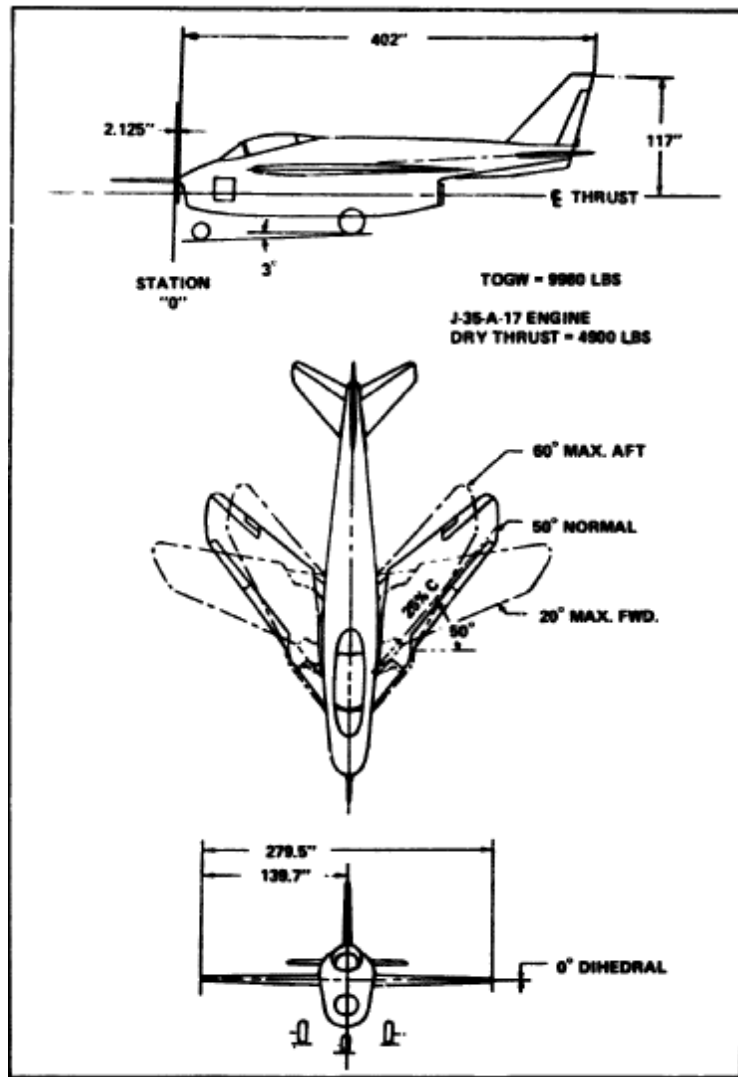


**Figure 9 Variable sweep on a general aircraft [13].**

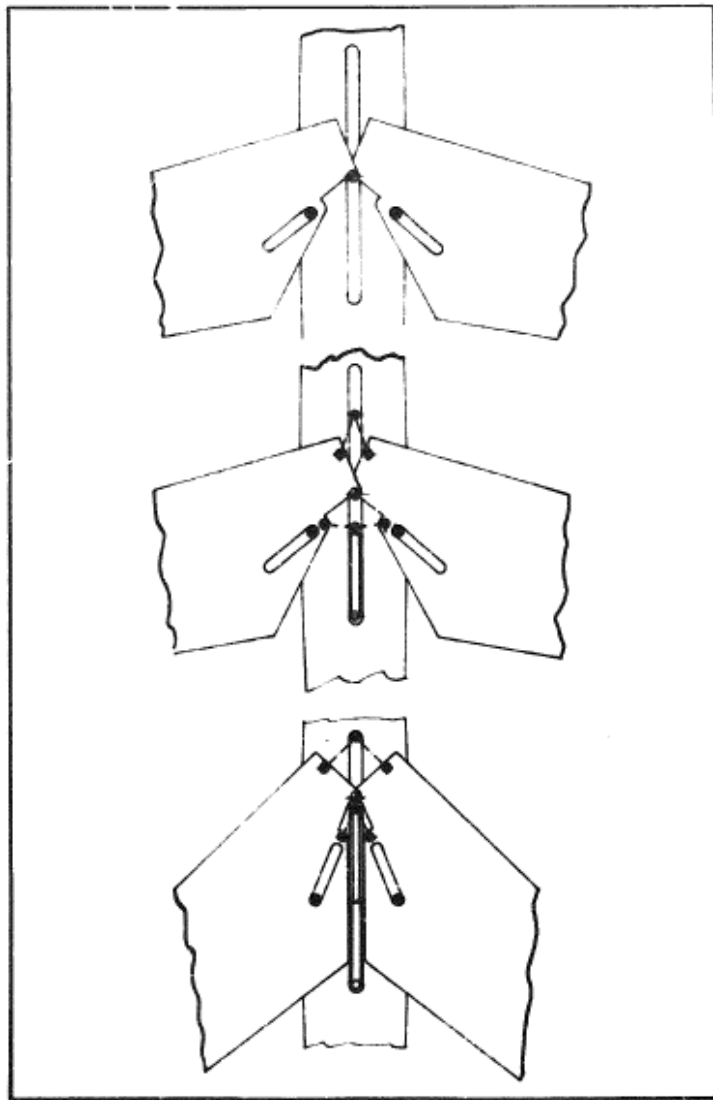


**Figure 10** Wing sweep mechanism [13].

According to Guiler and Huebsch [8], wing morphing is defined as camber control and can be traced back to the Wright Brothers Wright Kite shown in Figure 11. This glider used a flexible structure and a special weave to warp correctly when actuator cables were pulled [8]. Camber control is the ability to change the camber of the wing as needed for the best wing performance [8].

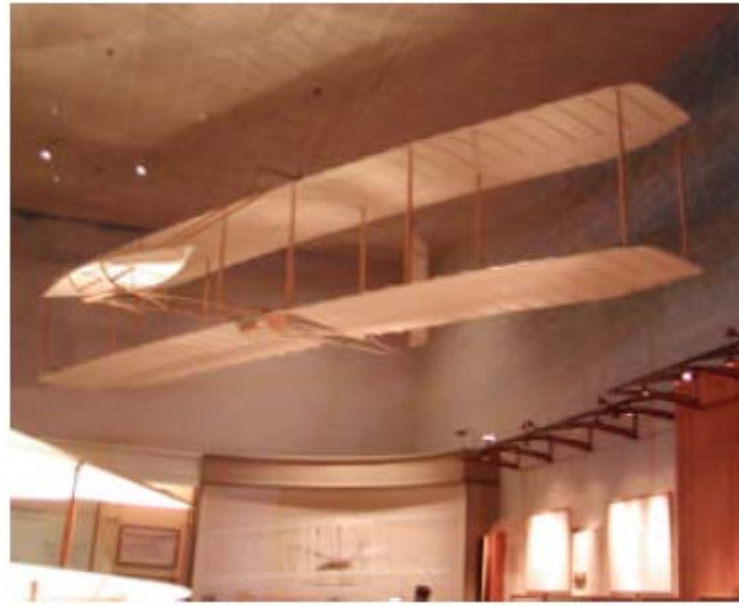


**Figure 11 Wright Brothers' 1899 Wright Kite wing warping design [8].**

### This Study

Morphing for this study will be defined as wing extension. Camber will remain a constant. The wings will start in the closed position along the fuselage body, a sweep of 90 degrees, and will morph to the full extension after being dropped. This is different from variable sweep which has multiple wing positions to optimize the flight conditions as required during flight. The wings in this study cannot. They only change once, from the position that meets storage restraints to the fully extended position for flight.

### **III. Experimental Equipment**

This section describes the equipment and preparation for this study.

#### **The Missile Model**

The missile model shown in Figure 12, is made of aluminum, is 28.44 in (0.72 m) long, and has a projected diameter of 2 in (0.0508 m). The missile has four identical tail fins, two horizontal and two vertical, to give the missile maneuverability and stability in flight. The airfoil of the tail is symmetric.



**Figure 12 Bare missile model in the wind tunnel.**

For this study, there are five sweep variations that are all variations of the 30-degree swept wing with negative stagger. This particular configuration was chosen because Corneille [6] found that negative stagger was better than positive stagger and the 30 degrees allowed for a wide range of sweep variations. The 30-degree swept wing starts at 90 degrees, or against the missiles body, and swings out to the 30 degrees swept

point. There were  $15^\circ$  intervals used giving wing configurations at 90, 75, 60, 45, and 30 degrees. Figure 13 shows the five wing configurations of the 30-degree wing morphing from 90 degrees, against the body, to full extension.

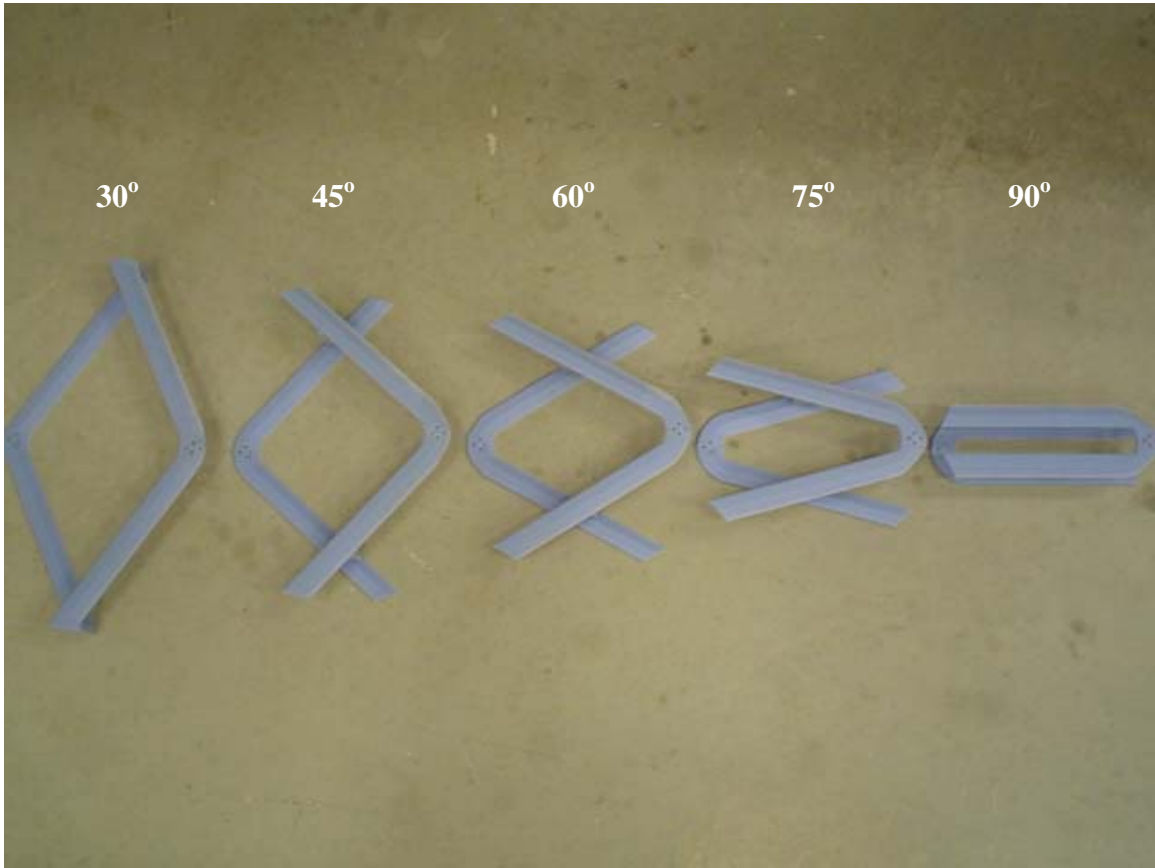


**Figure 13 Five wing configurations of  $30^\circ$  swept wing morphing from  $90^\circ$ , against the body, to  $30^\circ$  full extension.**

These wings are made of plastic. They were designed in SolidWorks, based upon the specifications of the aluminum 30-degree swept wing and modified to simulate morphing. The wings were then made in AFIT's rapid prototype machine. Table 1 gives the weight, span, reference area, and aspect ratio for the configurations of this study. The reference area for the bare missile is the projected area and wing planform area for the

winged configurations. The aspect ratios and efficiency factors are calculated using equations that will be discussed later.

**Table 1 Various parameters of the model configurations.**

	Weight	Span	Reference Area	Aspect Ratio
Bare Model	6.85 lbm (3.11 kg)	N/A	N/A	N/A
30° Swept Joined Wing Aluminum	7.62 lbm (3.46 kg)	15.588 in (0.396 m)	0.265 ft <sup>2</sup> (0.0246 m <sup>2</sup> )	7.79
30° Swept Joined Wing Plastic	7.2 lbm (3.266 kg)	15.588 in (0.396 m)	0.265 ft <sup>2</sup> (0.0246 m <sup>2</sup> )	7.79
45° Swept Joined Wing Plastic	7.2 lbm (3.266 kg)	13.44 in (0.341m)	0.265 ft <sup>2</sup> (0.0246 m <sup>2</sup> )	6.72
60° Swept Joined Wing Aluminum	7.67 lbm (3.48 kg)	10.6 in (0.8833 m)	0.265 ft <sup>2</sup> (0.0246 m <sup>2</sup> )	4.50
60° Swept Joined Wing Plastic	7.2 lbm (3.266 kg)	10.6 in (0.8833 m)	0.265 ft <sup>2</sup> (0.0246 m <sup>2</sup> )	4.50
75° Swept Joined Wing Plastic	7.2 lbm (3.266 kg)	7.10 in (0.5917 m)	0.265 ft <sup>2</sup> (0.0246 m <sup>2</sup> )	3.55
90° Swept Joined Wing Plastic	7.2 lbm (3.266 kg)	3.18 in (0.265 m)	0.265 ft <sup>2</sup> (0.0246 m <sup>2</sup> )	1.59
30° Swept Single Wing Aluminum	7.12 lbm (3.23 kg)	15.588 in (0.396 m)	0.133 ft <sup>2</sup> (0.012 m <sup>2</sup> )	12.69
30° Swept Single Wing Plastic	6.99 lbm (3.17 kg)	15.588 in (0.396 m)	0.133 ft <sup>2</sup> (0.012 m <sup>2</sup> )	12.69

The airfoil profile is shown in Figure 14 where the length is 1 in (0.0254 m) for all wings. There is no twist or dihedral for any of these wings and there is a wing gap between the joined wings of 2 in (0.0508 m), the diameter of the missile. The wing gap is shown in Figure 16. The chord length of all the wings is 1.375 in (0.034925 m). This is different from the length of the profile because the profile is not parallel to the missile where the chord length is parallel shown in Figure 15. This airfoil has positive camber, which consequently causes a negative  $C_{M,0}$  that is not desirable [17]. Because the

aerodynamics of a positive camber wing is desirable, a tail is usually required to make  $C_{M,0}$  positive [17].

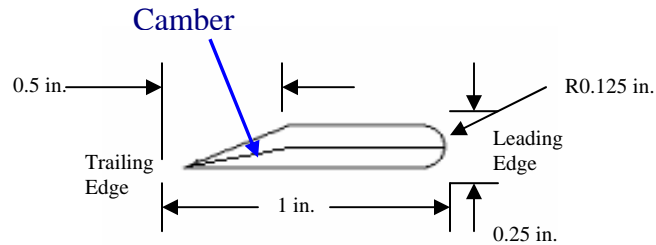


**Figure 14 Profile for all the swept wings.**

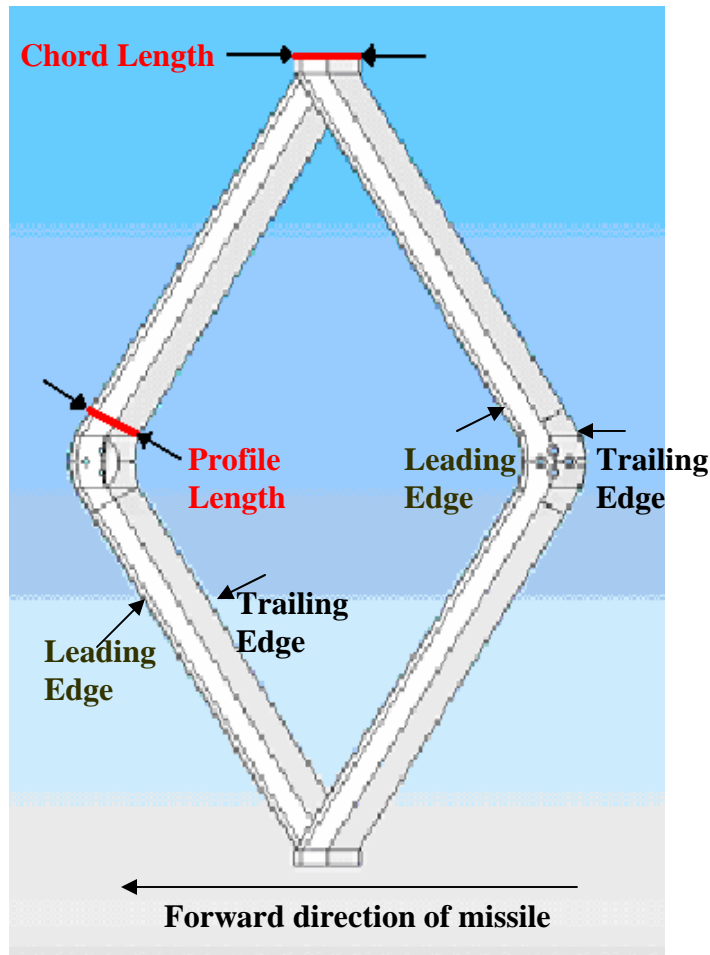


**Figure 15 This diagram shows the difference between the profile and the chord.**

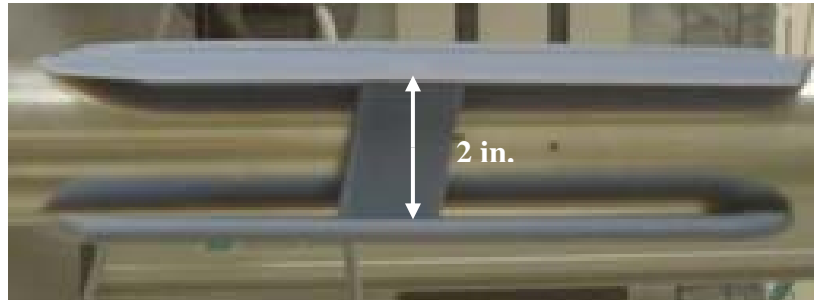


**Figure 16** The 90° swept wing showing the wing gap of 2 inches.

The wing connectors are mounted parallel to the missile, i.e. chord length of the wing. Originally, there were two types of wing connectors tested: curved and straight. Corneille [6] found no distinct difference between the effects of either. For this study, only the straight connector was used to reduce the variables. The wing connector is also a moving body in this study. The wing connector moves towards the wingtips as the wings morph to their full extension, as seen in Figure 17 and Figure 18. Also notice how the wing tips are changing between sweeps.

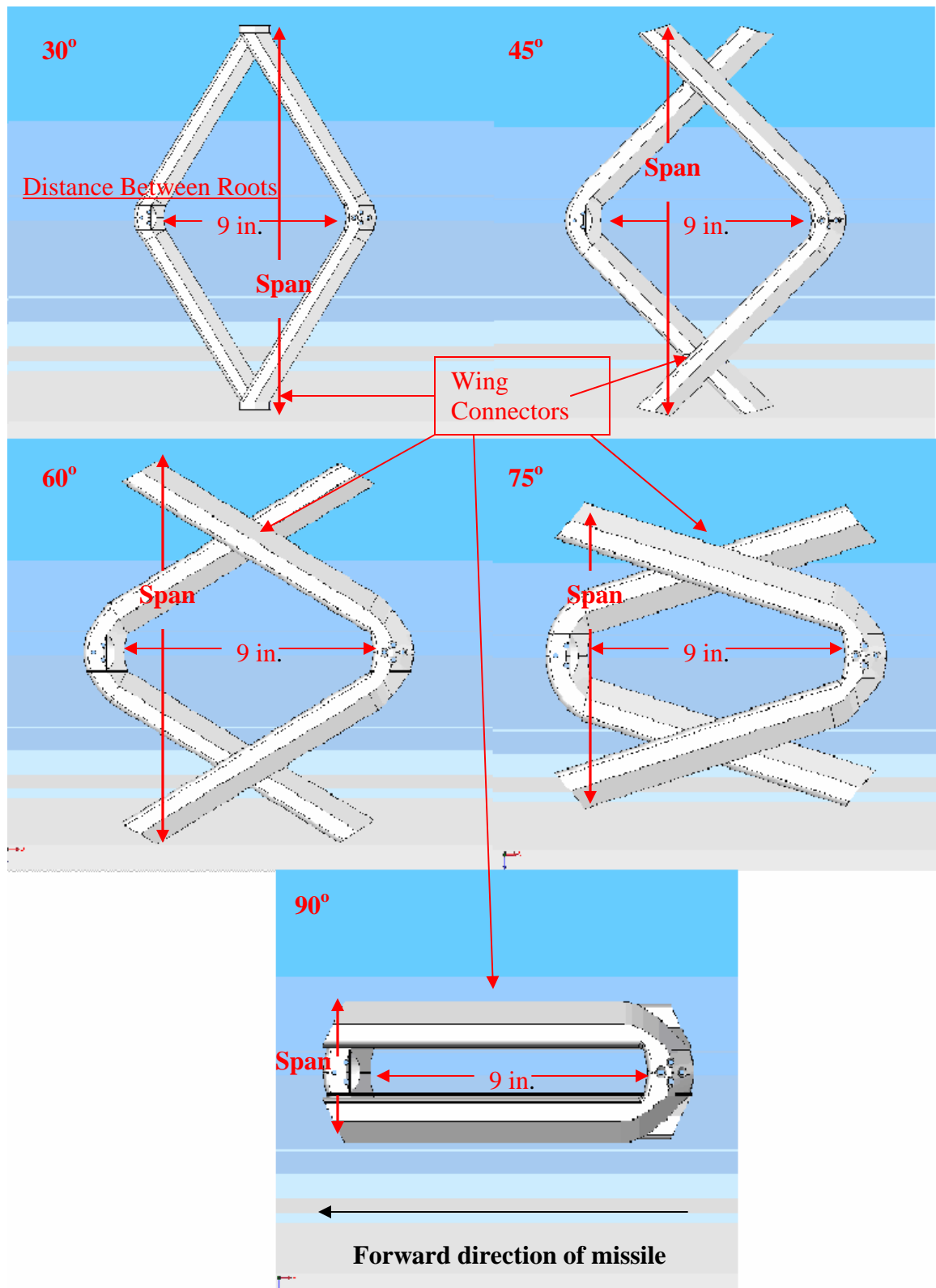


**Figure 17** Top profile of the five wing morphing configurations of the 30° swept wing.

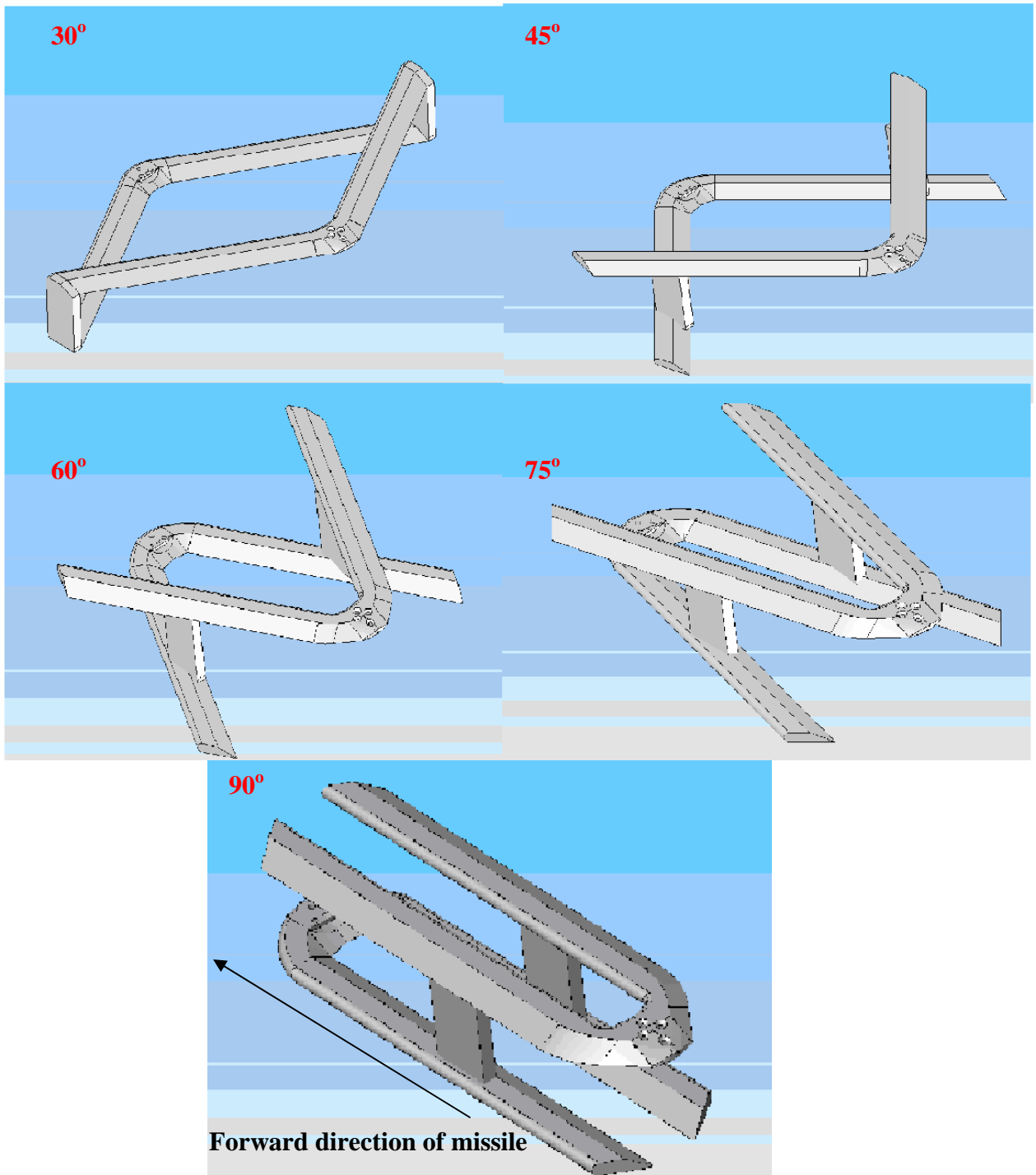


**Figure 18** Different view of the five wing morphing configurations of the 30° swept wing.

## Wind Tunnel

Experiments were conducted in the AFIT 3'x3' subsonic wind tunnel, built by the New York Blower Company. The wind tunnel fan is an ACF/PLR Class IV with a Toshiba Premium Efficiency (EQP III) fan motor. The fan and the motor are both controlled by a Siemens (13710) Adjustable Frequency Tunnel Controller. Table 2 shows the specifications.

**Table 2 Fan and motor specifications [11].**

Controller	Motor
	3 phase induction
	1785 RPM operating speed
	Maximum theoretical speed – 150 mph
	Maximum tested speed – 148 mph
250 max HP	200 brake horsepower
460 volts	230/460 volts
315 amps	444/222 amps
	60 Hz
	4 poles

The tunnel is an open circuit configuration with a closed test section. The fan is located at the end of the tunnel and pulls the ambient air from the room through a 122" w x 111" h x 70" l intake plenum. To give the tunnel good laminar streamlines, the plenum consists of four steel mesh anti-turbulent screens with  $\frac{1}{4}$ " aluminum honeycomb flow-straightener which has a minimum aspect ratio of 15. The flow travels to the test section

through a 95.5" long convergent duct with a contraction ratio of 9:5:1. The height of the tunnel contracts from the anti-turbulent screen at 111" to the test section of height 31.5". Figure 19 displays the wind tunnel convergence dimensions. Figure 20 displays the schematic of AFIT's wind tunnel.

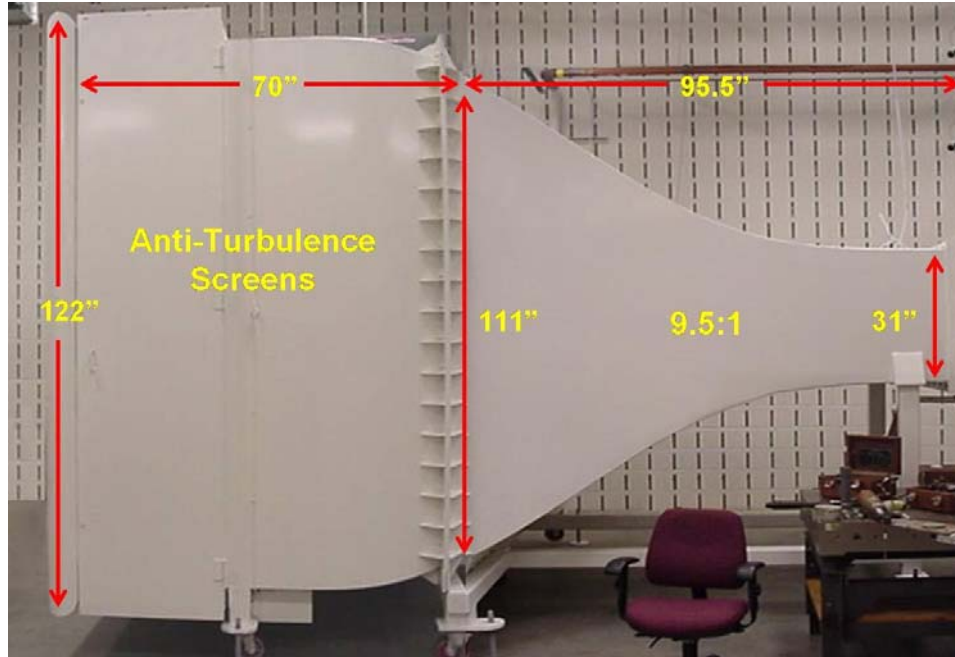


**Figure 19 Wind tunnel convergence dimensions [11].**

The test section volume is 31" h x 44" w x 72" l with an octagonal shape to reduce corner interference. The test section is shown in Figure 21. The sting mechanism in the test section is remotely controlled allowing the model to vary the angle of attack from -25 to 25 degrees.

The wind tunnel diverges after the test section and exits the tunnel through a vertical exhaust pipe. There is a protective fence to protect the fan and motor at the end of the tunnel from debris, possibly from model failure.

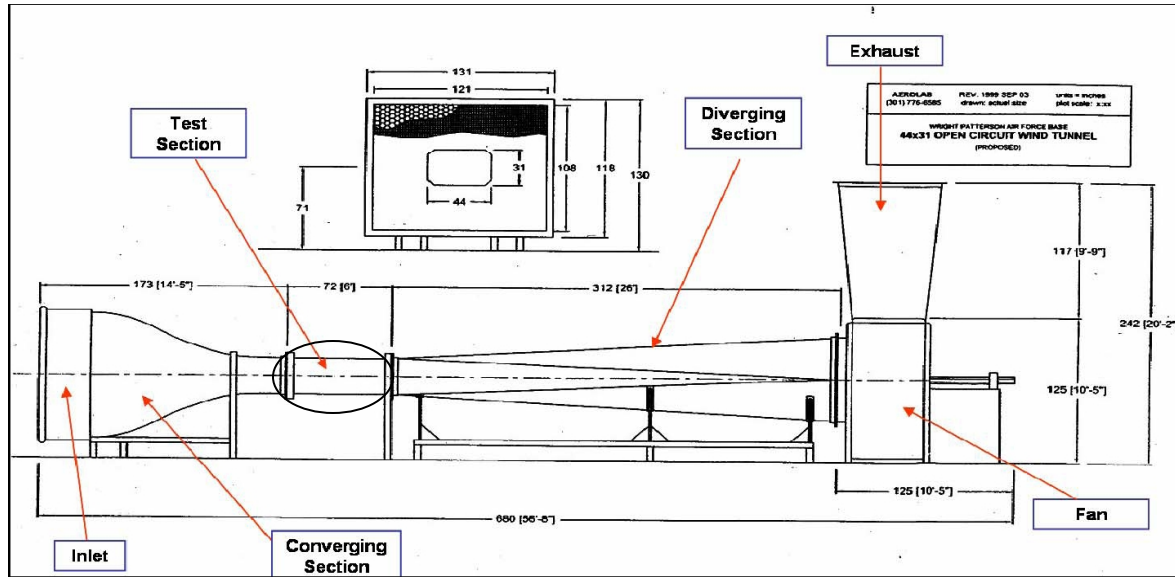


**Figure 20** AFIT 3' x 3' wind tunnel schematic [11].

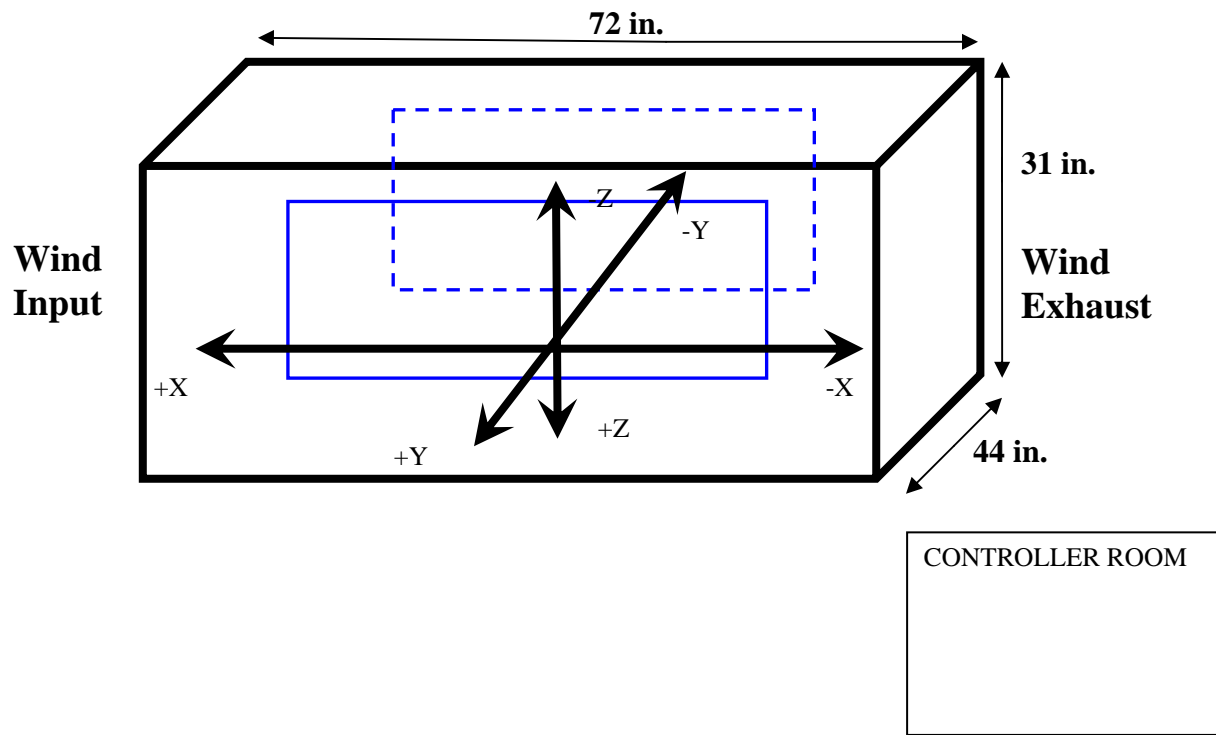


**Figure 21** Test Section of tunnel from Figure 20 with the tunnel axis as defined by the hot-wire traverse grid. [9]

## **Strain Gage Balance**

The balance utilized by this study was AFIT's eight component 25 lb balance manufactured by Able Corporation. The balance uses strain gage rosettes to measure loads in the various components. The maximum loads of this particular balance and the specific components are shown in Table 3.

**Table 3 Maximum loads of AFIT's 25 lb balance.**

Directional	Maximum
Normal Force (N1)	25 lbs
Pitch Moment (N2)	25 in-lbs
Side Force (S1)	15 lbs
Yaw Moment (S2)	15 in-lbs
Axial Force (A1)	15 lbs
Roll Moment (L1)	7 in-lbs
Axial Force (A2)	15 lbs
Roll Moment (L2)	7 in-lbs

The balance measures the forces it experiences in voltages. LabView, a software package used to write programs for calibration and data acquisition, collects the data and converts from voltages to pounds force which can be used to calculate lift, drag and moments.

This is AFIT's only eight component balance. All of AFIT's other balances have six components. The eight component balance has a second axial force component and roll moment component. The axial force component and roll moment component on the six component balances measures both the positive and negative forces. The eight component balance has one axial force component and roll component for positive forces and one for negative directions. Essentially they always have similar measurements.

## **Dantec Hot-wire Anemometer**

The Streamline 90N10 Constant Temperature Anemometer by Dantec Dynamics has a tri-axial probe that measures velocities on three coordinate axes. It mounts on a mechanical arm that extends vertically into the wind tunnel from the top. The mechanical arm is fully motorized and programmable to transverse in all three axes. A data acquisition program named Streamware, collects processes and formats the data.

## **IV. Experimental Procedures**

This section describes the procedures associated with wind tunnel data collection.

### **Balance Calibration**

The balance was calibrated by applying weights in the six degrees of freedom. The normal forces were calibrated to 25 lbs (111.2 N), side forces to 15 lbs (66.72 N), axial forces to 15 lbs (66.72 N), and roll moments to 7.5 in-lbs (0.847 N-m). The weights being applied to the balance indicated the accuracy of the balance and the interactions, or forces indicated, in the other degrees of freedom. This information was then used to correct the balance data read by applying to MatLab data reduction which will be discussed later.

### **Test Plan**

Low speed wind tunnel tests were conducted on thirteen wing configurations on the missile model. The different plastic configurations are variations of the original aluminum 30-degree swept joined wing. The different sweeps are to simulate wing morphing from compact 90 degrees against the body out to the final extension of 30 degrees. These tests are to show steady state effects of the wings in 15 degree increments. The test configurations are shown in Table 4. The wing connectors for each wing simulate moving outboard on each wing configuration as if they are moveable axis points. This is shown in Figure 17 and Figure 18.

The 60-degree swept aluminum wing and plastic wing were also compared because of their different configurations. The aluminum configuration has the wing connectors at the wingtips, where the plastic wing has the wing connectors farther inboard, closer to the missile. The wingtips are also different in that the plastic wingtip is

not parallel to the missile body. This is because it is the 30-degree wing morphed to 60 degrees. The points where the wings are attached to the missiles are also different. These connection points are closer for the plastic wings. The two wings are compared in Figure 22.

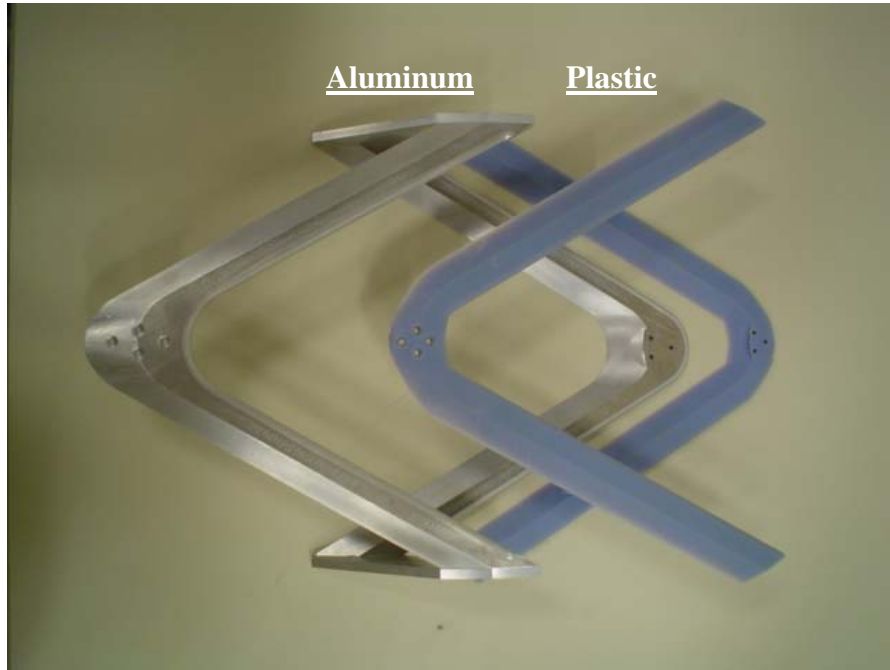


**Figure 22 Comparison between the 60° swept plastic and aluminum wings.**

Corneille [6] conducted tests at 100 mph (44.7 m/s), 130 mph (58.1 m/s), and 145 mph (64.82 m/s). For comparison purposes, tests in this investigation were run at the same speeds; however two test speeds were added, 60 mph (26.82 m/s) and 80 mph (35.76 m/s). There was an unexplained loss of lift in one of the conducted tests so the extra speeds were added to show that this was an isolated discrepancy and repeatability does exist among different speeds.

Each test was conducted at angles of attack of -4 degrees to 15 degrees. The angle of attack was increased in two degree increments up to 14 degrees then 1 degree for the final increment. This was also done to compare with Corneille [6].

**Table 4 Model Test Configurations**

Bare Model	
30° Sweep	<b><u>Aluminum</u></b>
	Single Top Swept forward
	Single Bottom Swept aft
	Joined Wing
30° Sweep	<b><u>Plastic</u></b>
	Single Top Swept forward
	Single Bottom Swept aft
	Joined Wing
45° Sweep	<b><u>Plastic (Morphed)</u></b>
	Single Top Swept forward
	Joined Wing
60° Sweep	<b><u>Aluminum</u></b>
	Joined Wing
	<b><u>Plastic (Morphed)</u></b>
	Joined Wing
75° Sweep	<b><u>Plastic (Morphed)</u></b>
	Joined Wing
90° Sweep	<b><u>Plastic (Morphed)</u></b>
	Joined Wing

## Computation of Parameters

The forces measured by the balance are body axis forces. This axis changes with the orientation of the missile's body. These forces must be converted to the wind axis, or the tunnel axis, to calculate the lift and drag forces and the pitching and rolling moments.

The lift, drag, pitching moment and rolling moment coefficients were determined for each configuration.

### *Lift*

Lift is the component of force normal to the wind axis shown in Figure 23. The balance reads the normal force and axial force of the missile which must be converted to the wind axis to get lift,  $L$ , using Equation (1), where  $N$  is the total normal force,  $A$  is the total axial force, and  $\alpha$  is the angle of attack.

$$L = N \cos \alpha - A \sin \alpha \quad (1)$$

Once the lifting force is determined it must be non-dimensionalized, because this is a scale model. To non-dimensionalize a force, the wing area and dynamic pressure are divided out of the force. The lift coefficient is the non-dimensional term desired. Equation (2) calculates the lift coefficient,  $C_L$ . Reference areas are given in Table 1.

$$C_L = \frac{L}{\frac{1}{2} \rho_\infty V_\infty^2 S} \quad (2)$$

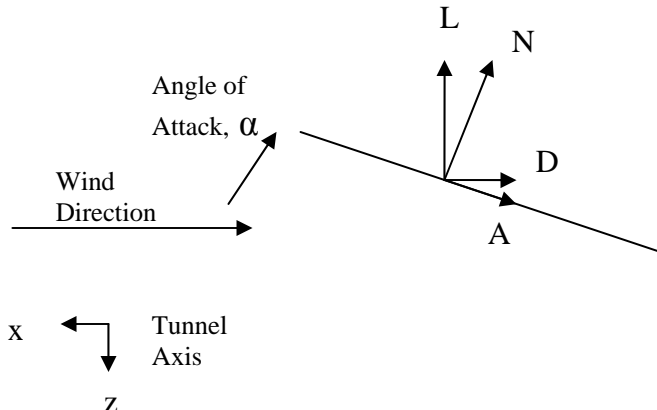


**Figure 23 Wind axis and body axis forces.**

### *Drag*

Drag is the force parallel to the wind axis shown in Figure 23. Again the forces measured by the balance need to be converted from the body axis to the wind axis. Equation (3) calculates drag, where  $N$  is the total normal force,  $A$  is the total axial force and  $\alpha$  is the angle of attack.

$$D = N \sin \alpha + A \cos \alpha \quad (3)$$

Once the drag is calculated from measured values it also was non-dimensionalized using Equation (4).

$$C_D = \frac{D}{\frac{1}{2} \rho_\infty V_\infty^2 S} \quad (4)$$

This drag coefficient is the sum of profile drag and induced drag. The profile drag is usually obtained from experimental data. Induced drag is a by-product of lift. Equation (5) gives the induced drag coefficient, where AR is the aspect ratio, and  $e$  is the efficiency factor. The efficiency factor can be solved for using Figure 8.

$$C_{D,I} = \frac{C_L}{\pi e AR} \quad (5)$$

Normally, the aspect ratio is defined by Equation (6), where  $b$  is span and  $S$  is reference area, and this is still true for the single wing configurations. For the joined wing configurations aspect ratio is redefined by Equation (7), where  $AR_T$  is the total aspect ratio,  $AR_F$  is the front wing aspect ratio,  $S_F$  is the front wing surface area,  $AR_R$  is the rear wing aspect ratio, and  $S_R$  is the rear wing surface area [2]. Equation (7) was used to calculate the aspect ratio in Table 1.

$$AR = \frac{b^2}{S} \quad (6)$$

$$AR_T = \frac{AR_F \left( \frac{S_F}{S_R} \right) + AR_R \left( \frac{S_R}{S_F} \right)}{\left( \frac{S_F}{S_R} + 1 \right) \left( \frac{S_R}{S_F} + 1 \right)} \quad (7)$$

### ***Pitching Moment***

Moments show the stability of an aircraft. The pitching moment is calculated about the center of gravity of the model by doing a sum of moments. Figure 24 shows the lifting forces seen by the missile. The balance reads the total lifting forces at the point of the balance, or  $N$ . The pitching moment found by calculating the distance from the center of gravity to where the balance measures the normal forces as seen in Equation (8), where  $a$  is the distance from center of gravity of the model to the balance strain gage.

$$M = N a \quad (8)$$

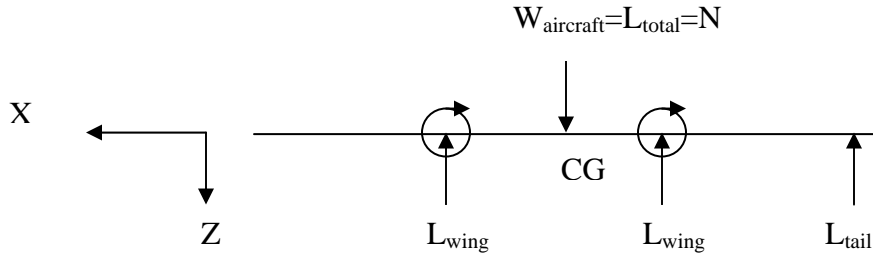


**Figure 24 Diagram of lifting forces on the missile.**

Then the moment coefficient is determined by applying Equation (9), where  $c$  is the chord length.

$$C_M = \frac{M}{\frac{1}{2} \rho_\infty V_\infty^2 Sc} \quad (9)$$

### ***Rolling Moment***

The rolling moment shows the tendency for the missile to roll in flight conditions which would cause control problems. The balance is already on the missile's rolling axis and has a component to measure the rolling moment,  $L'$ . Equation 10 calculates the rolling moment coefficient.

$$C_{L'} = \frac{L'}{\frac{1}{2} \rho_\infty V_\infty^2 Sc} \quad (10)$$

### ***Compressibility Analysis***

The maximum speed of the wind tunnel is 145 mph (64.82 m/s), which is well within the incompressibility regime. This missile is more likely to fly in the compressibility regime at about Mach 0.7. The Prandtl and Glauert compressibility

correction Equations (11-12) can give a better idea of the coefficients in the compressibility region.

$$C_L = \frac{C_{L,o}}{\sqrt{1 - M_\infty^2}} \quad (11)$$

$$C_D = \frac{C_{D,o}}{\sqrt{1 - M_\infty^2}} \quad (12)$$

These equations are pretty good approximations and can be used up to Mach 0.8 where they can no longer be used due to the anomalies of transonic flow. By simple analysis of these equations, it should be realized that as Mach increases so will the lift and drag coefficients.

### ***Tare***

When the missile is connected to the balance and there is no flow through the wind tunnel, the balance still has small readings and needs to be zeroed out like a weight scale. To do this, the missile is put through a run in the wind tunnel with no wind for each test configuration. The data measured by the balance for those runs are put into what are called tare files. Then the model is put through tests at the specified wind speeds, data are recorded and put into test files. These files are inputted into the MatLab, shown in Appendix B, which subtracts out the tare data from the test data to give you the actual force readings of the balance to reduce error.

### ***Blockage Correction***

The wind speed at the beginning of the test section, where the pressure transducer measures the velocity, is different than the point in the tunnel where the model is placed

and tested. This is due to friction of the walls of the wind tunnel. This causes the pressure transducer, which is upstream, to be greater than the point where the model will be in the test section. The velocity at the model test section is the velocity used for the aforementioned calculations. Because the transducer is measuring the upstream velocity, a correction was made to get the velocity at the test section.

The hot-wire anemometer was used to measure the velocity at the point in the test section where the modes is to be placed. This is an open tunnel measurement. Figure 25 shows how the anemometer was positioned in the tunnel. The hotwire recorded the velocities at the test location with open tunnel configuration at speeds of 60, 80, 100, 130, and 145 mph.

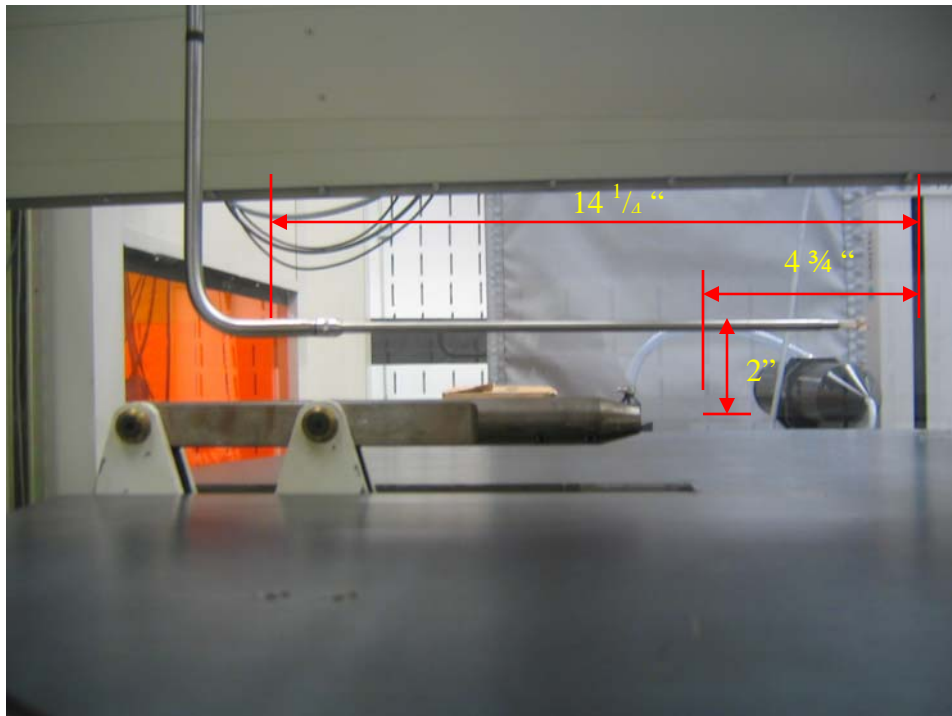


**Figure 25 Shows placement of hotwire anemometer [16].**

The hotwire started measuring the velocity 0.5 mm in the positive Y direction and was programmed to move in 0.1 mm increments in the pattern shown in Figure 26. The hotwire measured a  $1.0 \text{ mm}^2$  plane.

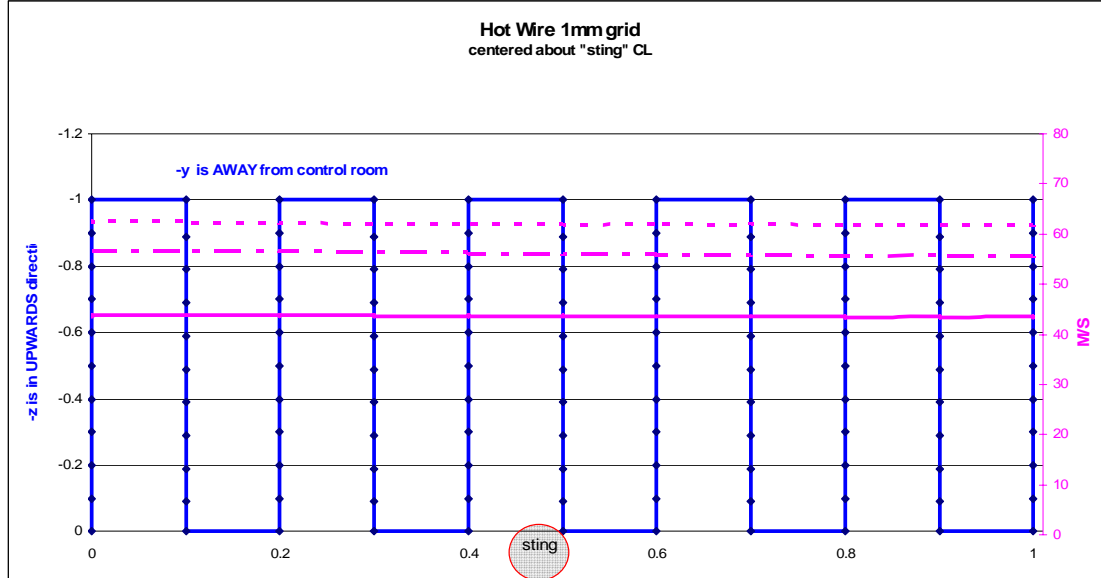


**Figure 26 Hotwire test pattern [9].**

The Dantec Streamware software saves the recorded measurements as voltages. These measurements are then converted to mph to compare them to the transducer measurements which are in mph. Equation (13) compares the two velocities, where  $\varepsilon_{tc}$  is the total blockage,  $U_{OT}$  is the freestream velocity at the model or hotwire, and  $U_{Tr}$  is the freestream velocity at the beginning of the wind tunnel or transducer.

$$\varepsilon_{tc} = \frac{U_{OT}}{U_{Tr}} \quad (13)$$

## V. Results & Analysis

Using the procedures established in the last chapter, the data were recorded and analyzed.

### Wind Tunnel Blockage Correction

Equation (13) was used to calculate the velocity blockage correction factor between the hotwire and transducer velocity measurements. Table 5 summarizes the correction factors for each speed. Figure 27 shows the velocity comparison. These velocity corrections were then applied to the MatLab code in Appendix B to convert the recorded velocity of the transducer to the actual velocity the model is experiencing. As can be seen, the difference between the two ranged from a 4% to 10% difference, which is normal.

**Table 5 Difference in velocity between the transducer and hotwire.**

	60 mph	80 mph	100 mph	130 mph	145 mph
$\epsilon_{tc}$	0.9111794	0.9002786	0.955283	0.960305	0.954742

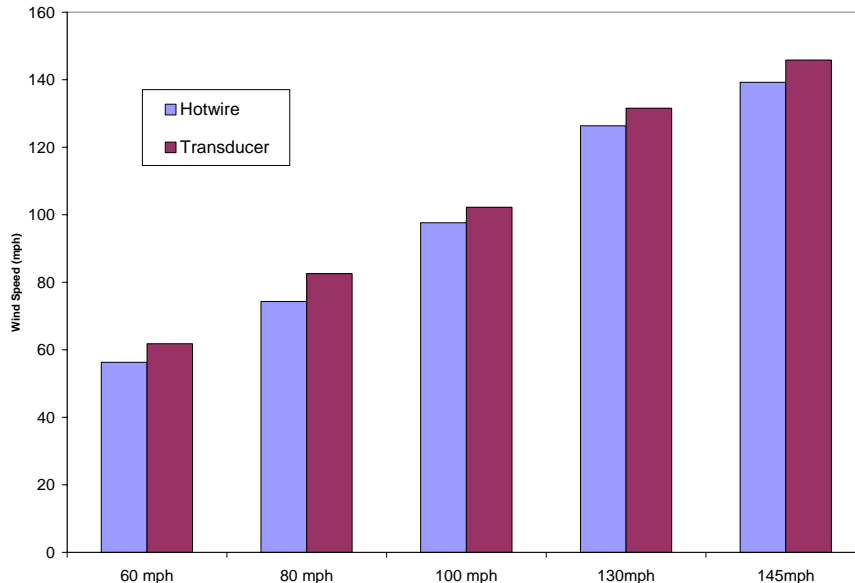


**Figure 27 Hotwire vs. transducer velocity measurements.**

## **Wing Configuration Comparison**

All the recorded data were run through the MatLab code in Appendix B, and the lift, drag, pitch and roll coefficients were calculated. Lift, drag, pitch, and roll curves were then created to compare the data retrieved.

The first test was conducted to recreate the results from Corneille [6] for the 30-degree and 60-degree negative stagger, because the tests for this study were conducted in a different wind tunnel and on a different balance. Figure 28 shows the lift comparison for the 30-degree swept aluminum joined wings in the new wind tunnel on the 25 lb balance versus Corneille's [6] test. To make comparisons, the graph for this study was transposed on top of Corneille's [6]. At speeds of 100 mph, 130 mph, and 145 mph the lift and drag curves are a match to Corneille's [6] lift coefficient. The same was found for the 60-degree swept aluminum wings shown in Figure 29, which matches Corneille's [6] curve on page 70 of her thesis. This shows that Corneille's [6] data is consistent and reproducible, which gives significance to the follow on investigations. Corneille [6] didn't test at 60 mph or 80 mph and only tested up to an angle of attack of 13 degrees, so that data cannot be compared.

It is interesting to note that for all the tests conducted of the 30-degree swept aluminum joined wing, there are two positions of temporary wing stall. There is one at about 4 degrees angle of attack and one at about 12 degrees angle of attack. It can also be noted that for the tests at 60 mph and 80 mph these stall characteristics are seen at lower angles of attack and more amplified. A similar characteristic is also seen in Hoang and Soban [10]. It was attributed to a low Reynolds number of  $0.4 \times 10^6$  and a thin airfoil selection of 12% of the chord. In this study, the Reynolds number ranged from  $0.4 \times 10^6$

to  $1.5 \times 10^6$  and the airfoil thickness was 18.25% of the chord. These conditions could be a possible cause of the wing stall in this study. The wing configuration in Hoang and Soban [10] was a single wing with 20-degree sweep. Looking at the single wing configurations with 30-degree sweep from this study in Appendix A, the temporary wing stall is also seen. It is not solely a condition of just the joined wings in this study. It seems to be more of a condition of the sweep, specifically the 30-degree sweep in this study. Wolkovitch [22] also suggests that joined wings have a premature flow detachment causing wing stall, which could also be a contributor to this study's wing stall.

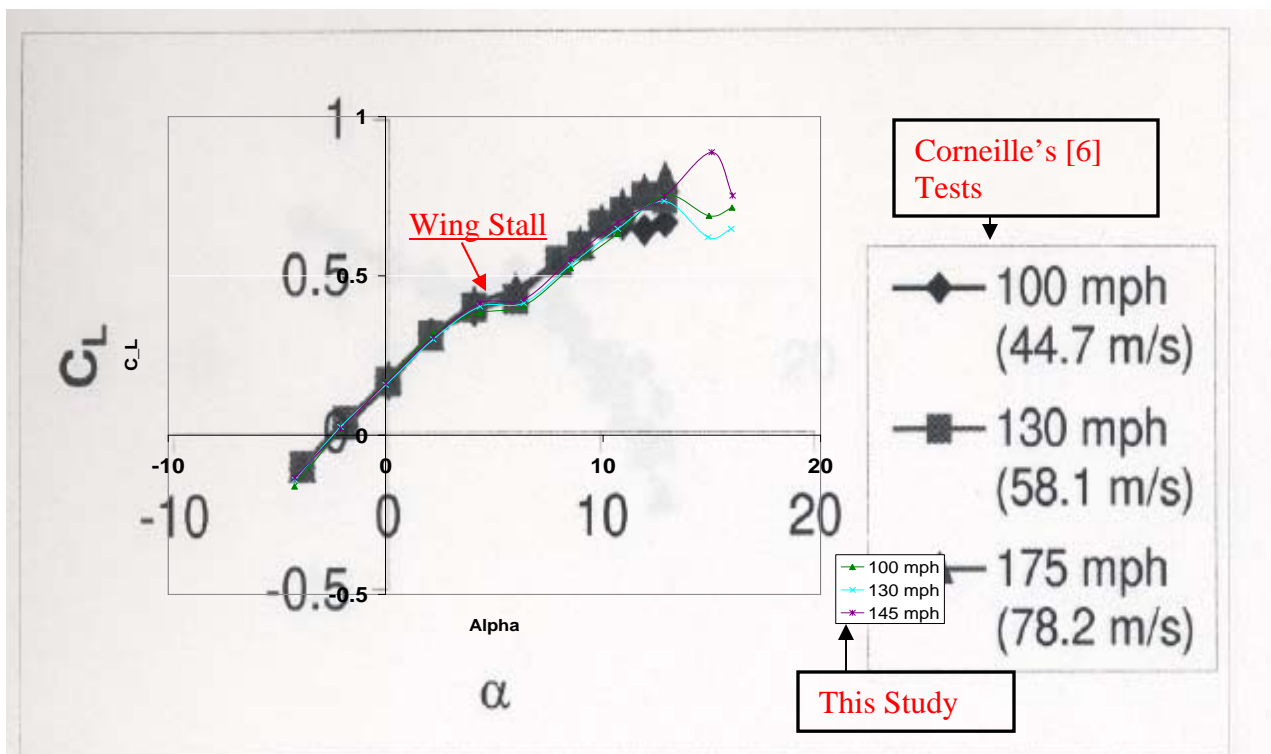


**Figure 28 Comparison between Corneille [6] and this study's results for the 30° joined wing made of aluminum.**

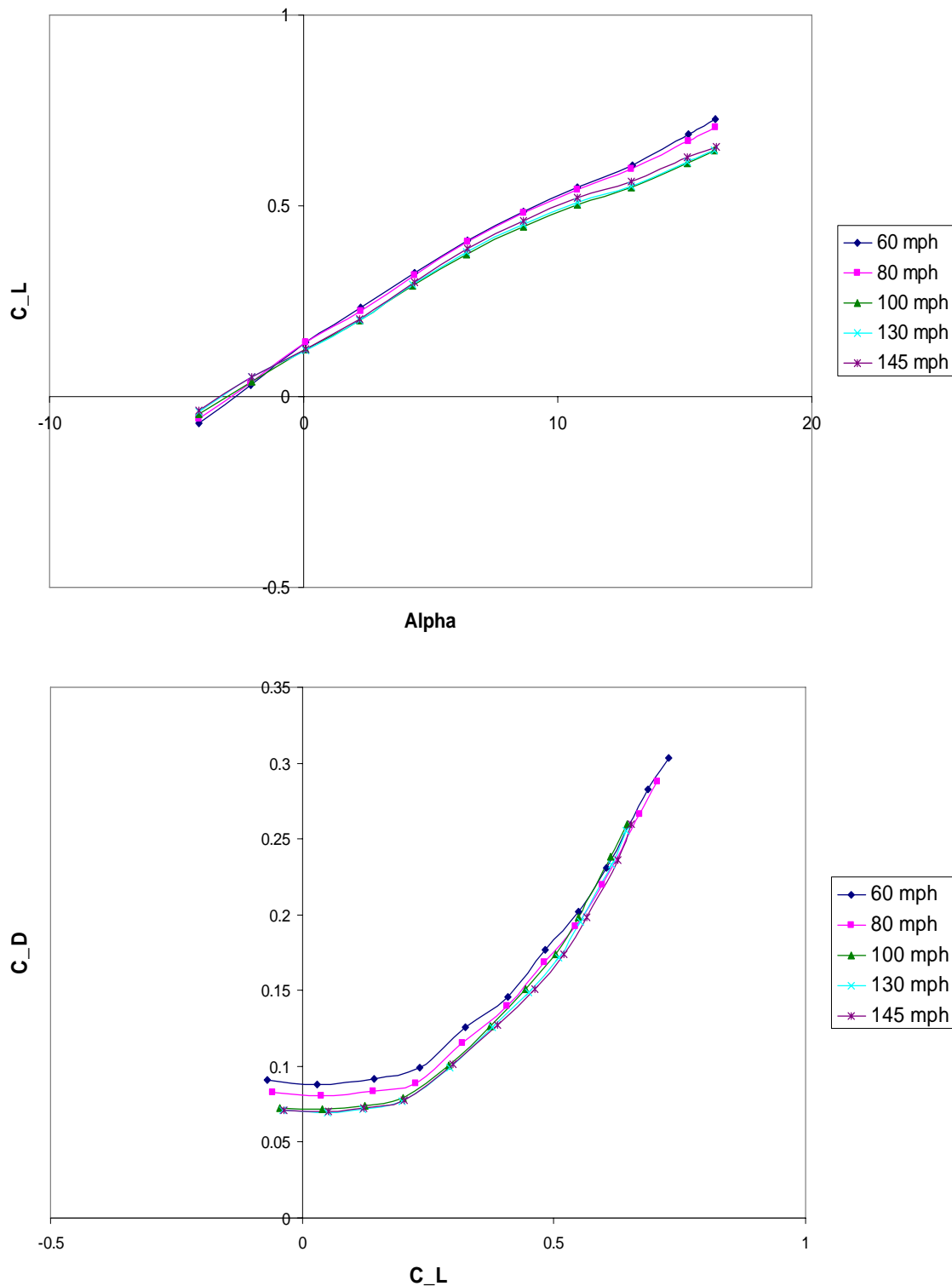


**Figure 29 Lift and drag relations of the 60° joined wing, not morphed, aluminum.**

The next comparison is the plastic versus the aluminum 30-degree swept joined wing, because it is the main wing of which the morphed wings are derived. The comparisons at 60, 80, 100, 130, and 145 mph are shown in Figure 30 through Figure 34. These curve comparisons show that the plastic wings with 30-degree sweep also have the two losses of lift that the aluminum wings experienced, which was mentioned earlier. The major difference is that the plastic wing's second loss of lift was seen at a lower angle of attack. This could possibly be due to the difference in stiffness and surface roughness. The plastic wings are less stiff and rougher than the aluminum configurations.

The 130 mph comparison must be noted because it has the biggest discrepancy at 10 degrees to 13 degrees angle of attack. It was decided to run the tests at 60 mph and 80 mph to see if this discrepancy happened at any other speeds, or if it was a phenomenon of the 130 mph speed at this specific angle of attack for this particular configuration of wings. Loss of lift of this magnitude was not seen at any other speeds. The test was then conducted again with a strobe light to see if the loss of lift is caused by the wing hitting its resonance frequency. At about 9 degrees angle of attack the wings began to visually vibrate rapidly until the angle of attack of 13 degrees was reached. The loss of lift can be attributed to the 30-degree swept plastic joined wings hitting a resonance frequency causing rapid vibration. Bagwill and Selberg [21] state that the structural complexity of joined wings increases the number of natural frequencies that produce modes of vibration. This is the probable cause. The material difference between the plastic and the aluminum will also add to this effect.

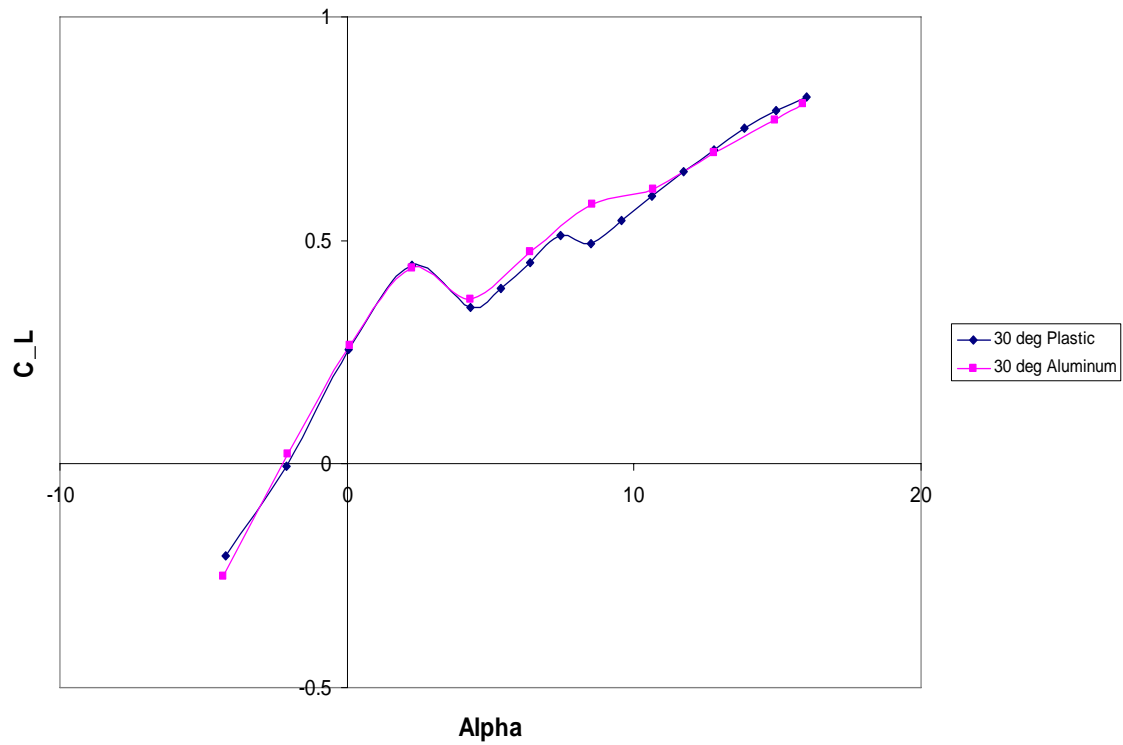


**Figure 30 Comparison of 30° joined wing, plastic and aluminum at 60 mph.**

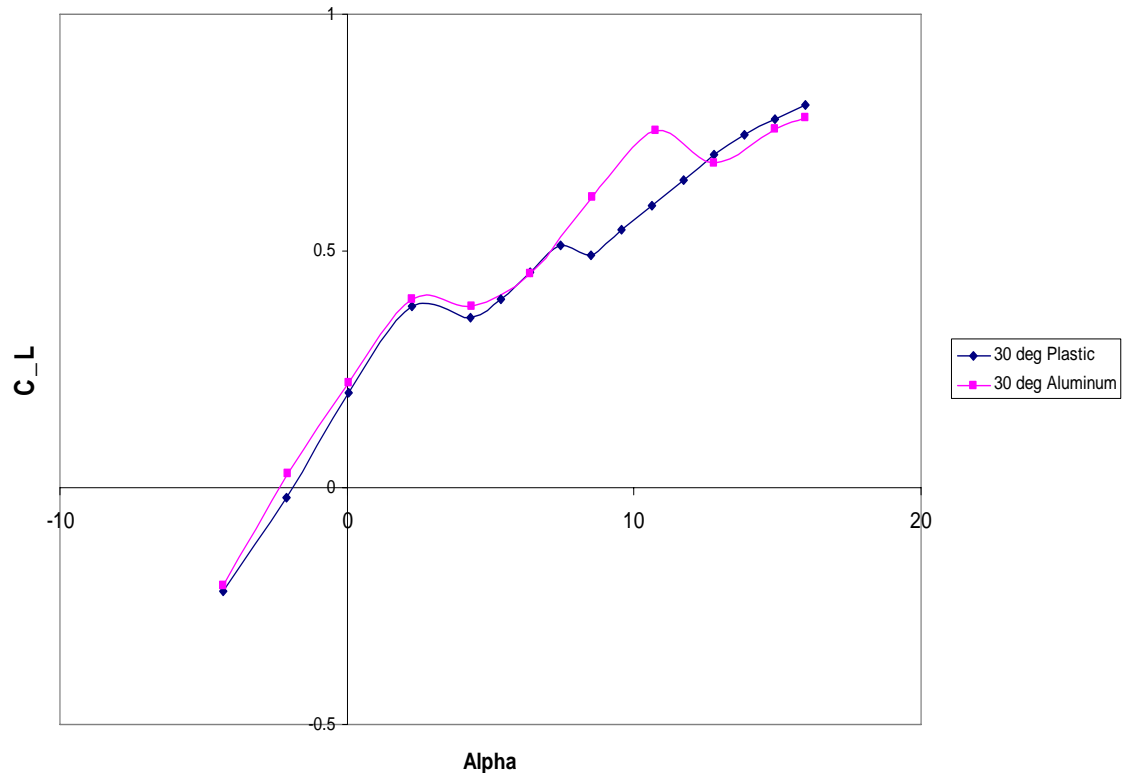


**Figure 31 Comparison of 30° joined wing, plastic and aluminum at 80 mph.**

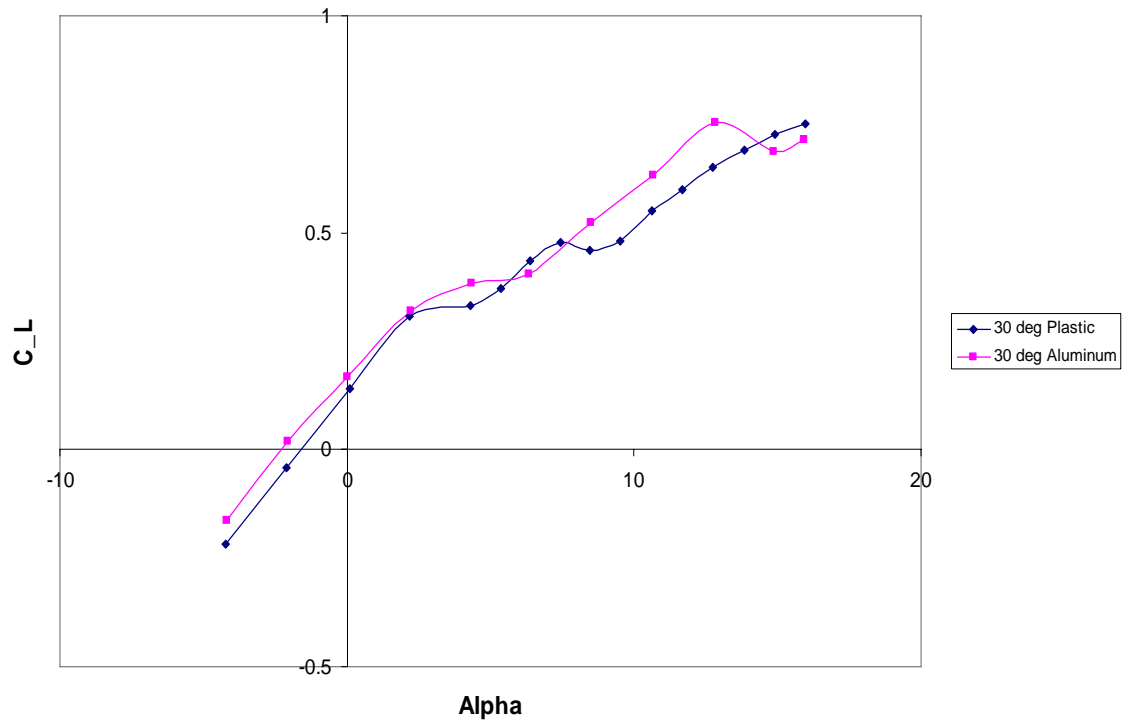


**Figure 32 Comparison of 30° joined wing, plastic and aluminum at 100 mph.**

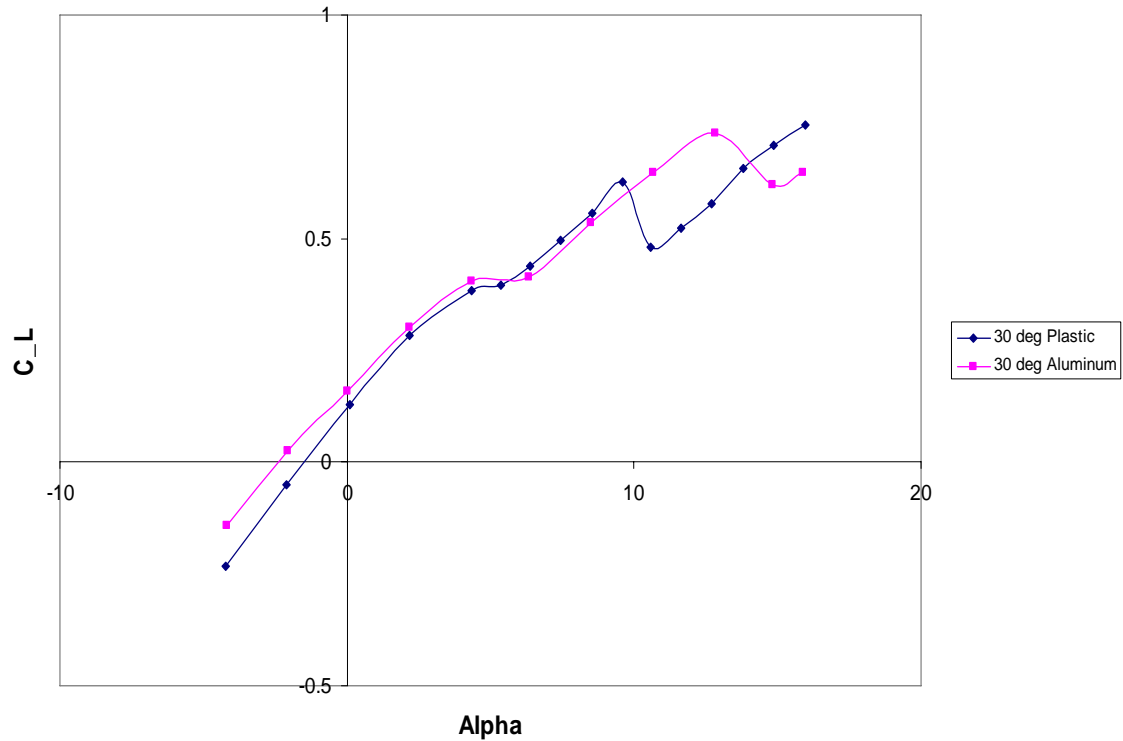


**Figure 33 Comparison of 30° joined wing, plastic and aluminum at 130 mph.**

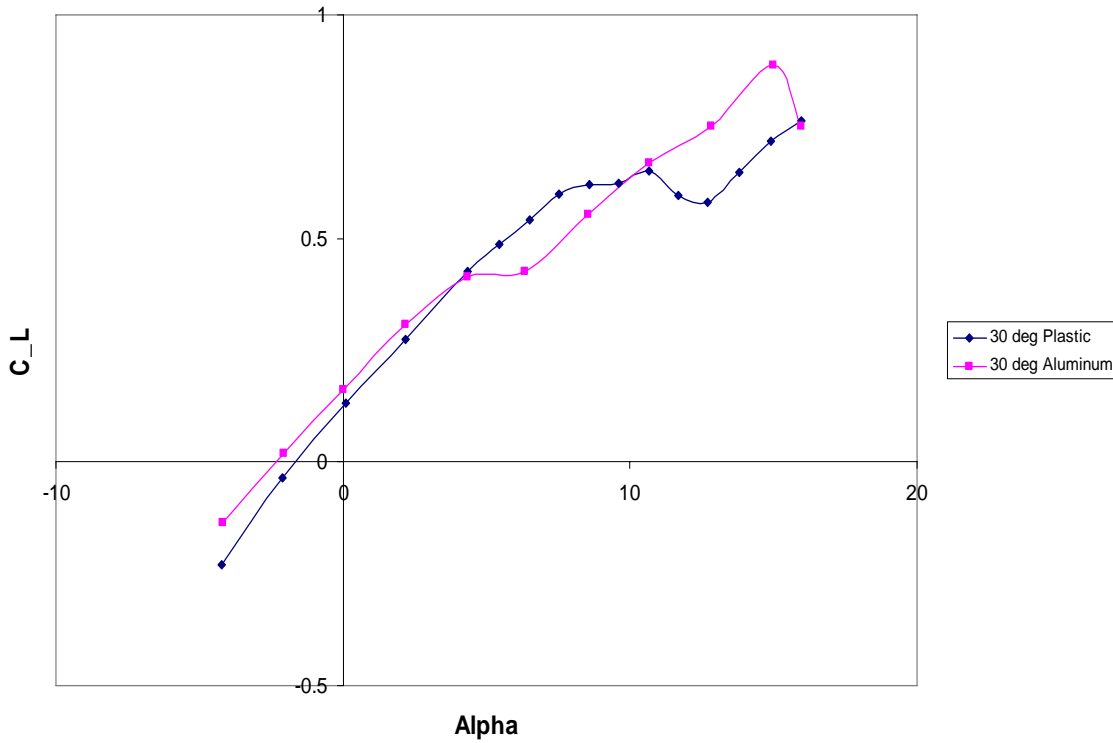


**Figure 34 Comparison of 30° joined wing, plastic and aluminum at 145 mph.**

Comparisons were also made between the various degrees of the 30-degree swept joined wings being morphed/swept back. The results matched expectations given by Bertin [4], who states that increasing sweep decreases the lift. As the wings are morphed outward from the missile's body, the lift coefficient increases until the 45 degree sweep is reached. Once the wings were morphed to their full extension of 30 degrees, the wings experienced temporary wing stall at about 2 degrees angle of attack, which brought the lift coefficient below that of the 45 degree swept wings. This can be seen in Figure 35 through Figure 39. Taking a closer look at these figures, temporary wing stall on the 30-degree configuration can also be seen on the 45 degree configuration, although it is less noticeable. This indicates that as the wings open from the 45 degree sweep to the 30-degree sweep, more wing stall is experienced. This is probably due to the Reynolds

number decreasing and becoming too low. The Reynolds number decreases because it is a function of chord length and as the wings are morphing to their full extension, the chord length is decreasing. The chord length is the distance from the leading edge of the wing to the trailing edge and is parallel to the missile's body. So, as the wing morphs out the sweep angle and the chord length both decrease.

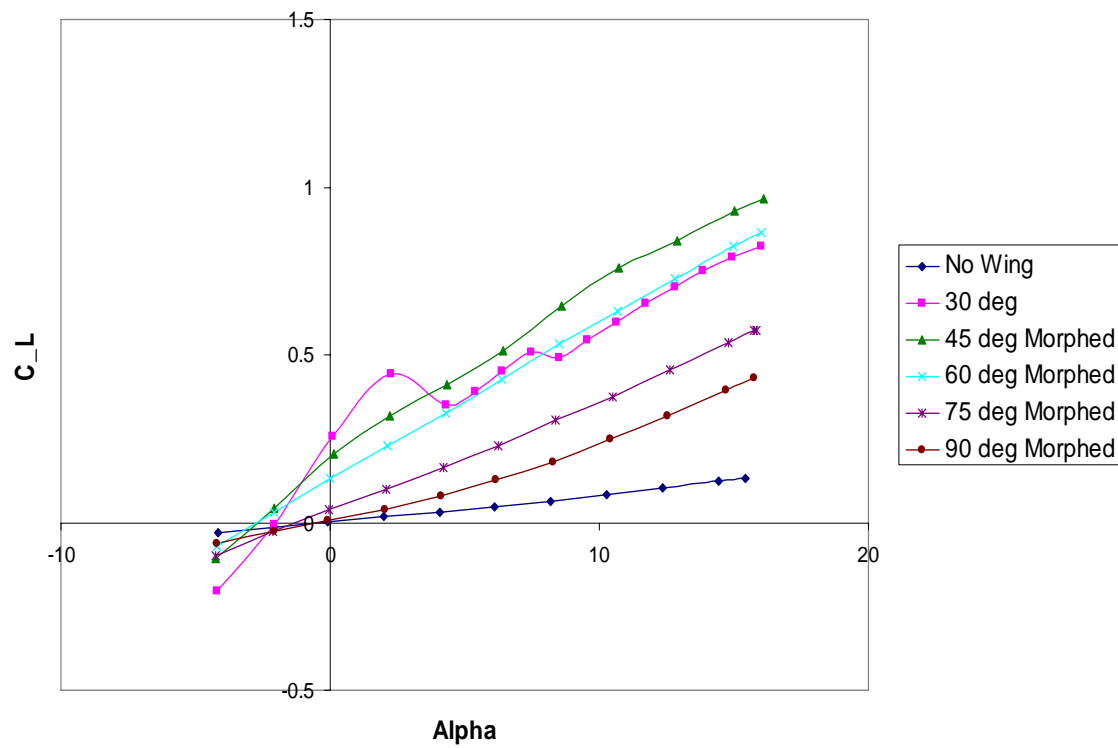


**Figure 35 Lift comparison of the morphing wing set at 60 mph.**

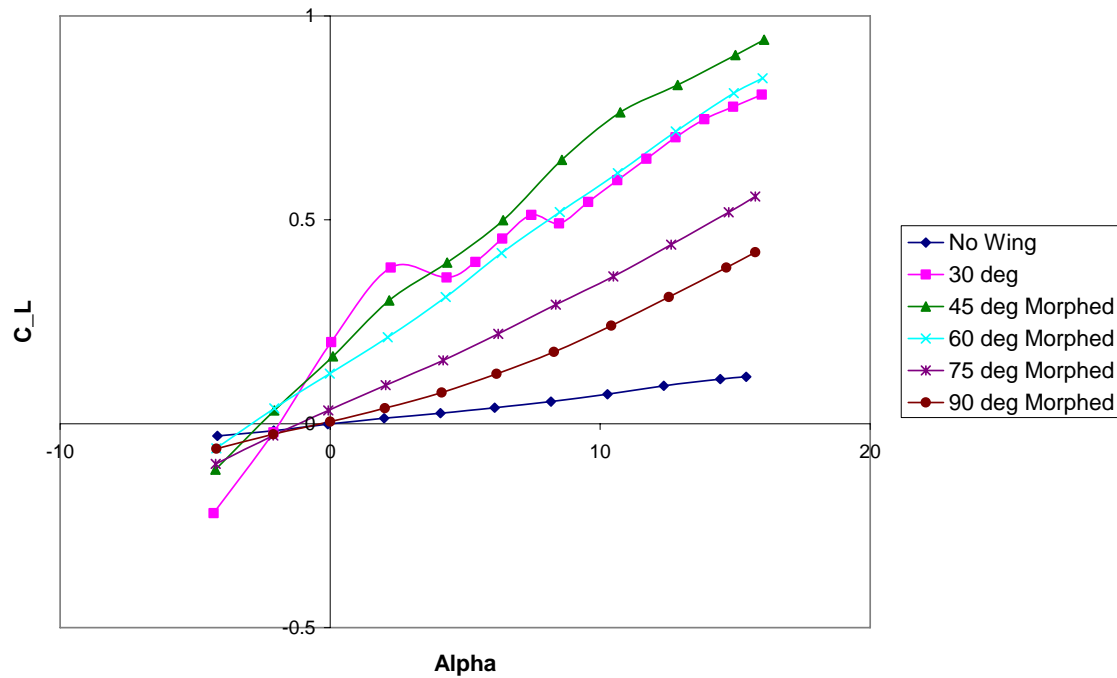


**Figure 36 Lift comparison of the morphing wing set at 80 mph.**

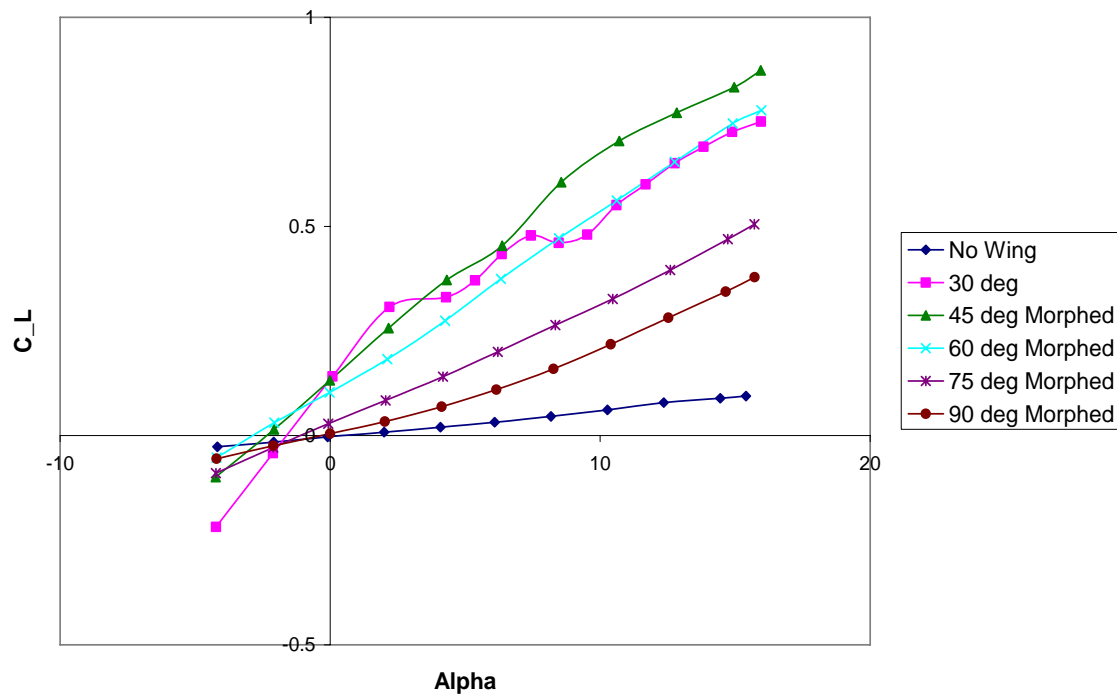


**Figure 37 Lift comparison of the morphing wing set at 100 mph.**

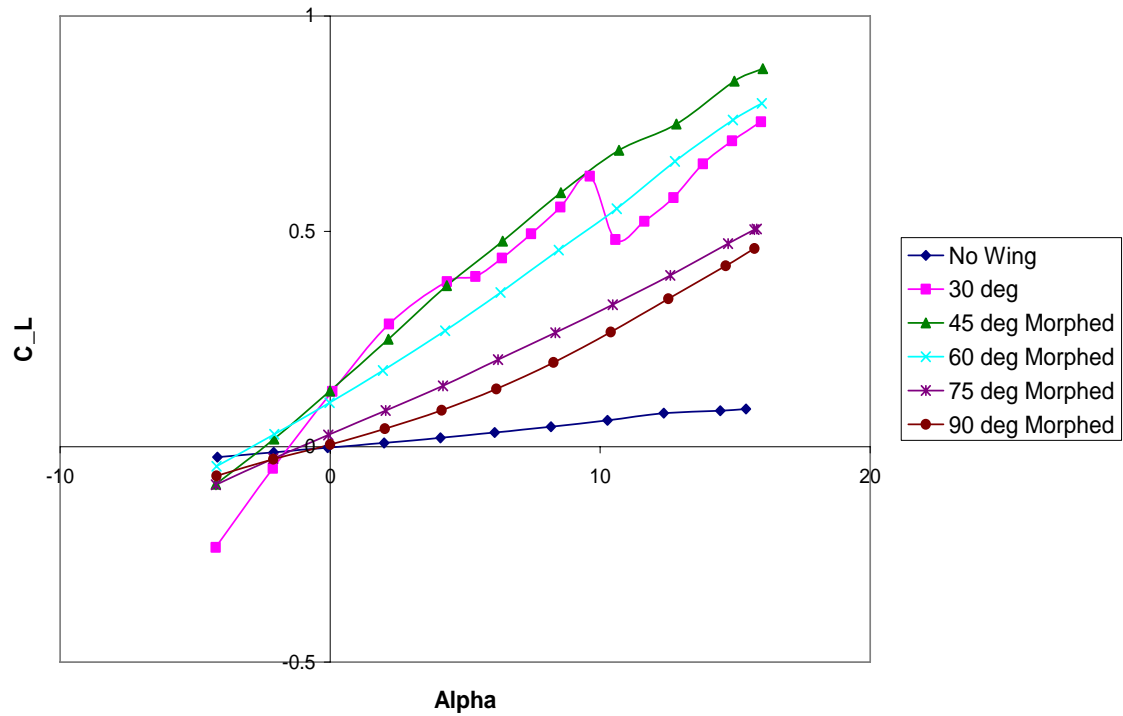


**Figure 38 Lift comparison of the morphing wing set at 130 mph.**

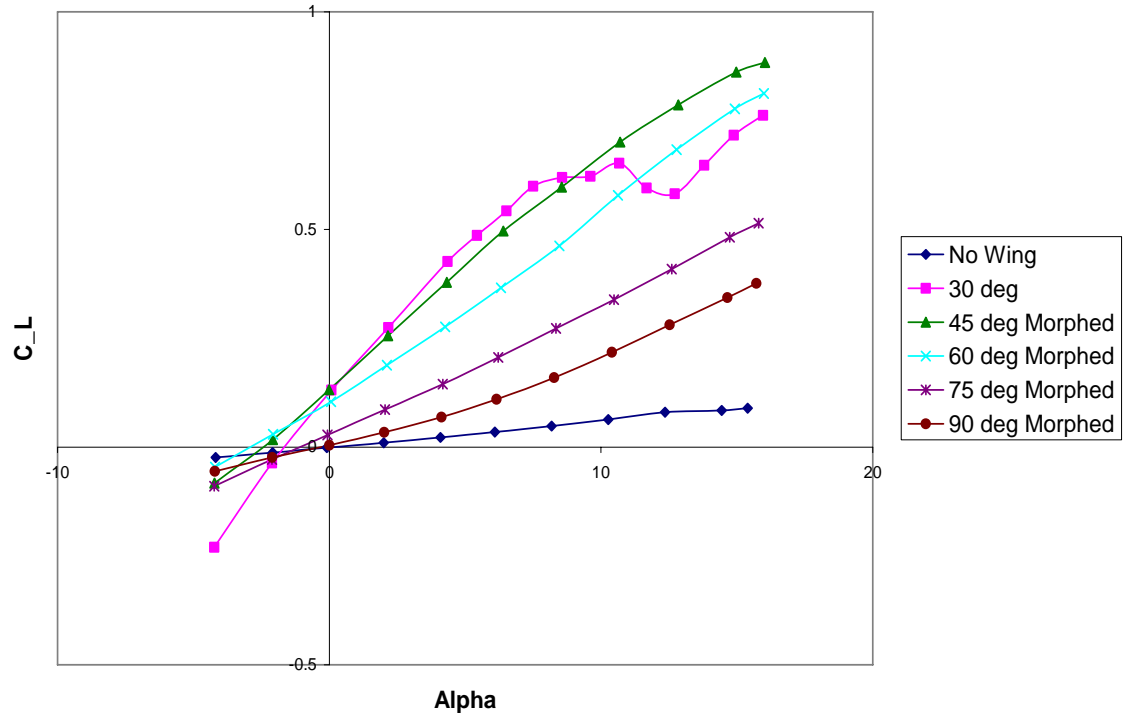


**Figure 39 Lift comparison of the morphing wing set at 145 mph.**

Figure 40 through Figure 44, show that there are drag increases among the wing configurations as the wings open outward from the body to the fully extended position. The drag rise is expected because of the increasing frontal area as the wings morph out to the 30-degree sweep. This is consistent with Bertin [4], who states that increasing sweep decreases the drag. There is also consistency with the Wolkovitch [22, 23], because both the 30-degree single wing configurations produce more drag than the 30-degree joined wing configuration.

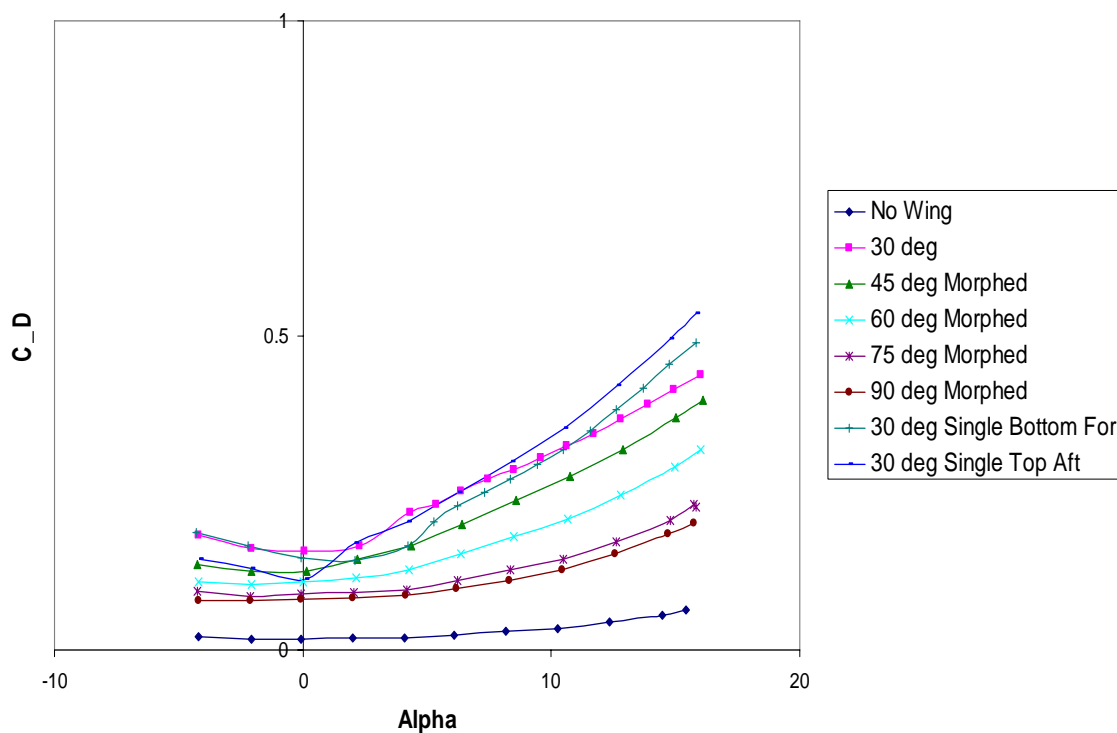


**Figure 40 Drag comparison of the morphing wing set at 60 mph.**

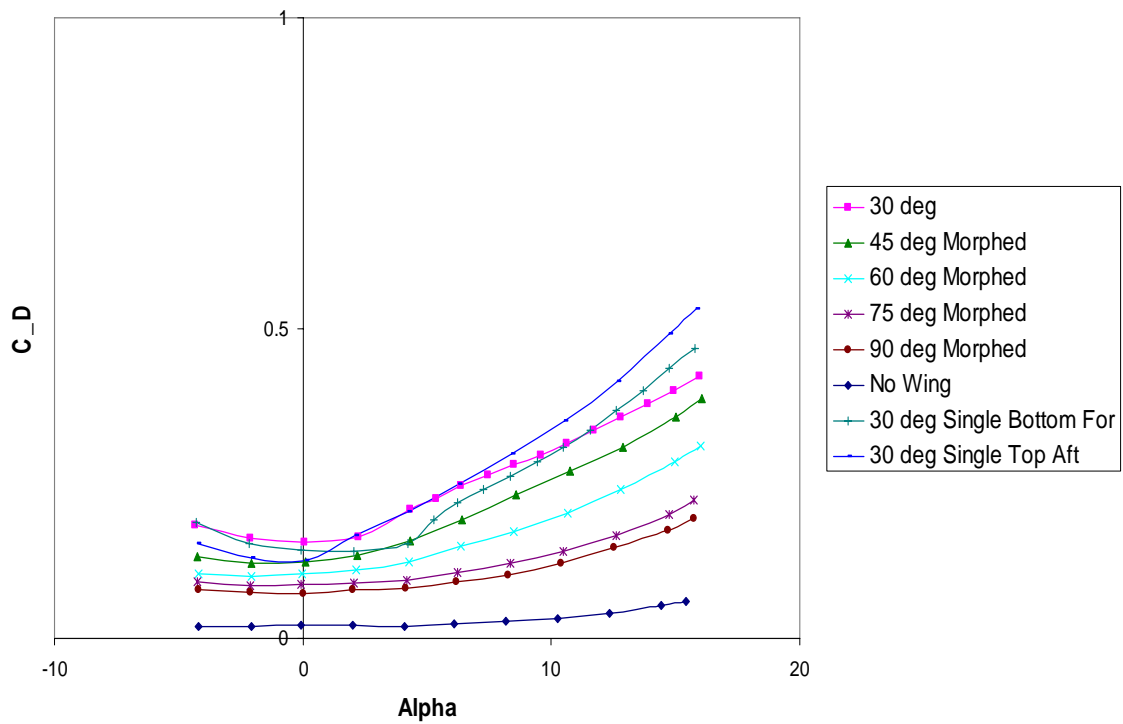


**Figure 41 Drag comparison of the morphing wing set at 80 mph.**

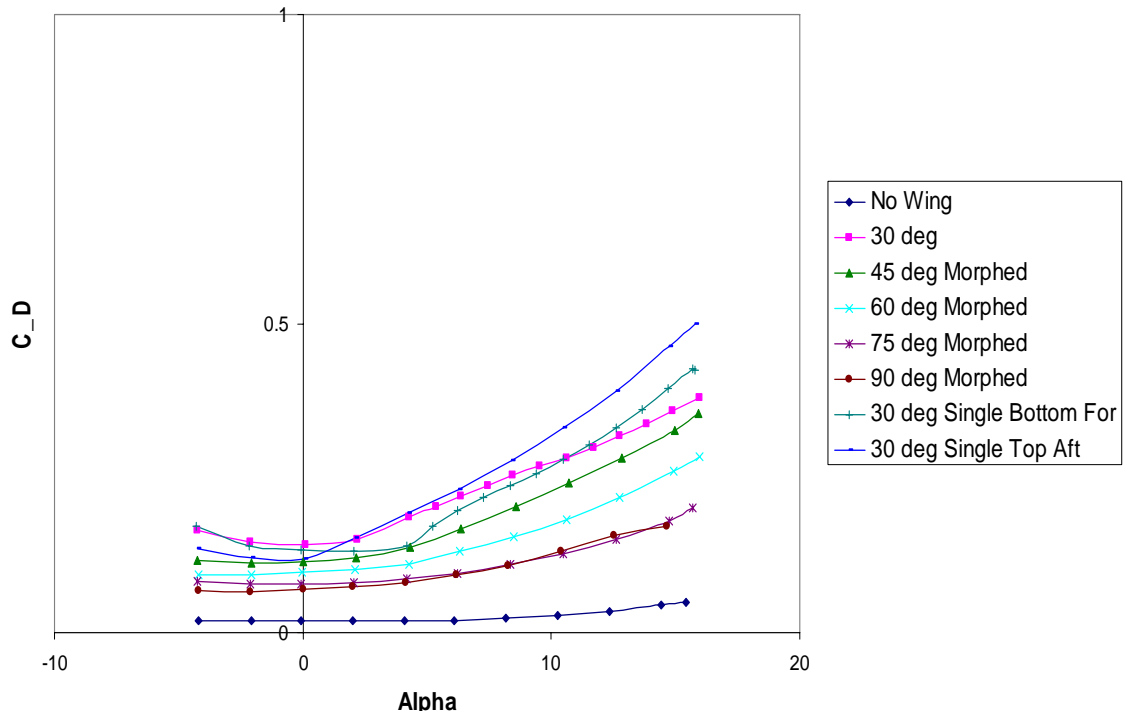


**Figure 42 Drag comparison of the morphing wing set at 100 mph.**

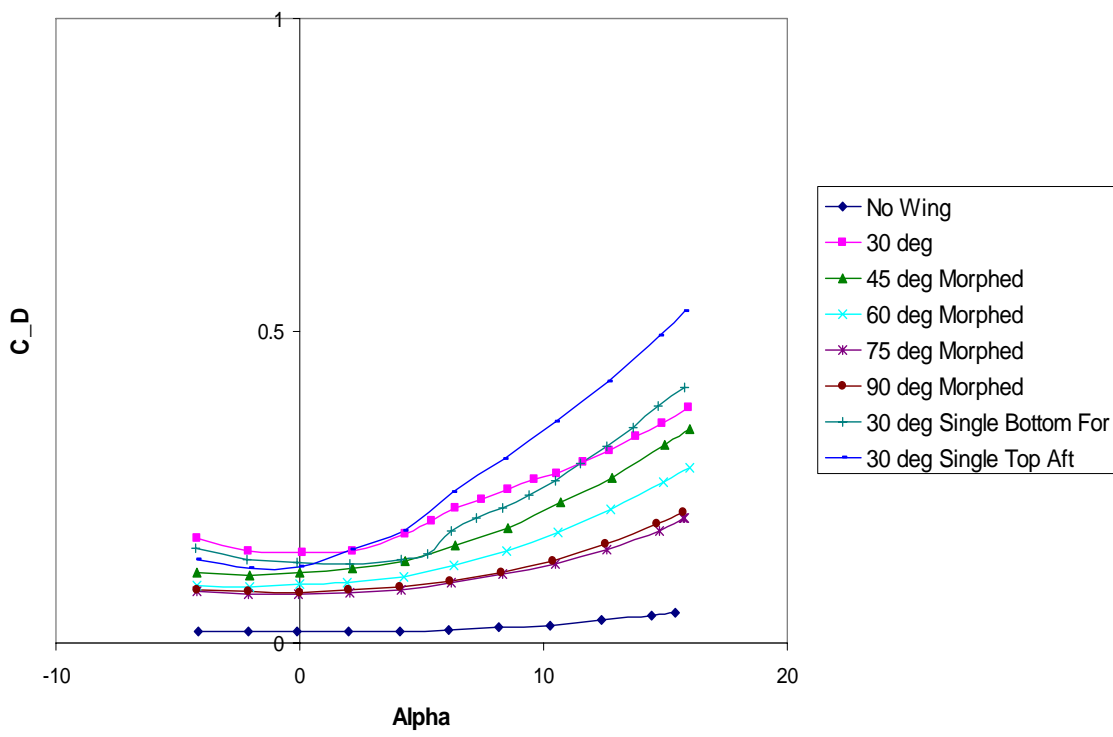


**Figure 43 Drag comparison of the morphing wing set at 130 mph.**

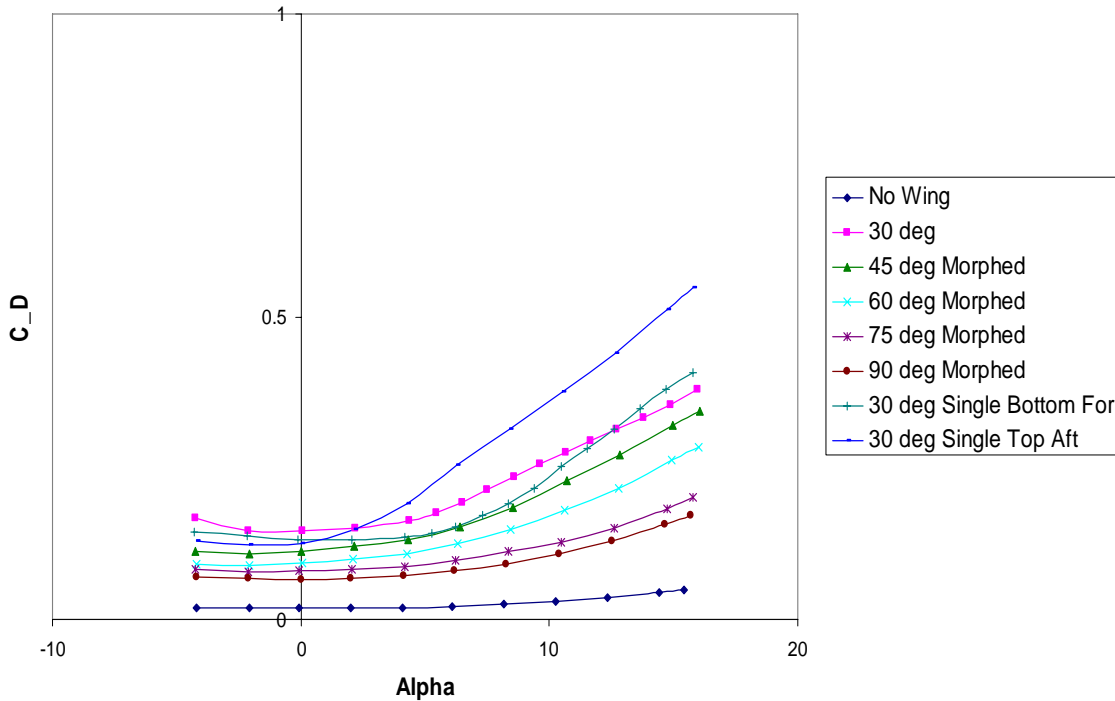


**Figure 44 Drag comparison of the morphing wing set at 145 mph.**

A comparison was made between the morphed 60-degree wing from this study and the 60-degree aluminum wing from Corneille's [6] study to see if there are any major aerodynamic differences. Figure 22 shows the structural differences between the two 60-degree swept configurations. The major differences are the placement of the wing connectors, the distance between the wing roots are closer together on the plastic model than the aluminum configuration, and the wingtips are of different shape. The aluminum wing's connectors act as winglets at the wingtips. The plastic configuration has the wing connectors inboard of the wingtips. Also, the aluminum wing's wingtips are parallel to the missile's body, where the plastic wing's wingtips are not because they are in a morphed position from the original 30-degree swept wing. They are parallel when in the 30-degree swept position. A comparison of the aerodynamic properties was done to see the effects of these differences. The 60 mph comparison is made in Figure 45 which shows the plastic configuration experiences slightly more lift than the aluminum configuration. This same result is seen at each of the other test speeds, which can be seen in Figures 81 to 84 (Appendix A). Winglets have shown to increase the lift-curve slope and maximum lift coefficient, while decreasing the induced drag [2, 7]. Also tip shape not parallel to wind flow has shown to decrease lift slope [7]. The results of this test were inconsistent with all of the literature researched. The wings are too dissimilar, that no conclusions can be drawn as to what causes the change in lift slope and max lift coefficient.

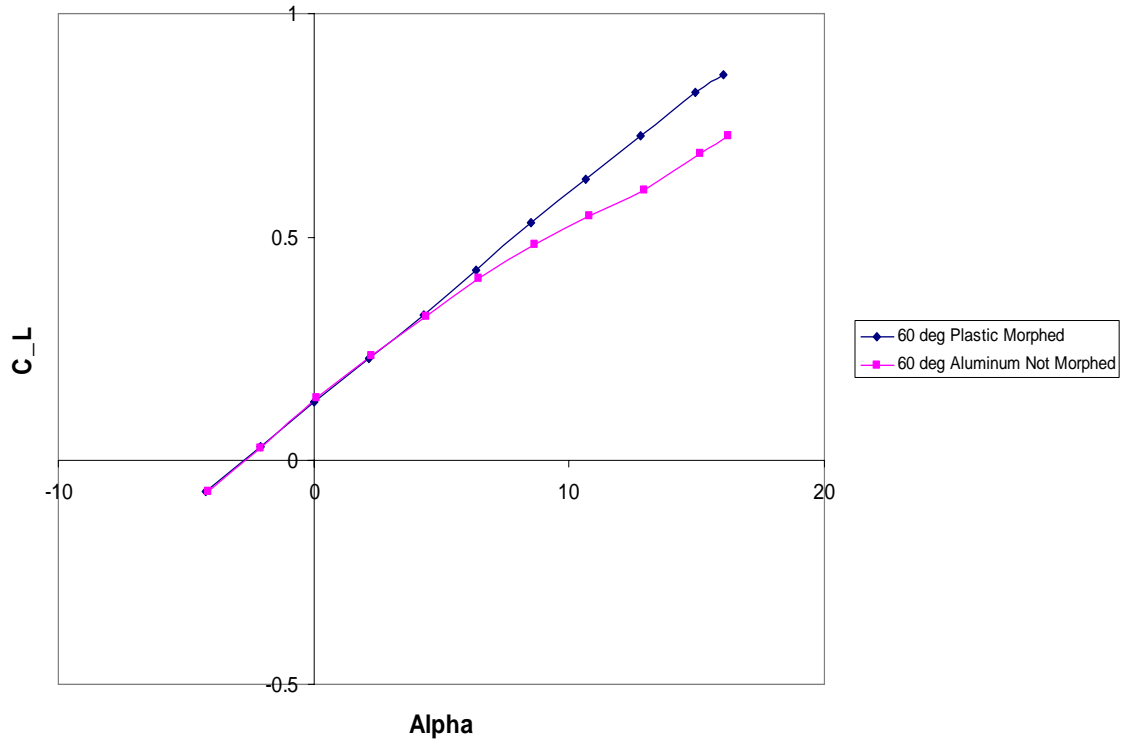


**Figure 45 Comparison of 60° joined wing plastic morphed and the aluminum at 60 mph.**

The plastic 60-degree morphed wing configuration was also tested for repetition to see if the same tests conducted on different days were producing the same results. As can be seen in Figure 46, the results of the two tests conducted at 145 mph were identical. This infers that the data taken is reproducible and accurate. Repeatability is also shown in Appendix A among the runs of different speeds producing similar coefficients at the same angles of attack.

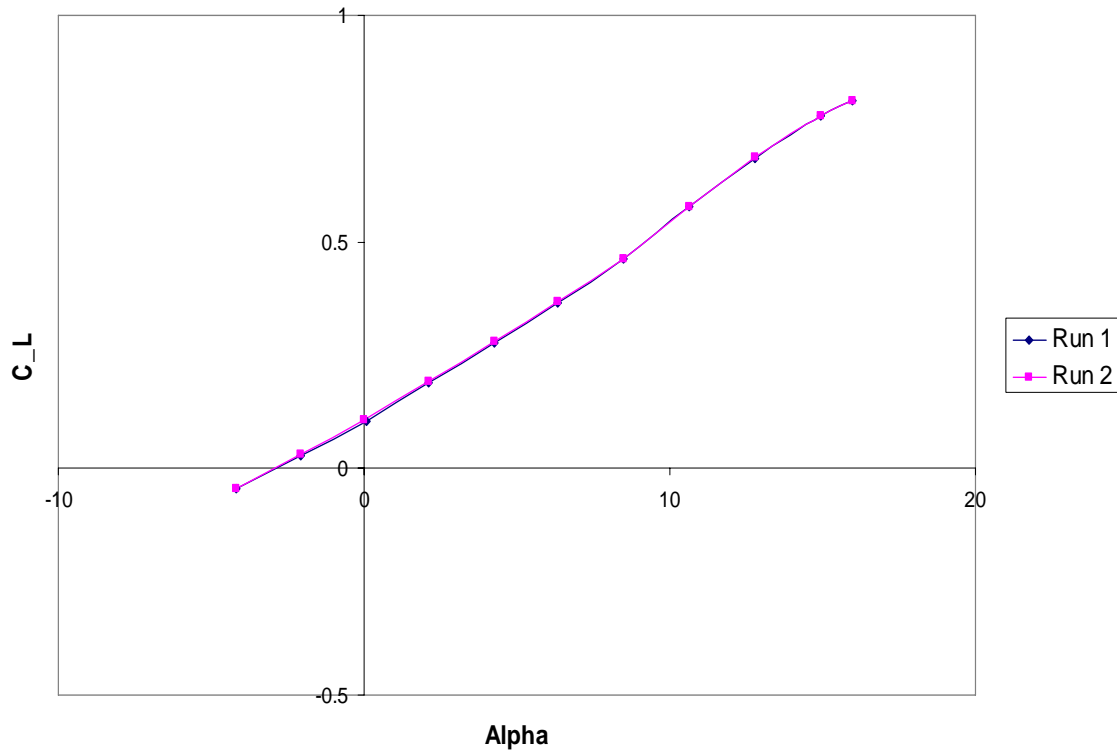


**Figure 46 Comparison between two runs on the 60° plastic morphed wing testing for repetition at 145 mph.**

The effects of pitching moment stability were compared among the different wing configurations at each test speed shown in Figure 47 through Figure 51. As the wings morph from 90 to 30 degrees, the pitching moment slope becomes less negative, but there are no major discrepancies to indicate major control issues. It is important to note that every configuration at every speed, the  $C_{M,0}$  is negative. This is consistent with Wolkovitch [22, 23], who states that the joined wing configuration induces a positive camber, which according to Kulhman and Ku [15], causes a negative  $C_{M,0}$ . This causes a stability problem. The missile must either fly with flaps deployed or the horizontal tail will have to be adjusted to make  $C_{M,0}$  positive for trimmed flight. The tail currently on the missile is symmetrical in camber which does not affect  $C_{M,0}$  [15]. The same result is

also found in the 30-degree swept single wing configurations found in Figures 56, 58, 60, and 62 (Appendix A), indicating that the joined wings are not solely the cause.

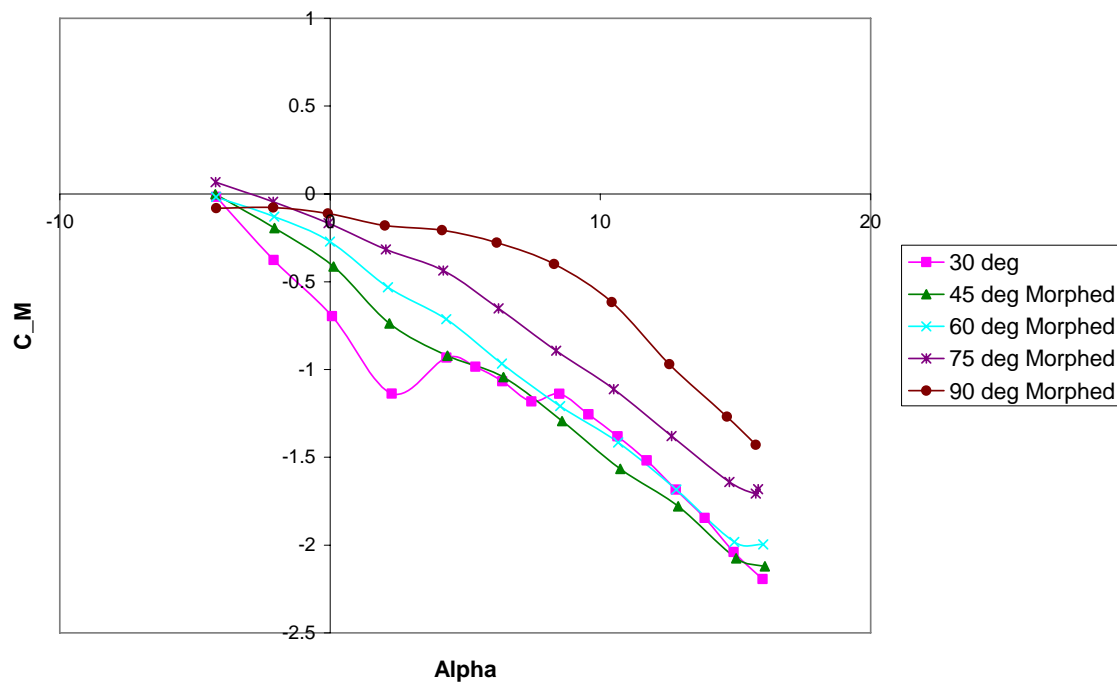


**Figure 47 Pitching moment comparison of the morphing wing set at 60 mph.**

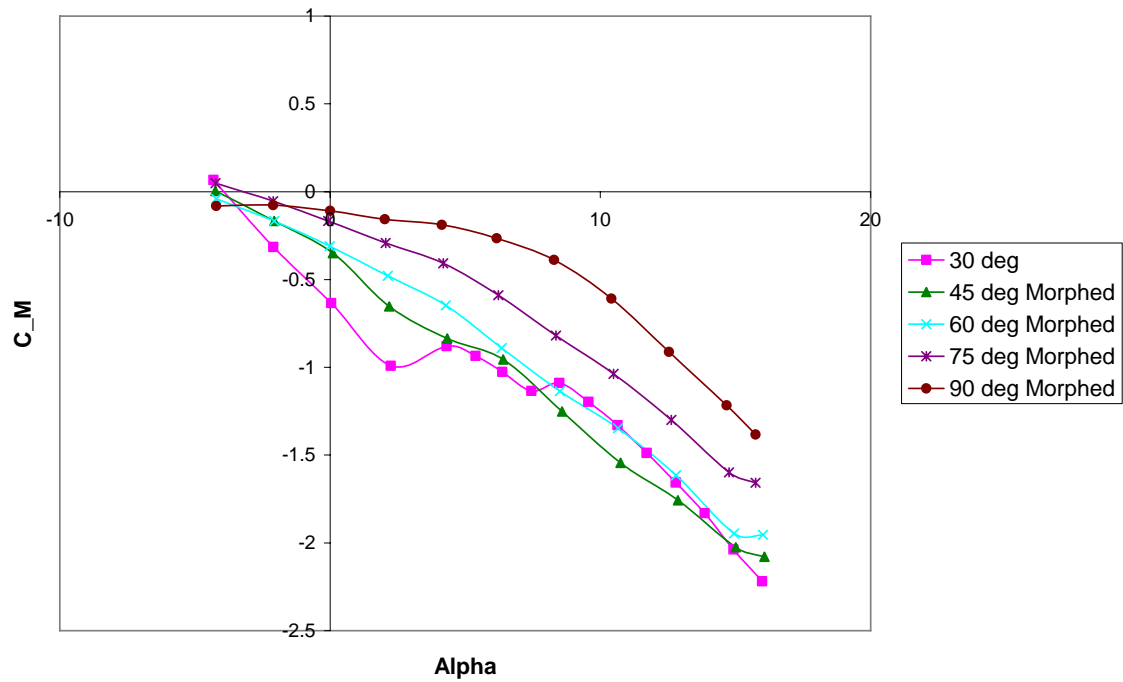


**Figure 48 Pitching moment comparison of the morphing wing set at 80 mph.**

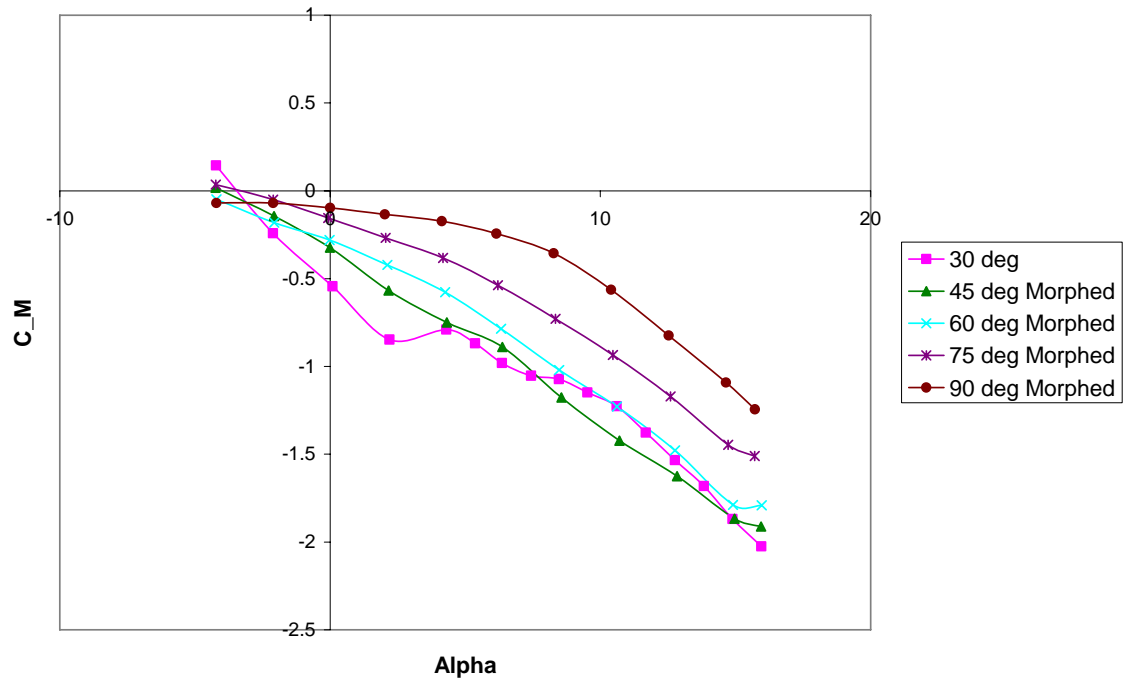


**Figure 49 Pitching moment comparison of the morphing wing set at 100 mph.**

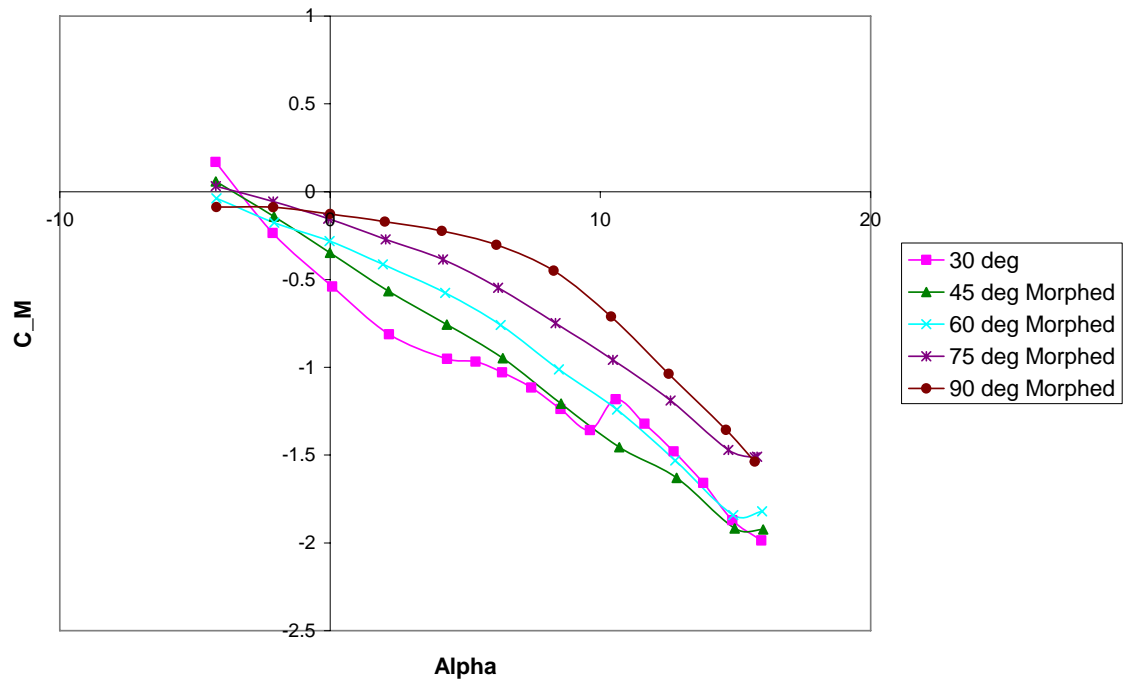


**Figure 50** Pitching moment comparison of the morphing wing set at 130 mph.

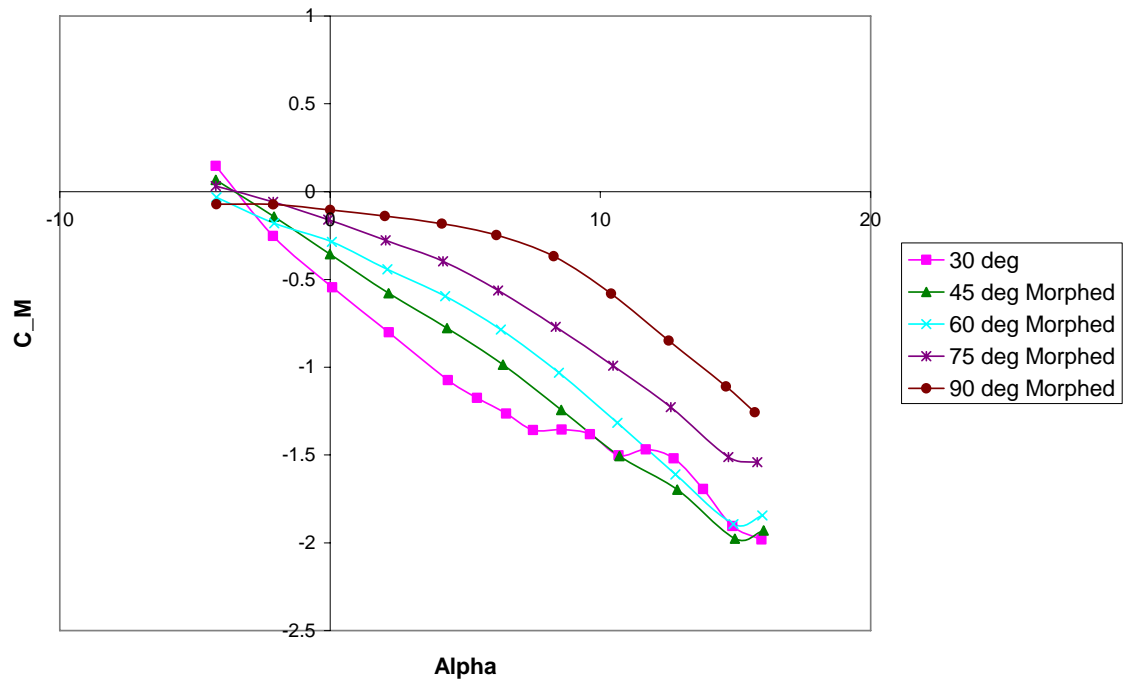


**Figure 51** Pitching moment comparison of the morphing wing set at 145 mph.

The rolling moment for all cases, at all angles of attack, is essentially zero showing stability on the rolling axis. Figure 52 shows this result for the 30-degree configuration which is the same result for all of the configurations. This stability is desired to ensure the missile with wings will not need any adverse control requirements according to Wolkovitch [22].

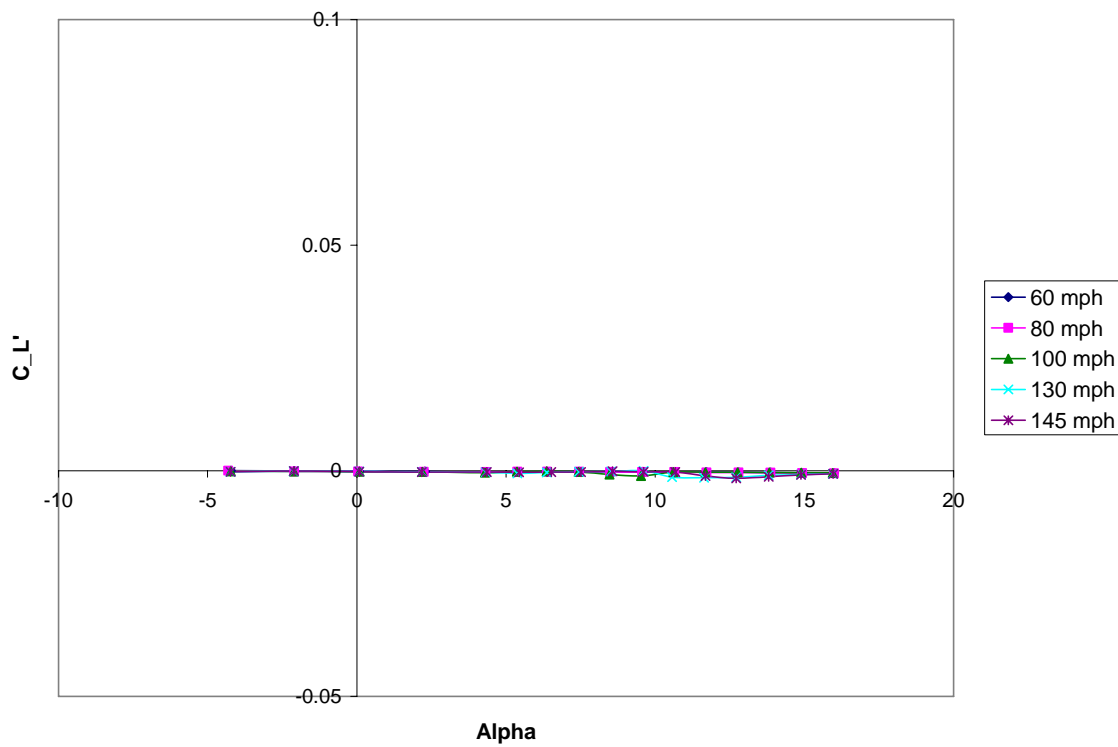


**Figure 52 Rolling Moment versus angle of Attack for 30° swept, plastic joined wing.**

## **VI. Summary**

The purpose of this study was to determine if morphing of the joined wings on a missile would cause lift, drag, or stability problems. It was shown that there were no problems with the lift, drag, or stability caused by the process of morphing. The lift and drag slopes increased and the pitching moment slope decreased as the wings opened to their full extension. The 30-degree swept joined wing does show wing stall at low angles of attack. While the exact reasons could not be determined, it is probable that the low Reynolds number and thinness of the wings may be part of the cause.

Future endeavors should include, testing wing models at a larger Reynolds number and increased wing thickness. To increase the Reynolds number, the chord length and/or the test velocity need to be increased. Another idea would be designing and testing a wing model of the scissors morphing concept with moving mechanisms. Other morphing concepts should also be designed and investigated then compared to find the one that is the most beneficial. Finally, testing should also be conducted in the compressibility regime, because the missile will most likely fly in this regime.

## **Appendix A**

The following pages contain the lift and drag coefficient relations as well as pitch and roll coefficient relations for all of the configurations tested.

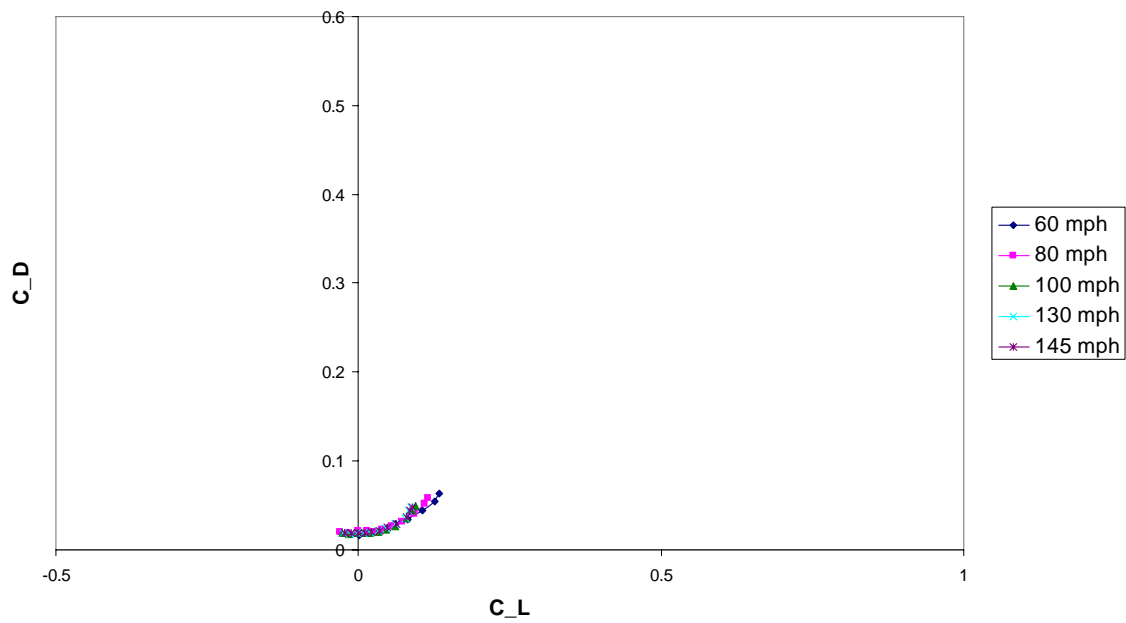
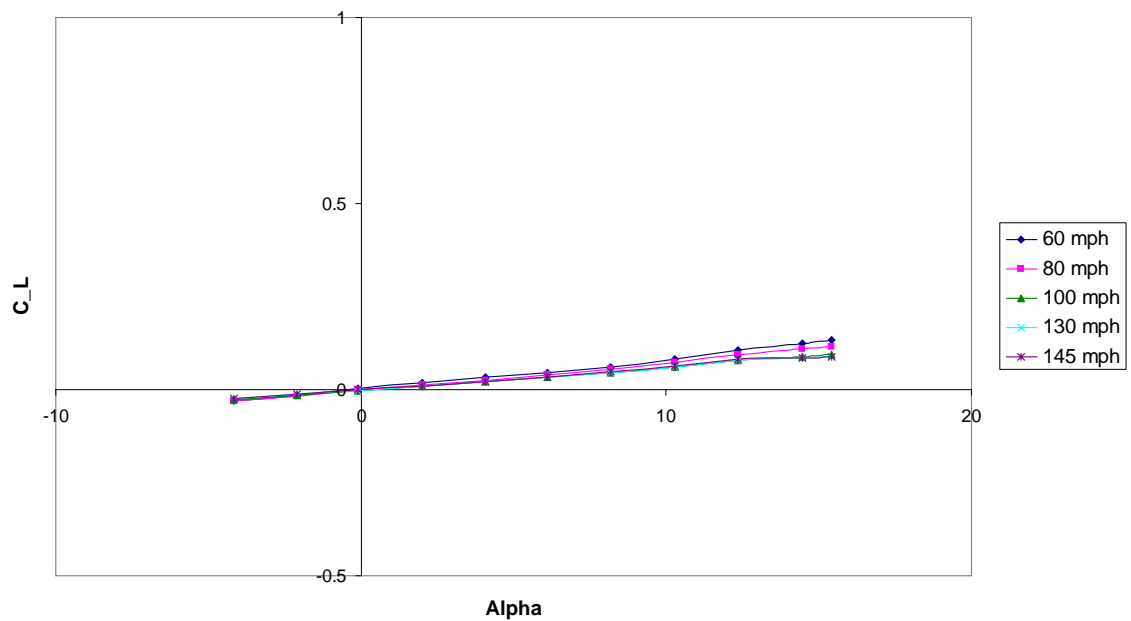


**Figure 53 Lift and drag relations of the bare missile.**

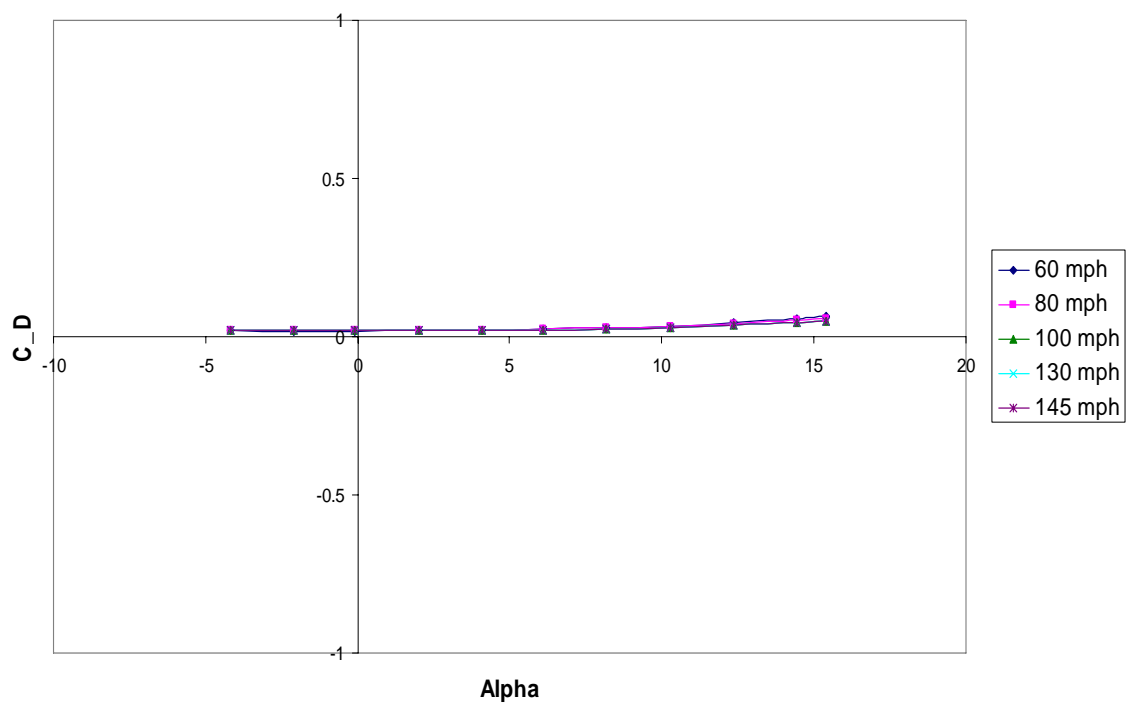


**Figure 54** Drag relations of the bare missile.

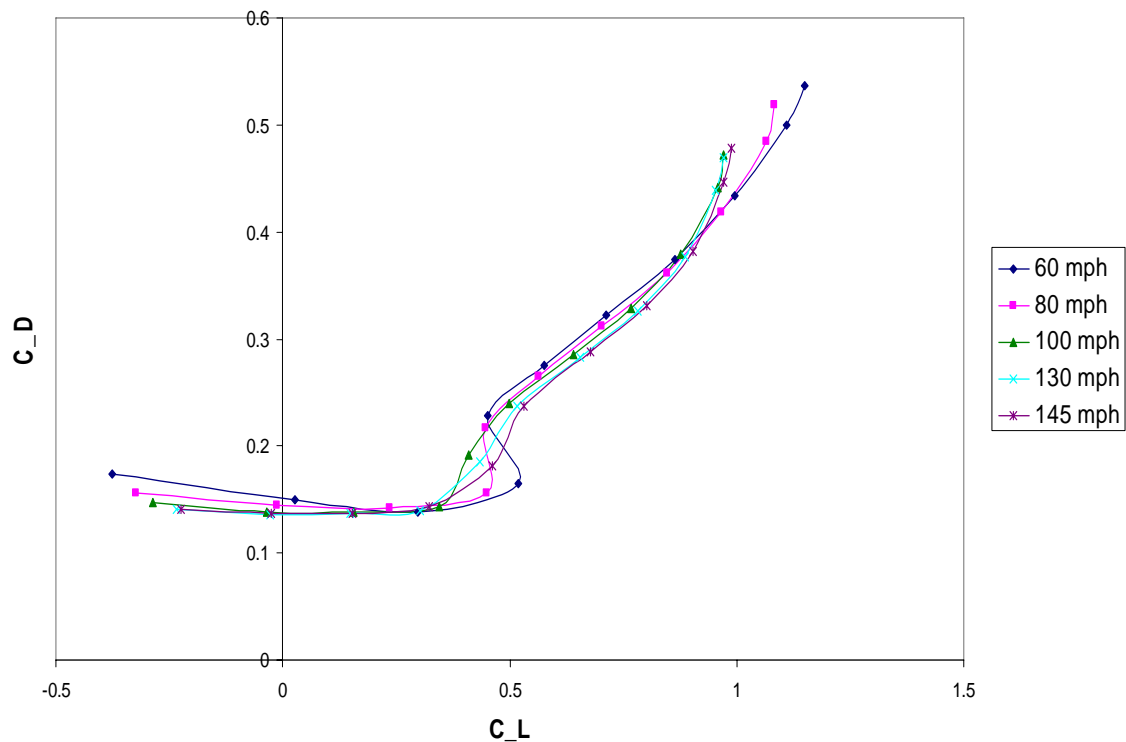
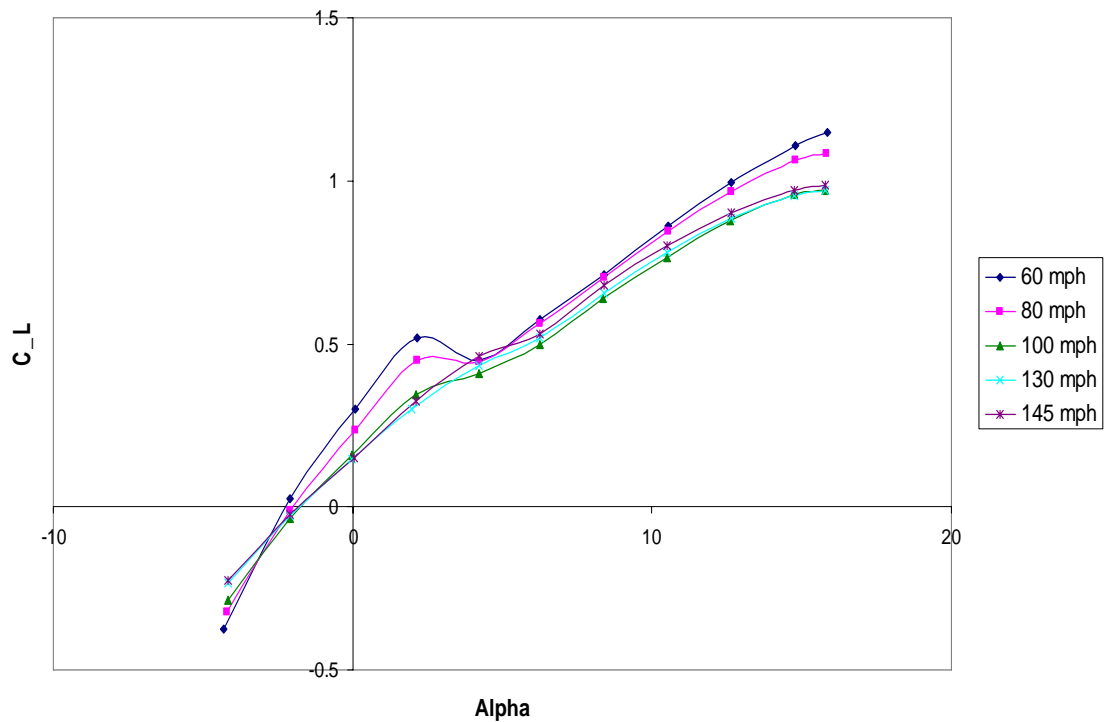


**Figure 55 Lift and drag Relations of 30° swept single wing located forward of CG, wings on bottom, aluminum.**

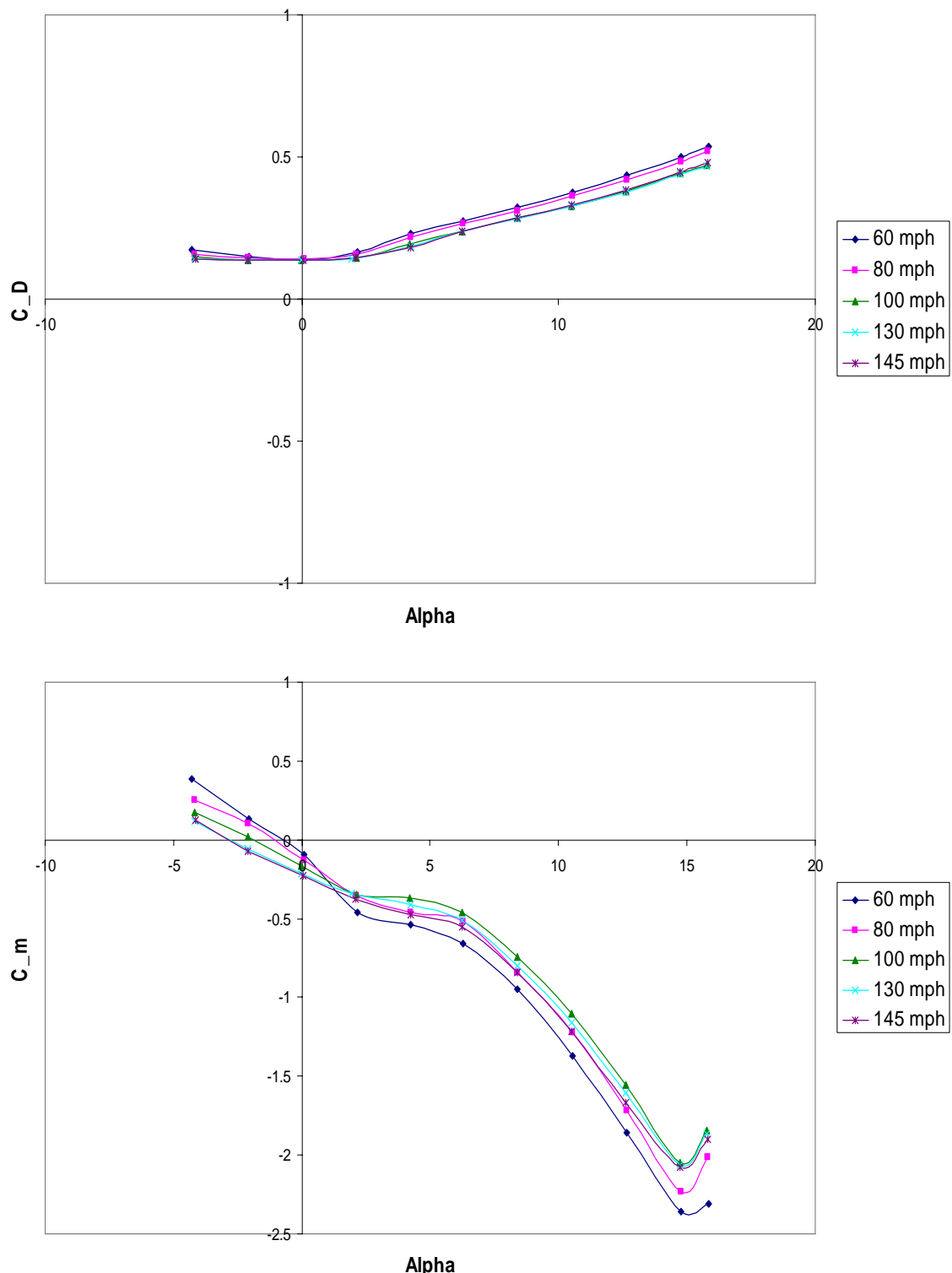


**Figure 56 Drag and pitch relations of the  $30^\circ$  swept single wing located forward of the CG, wings on bottom, aluminum.**

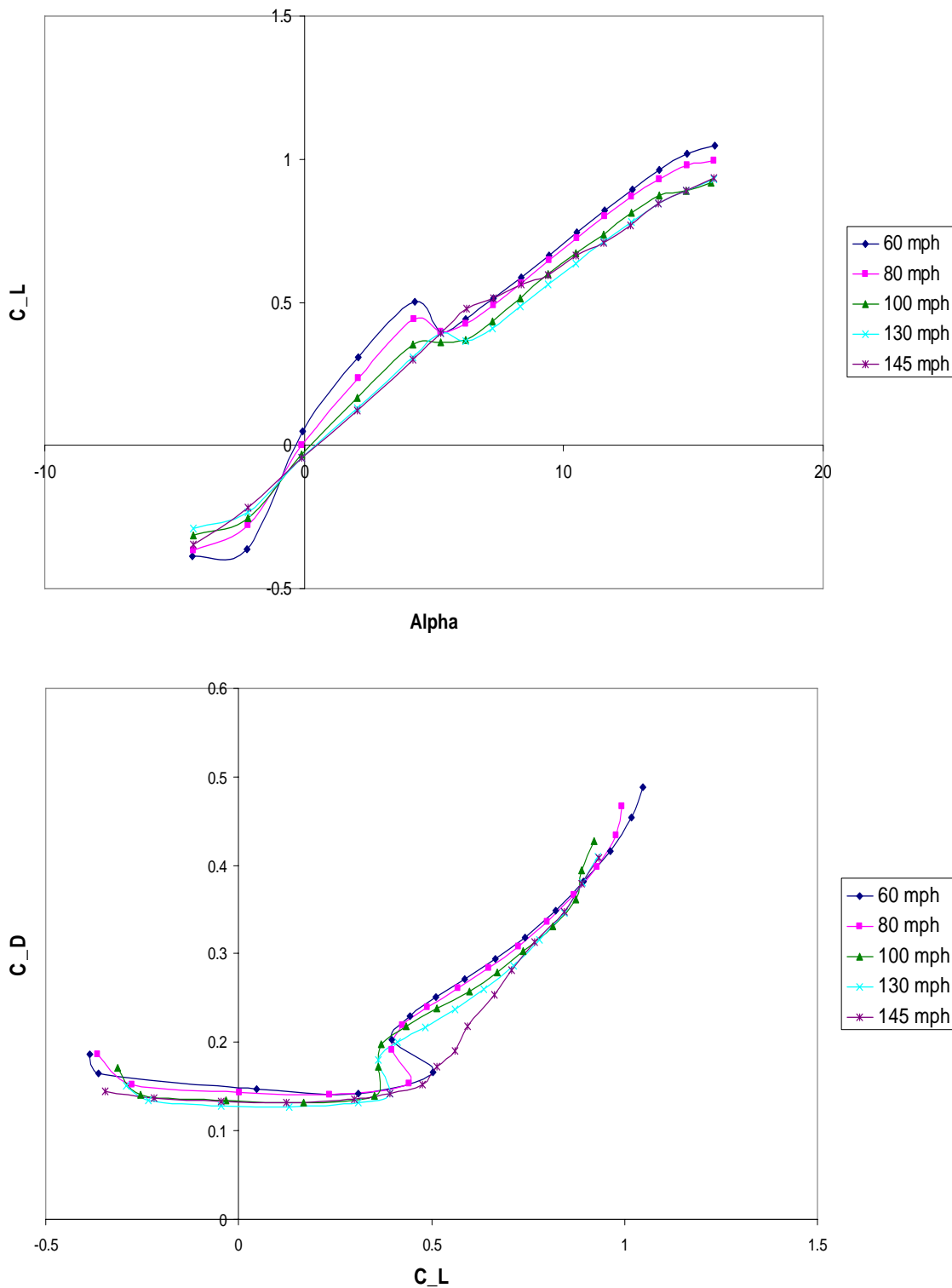


**Figure 57** Lift and drag relations of the  $30^\circ$  swept single wing located forward of the CG, wings on bottom, plastic.

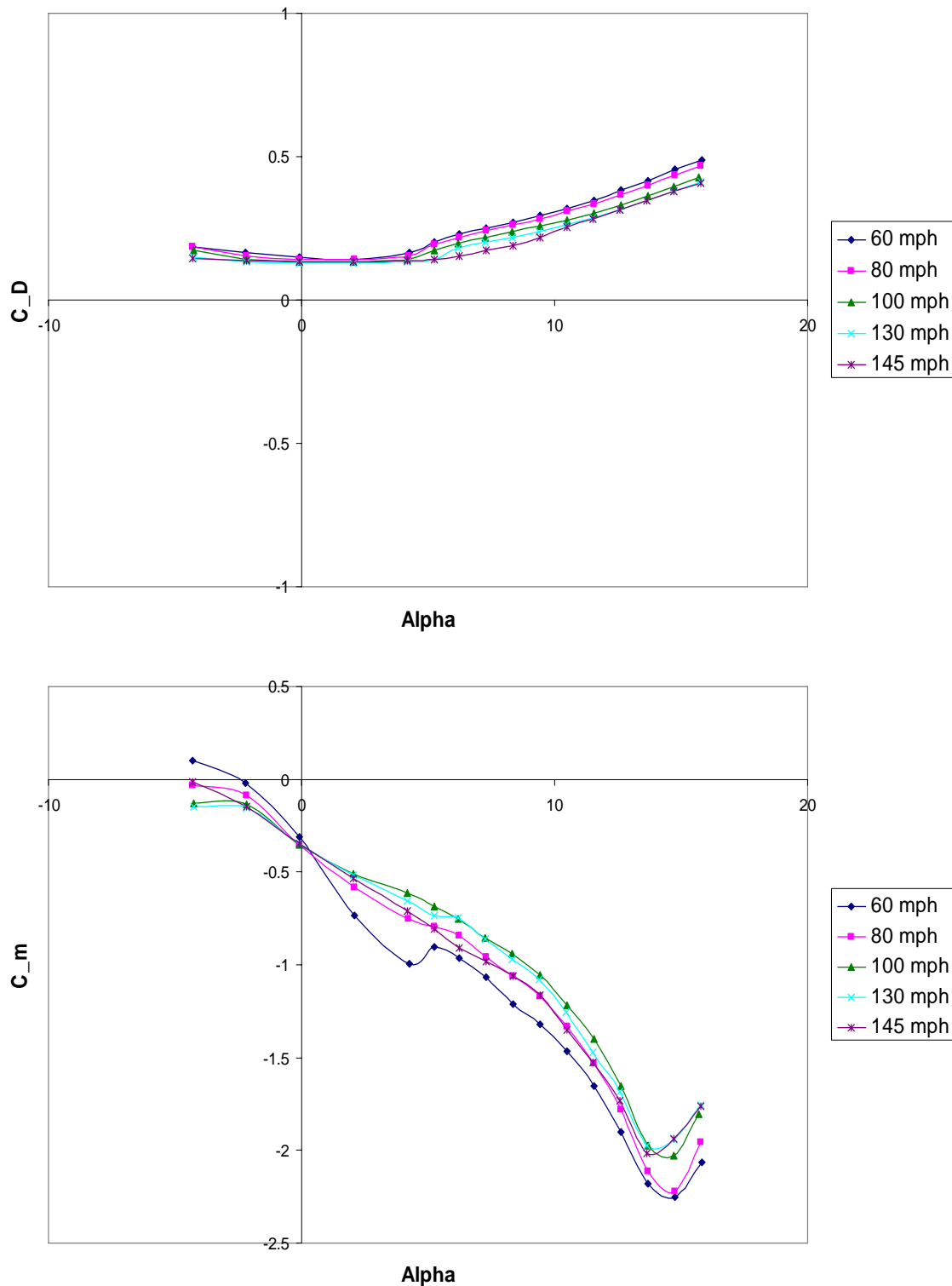


**Figure 58 Drag and pitch relations of the  $30^\circ$  swept single wing located forward of the CG, wings on bottom, plastic.**

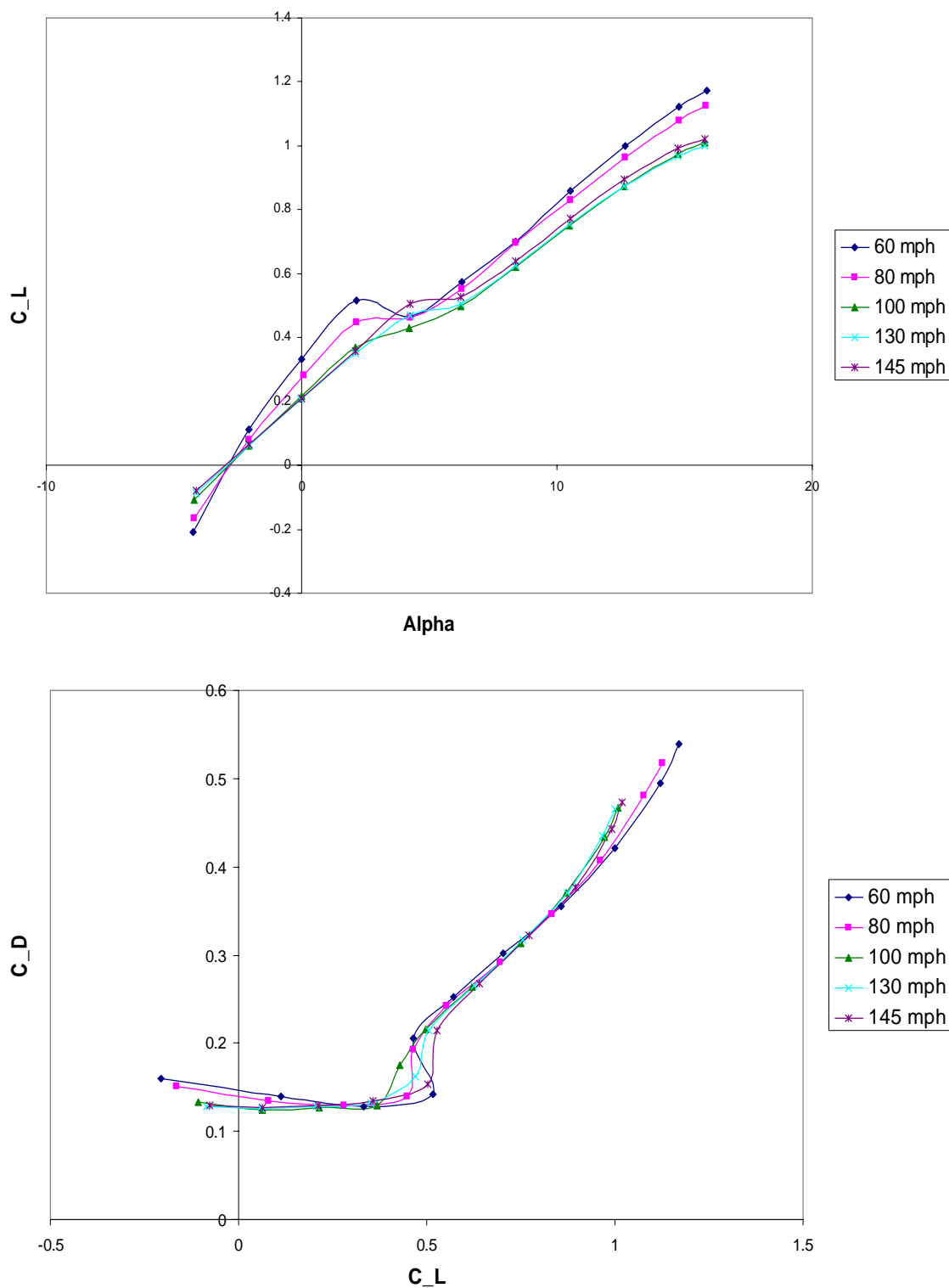


**Figure 59 Lift and drag relations of 30° swept single wing located aft of CG, wings on top, aluminum.**

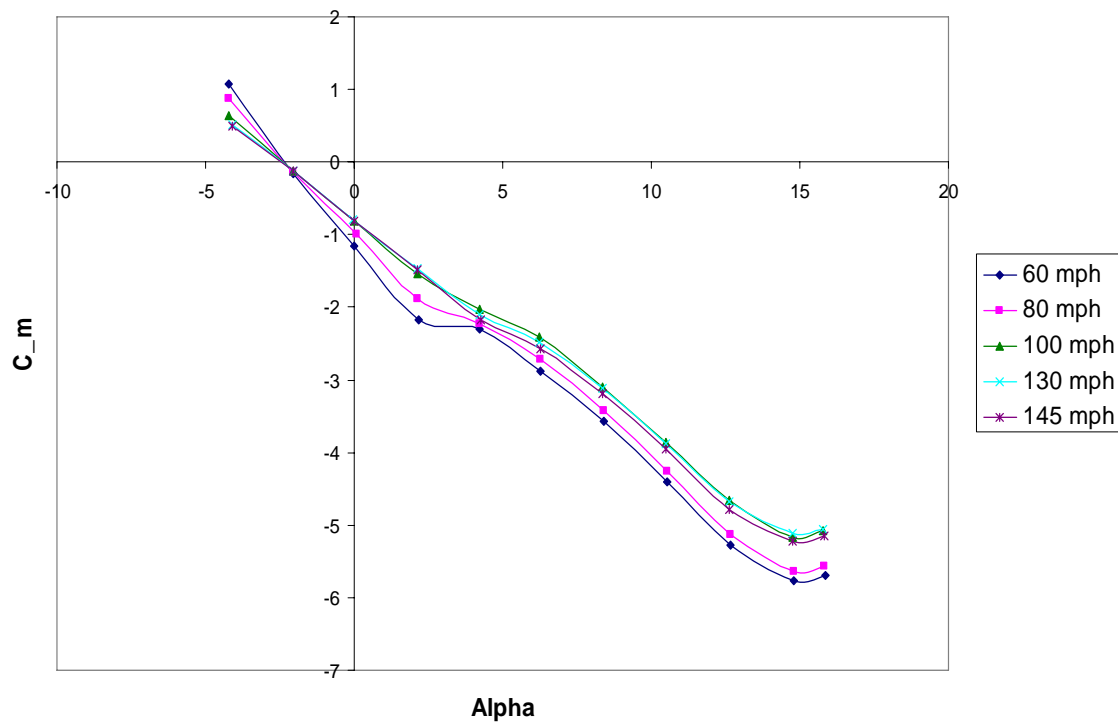
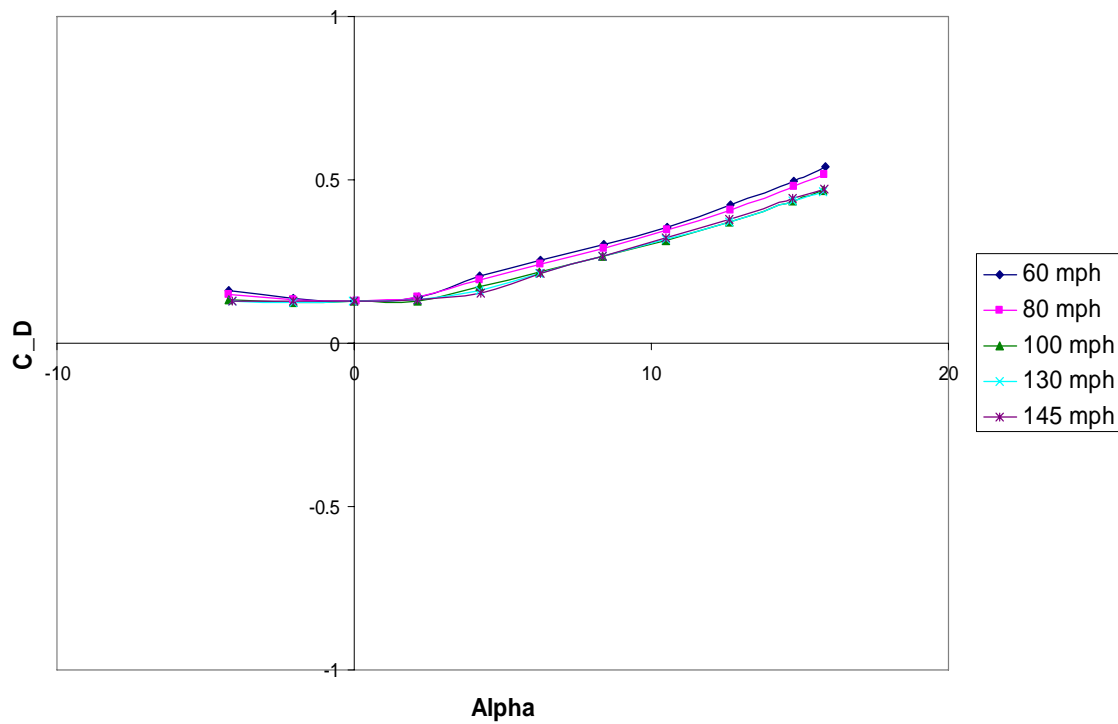


**Figure 60 Drag and pitch relations of the 30° swept single wing located aft of CG, wings on top, aluminum.**

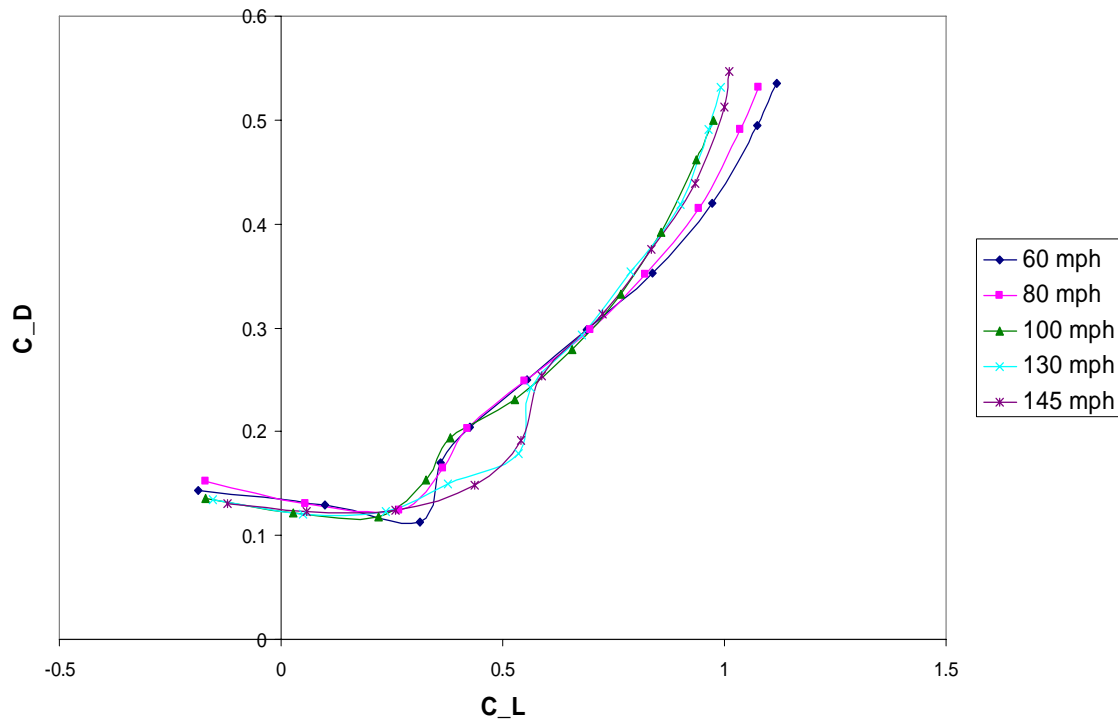
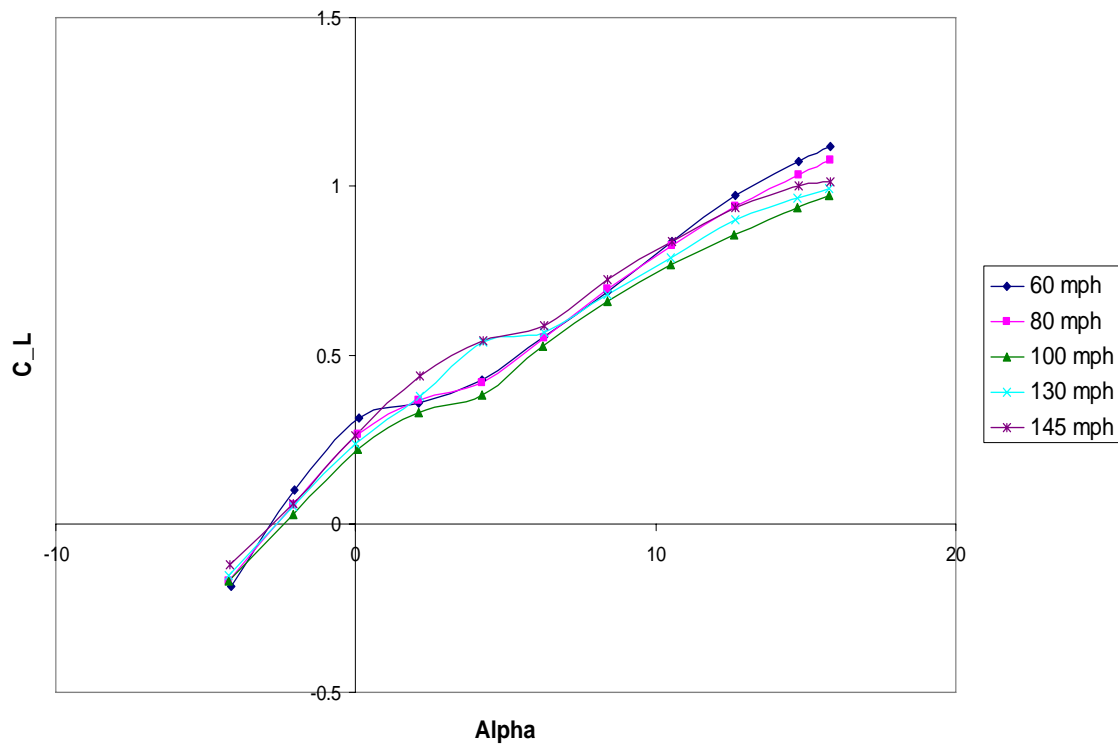


**Figure 61** Lift and drag relations of the  $30^\circ$  swept single wing located aft of CG, wings on top, plastic.

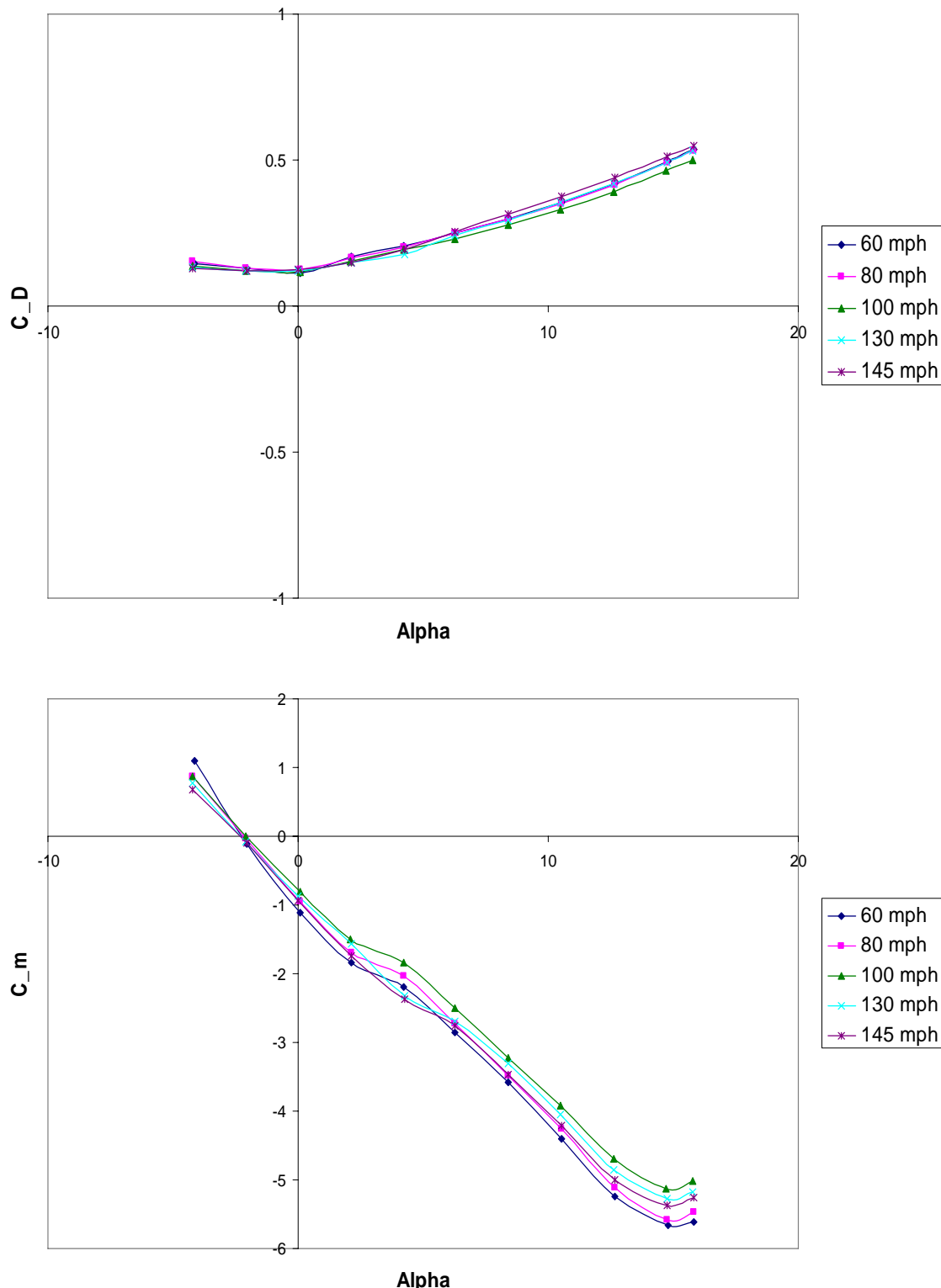


**Figure 62 Drag and pitch relations of the 30° swept single wing located aft of CG, wings on top, plastic.**

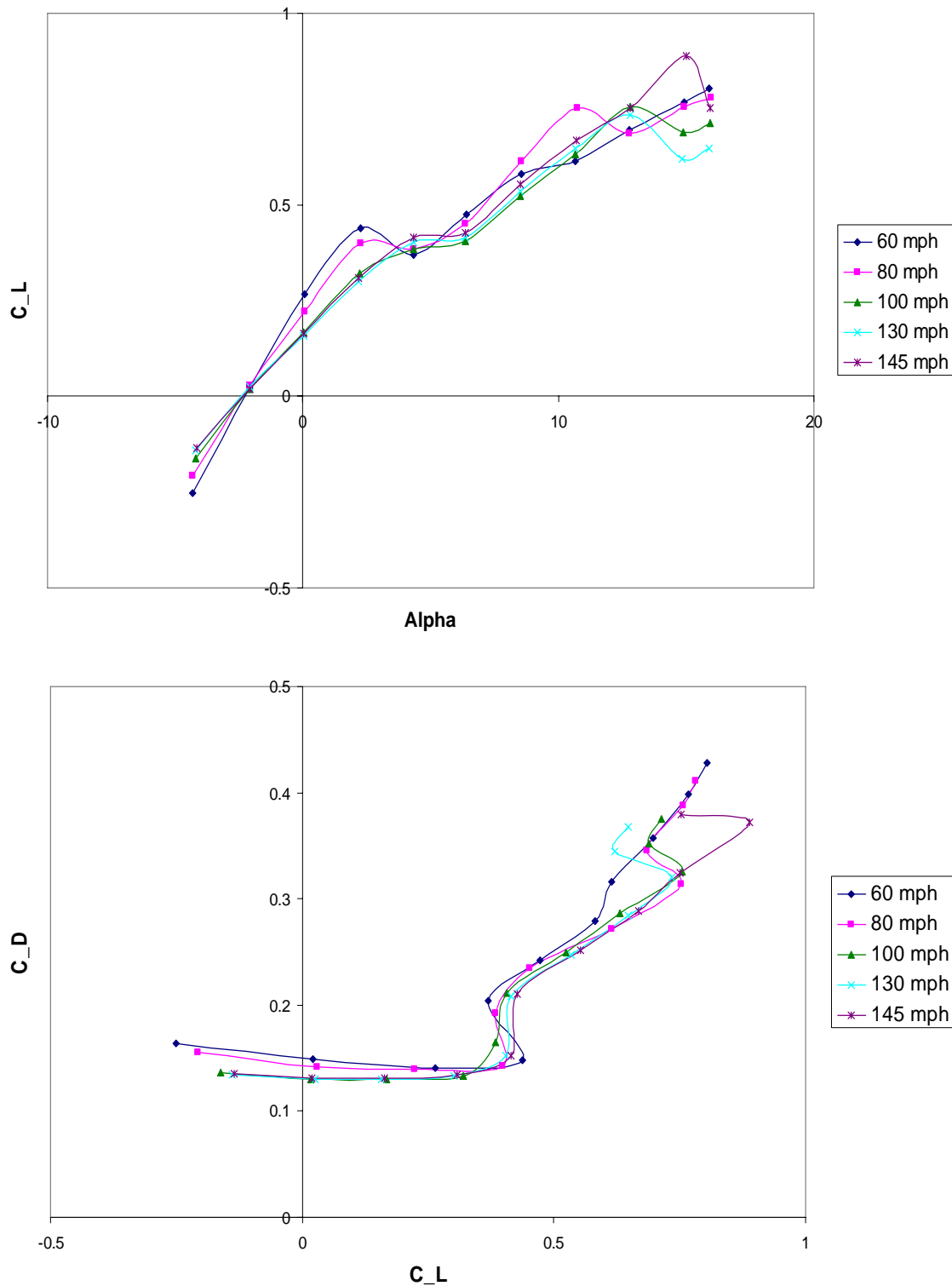


**Figure 63 Lift and drag relations of 30° swept joined wing, aluminum.**

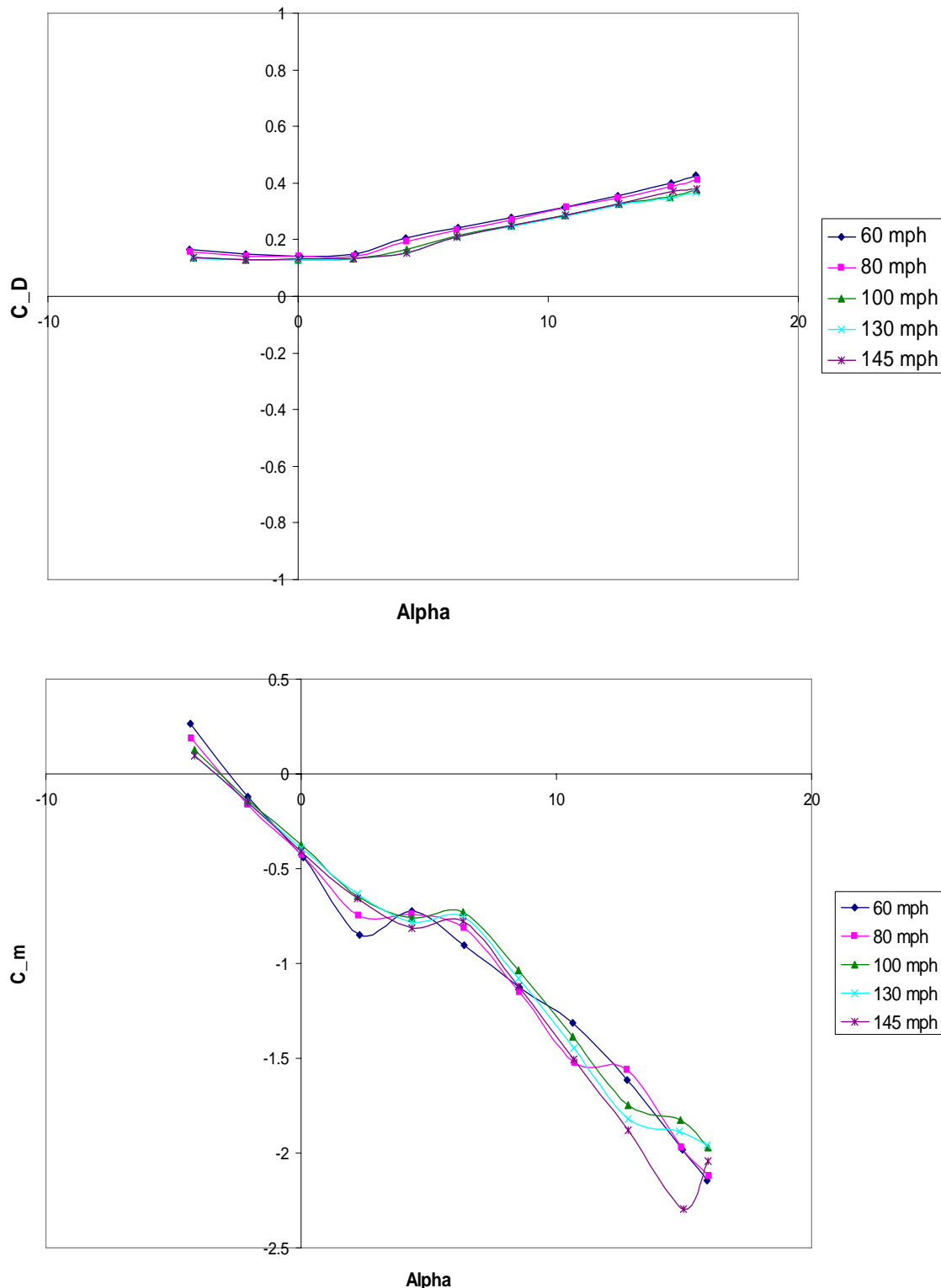


**Figure 64 Drag and pitch relations of the  $30^\circ$  joined wing, aluminum.**

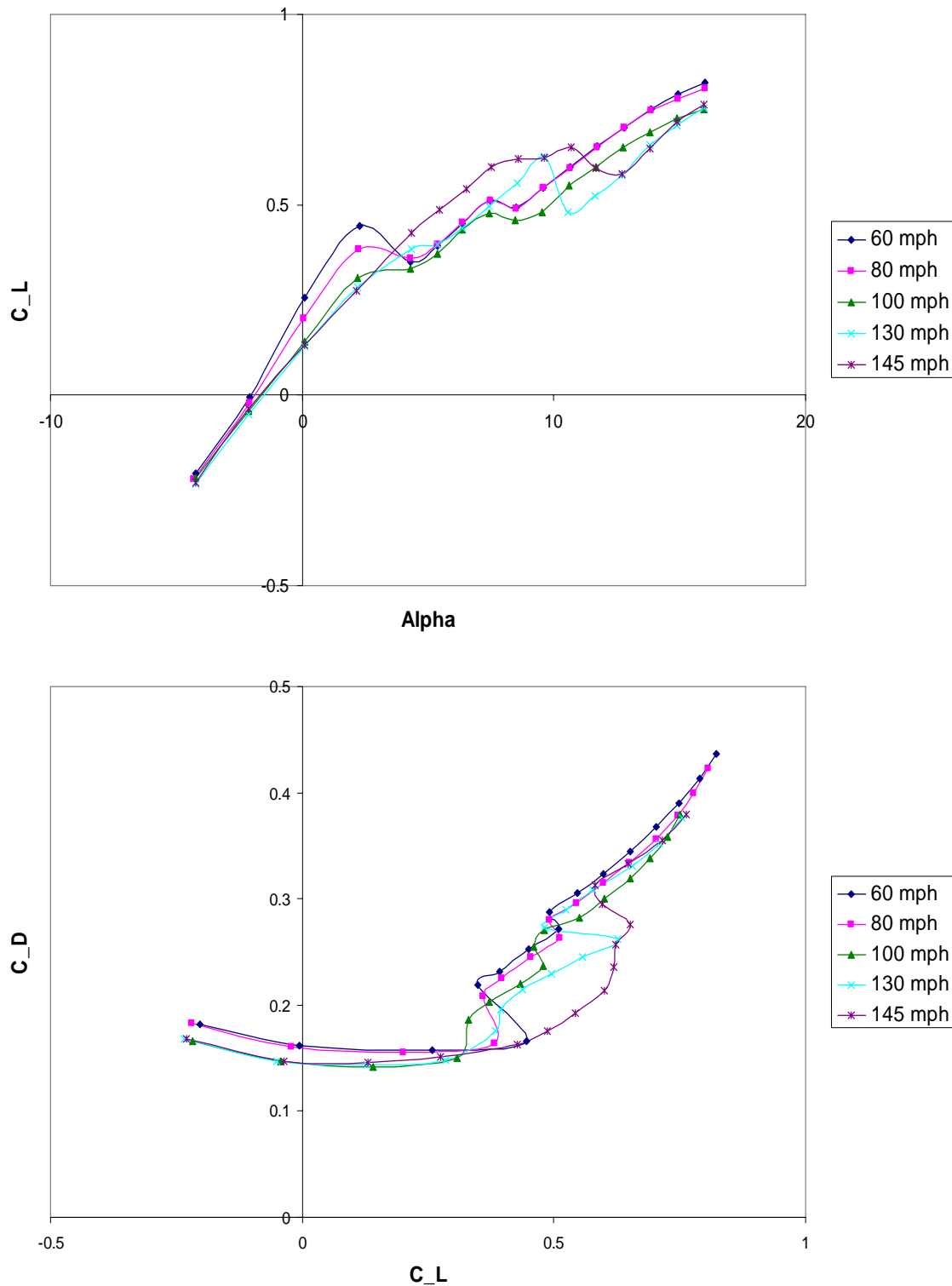


**Figure 65 Lift and drag relations of 30° swept joined wing, plastic.**

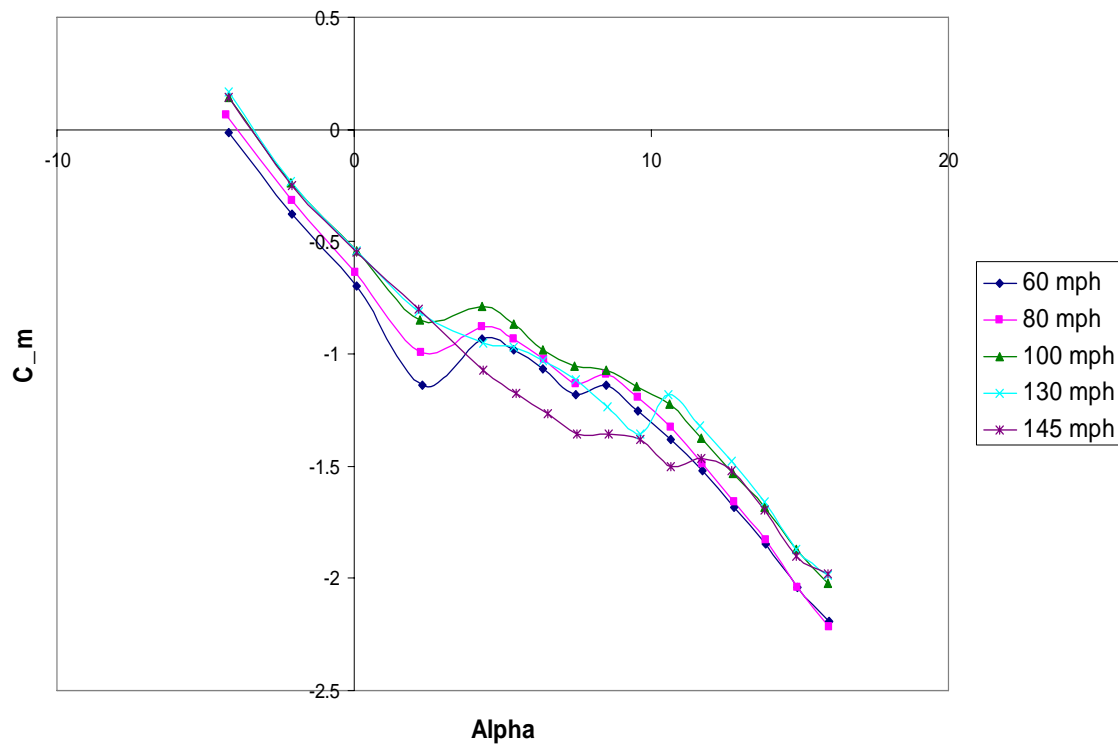
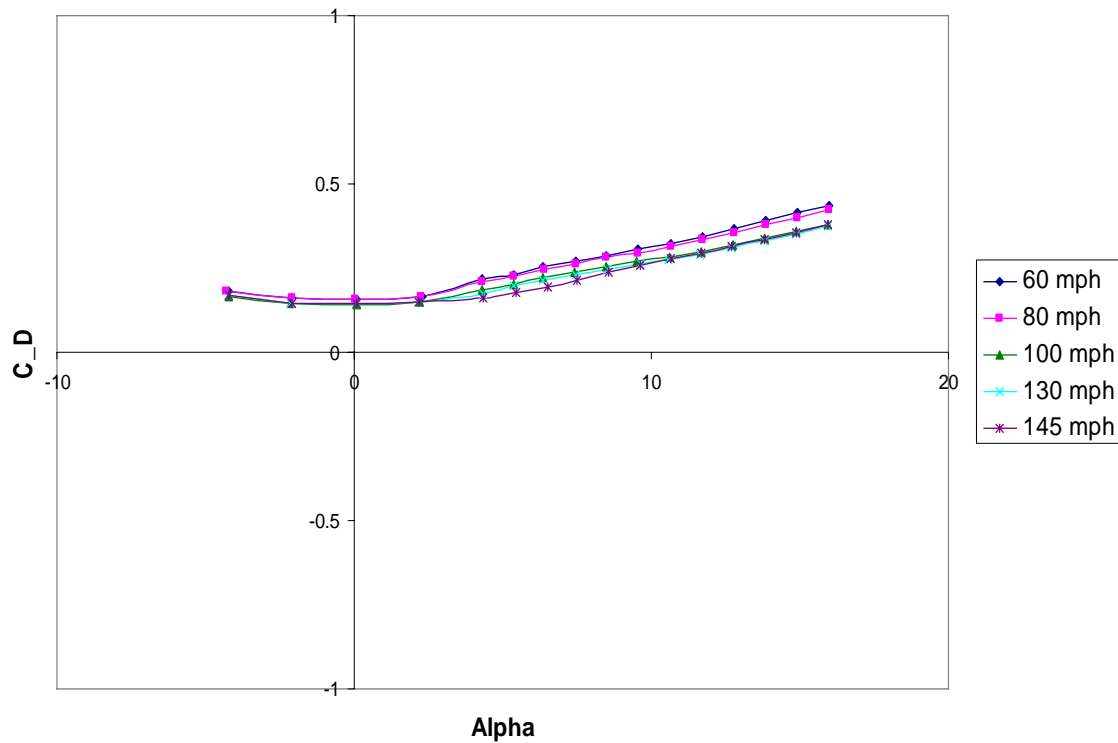


**Figure 66 Drag and pitch relations of the 30° joined wing, plastic.**

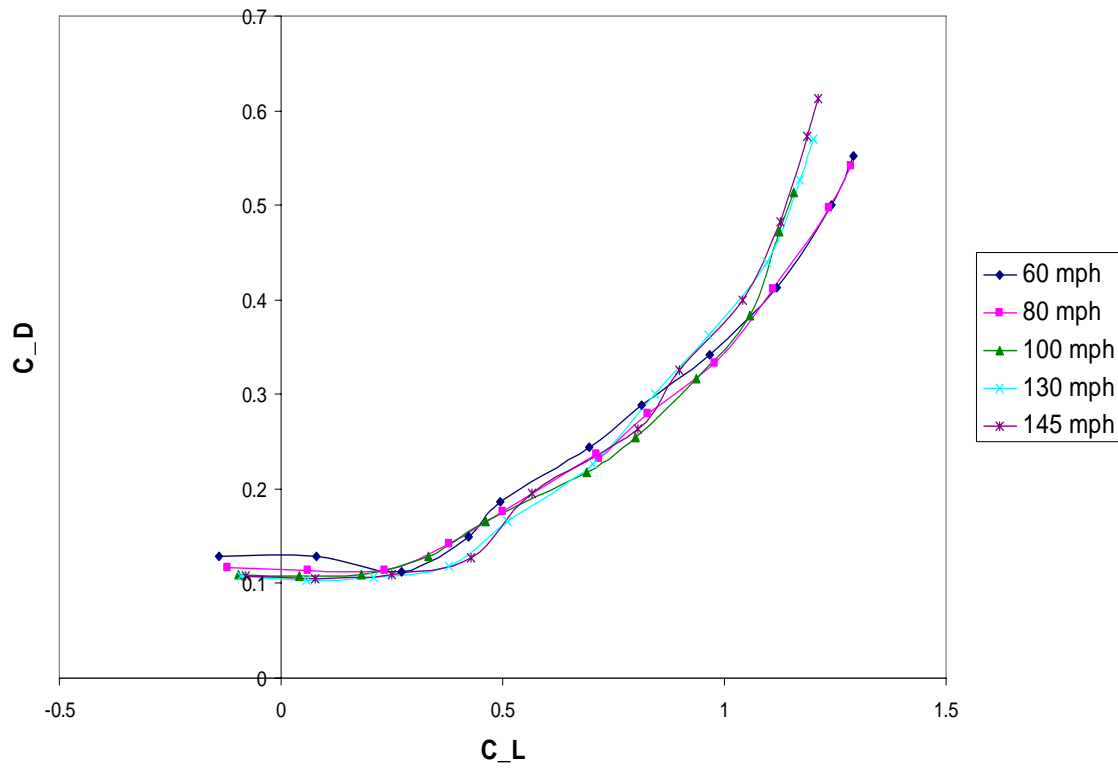
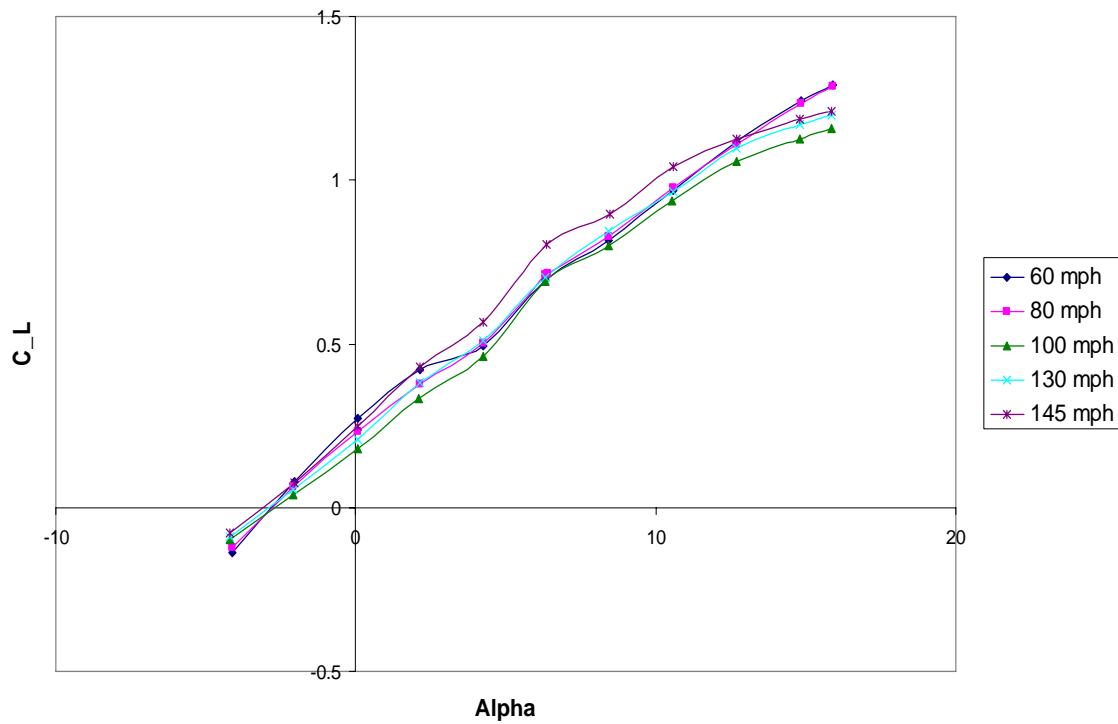


**Figure 67 Lift and drag relations of the  $45^\circ$  single wing swept forward, plastic.**

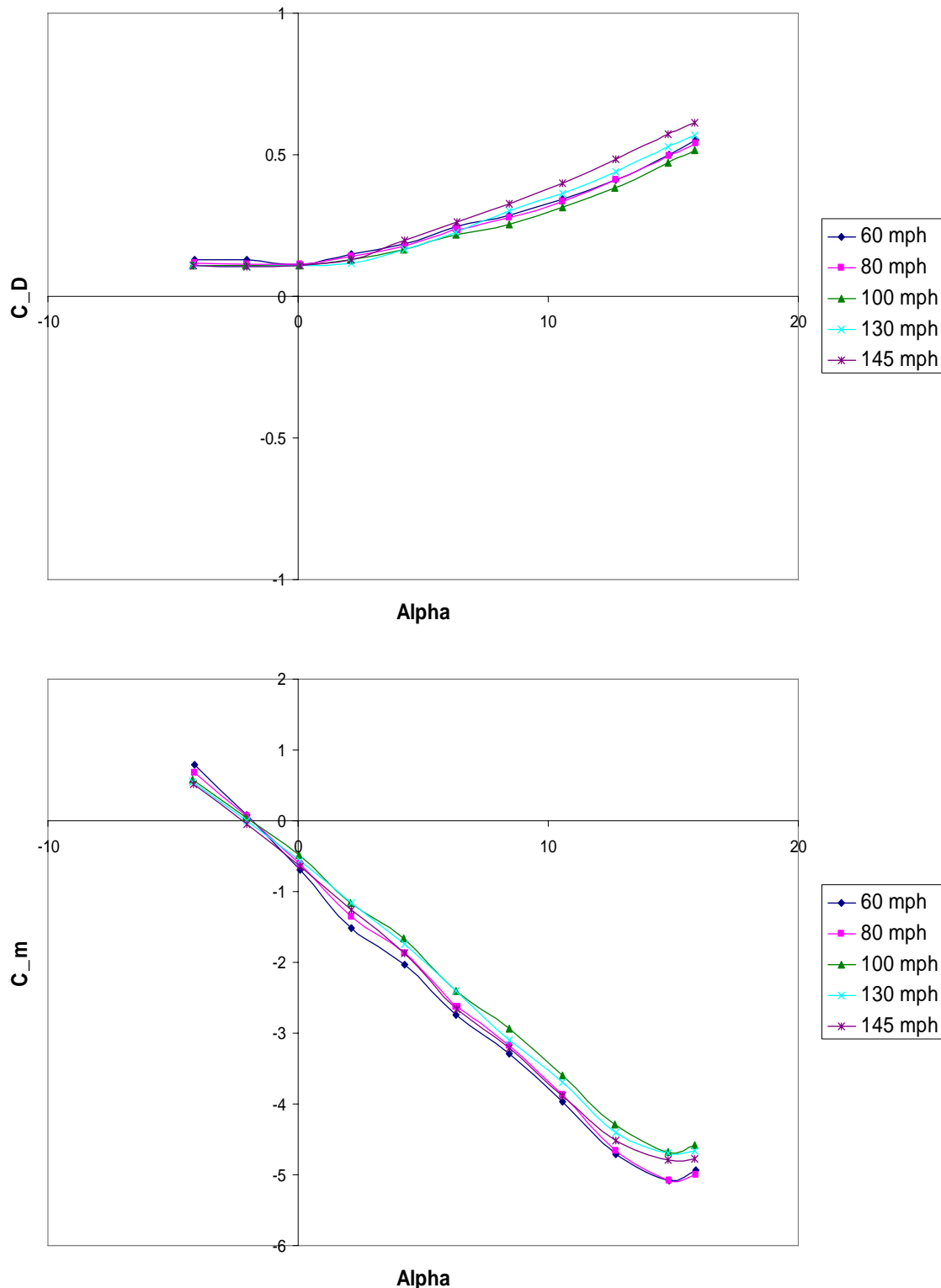


**Figure 68 Drag and pitch relations of the  $45^\circ$  single wing swept forward, plastic.**

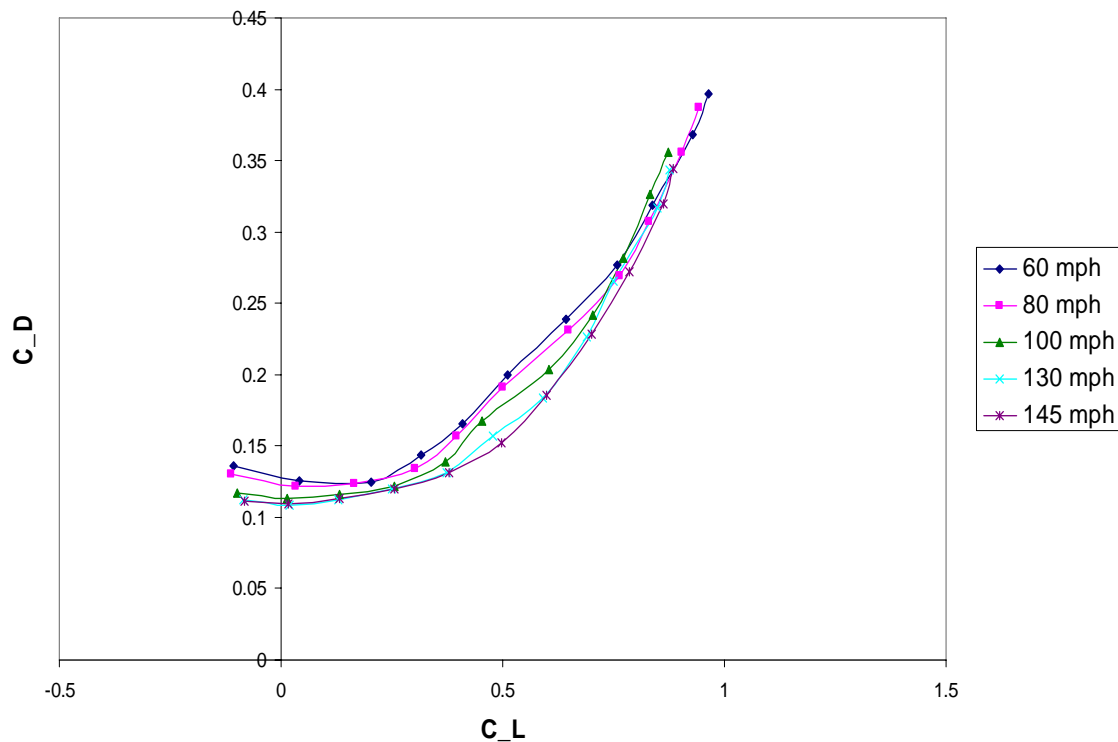
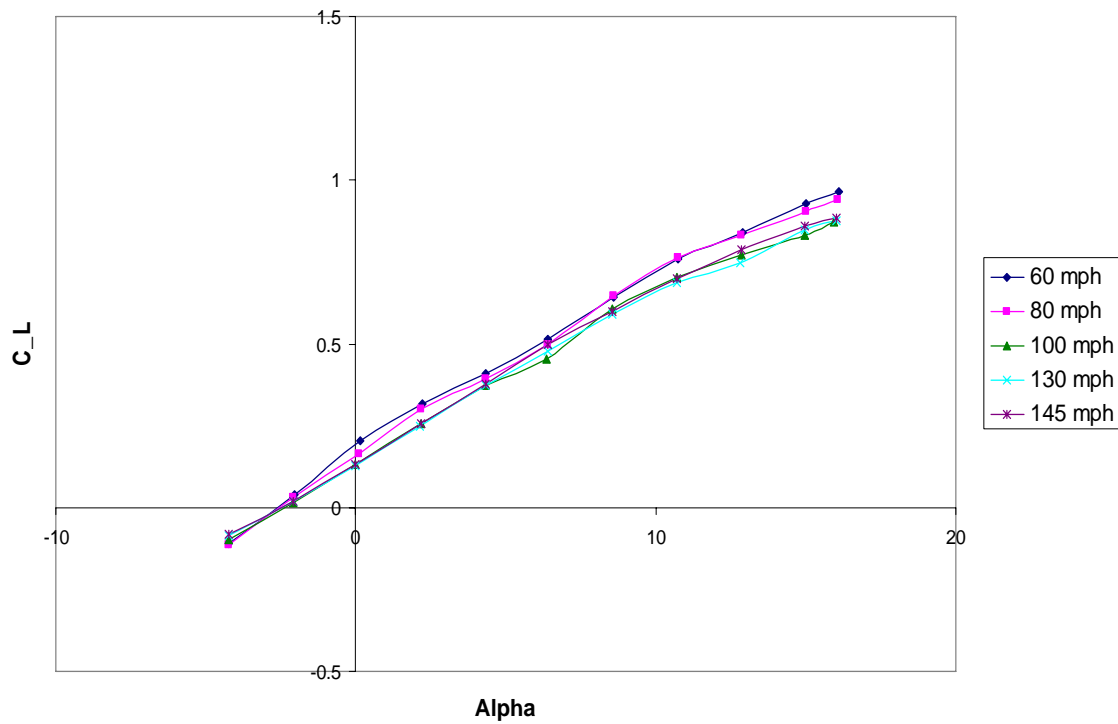


**Figure 69** Lift and drag relations of the  $45^\circ$  joined wing, plastic.

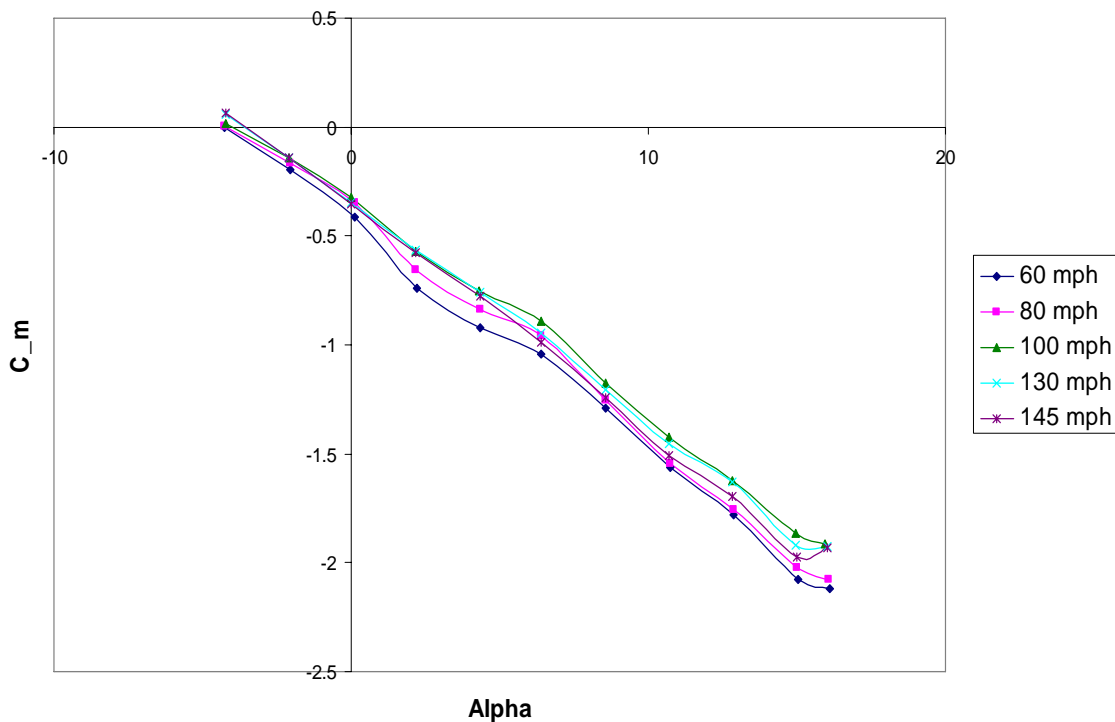
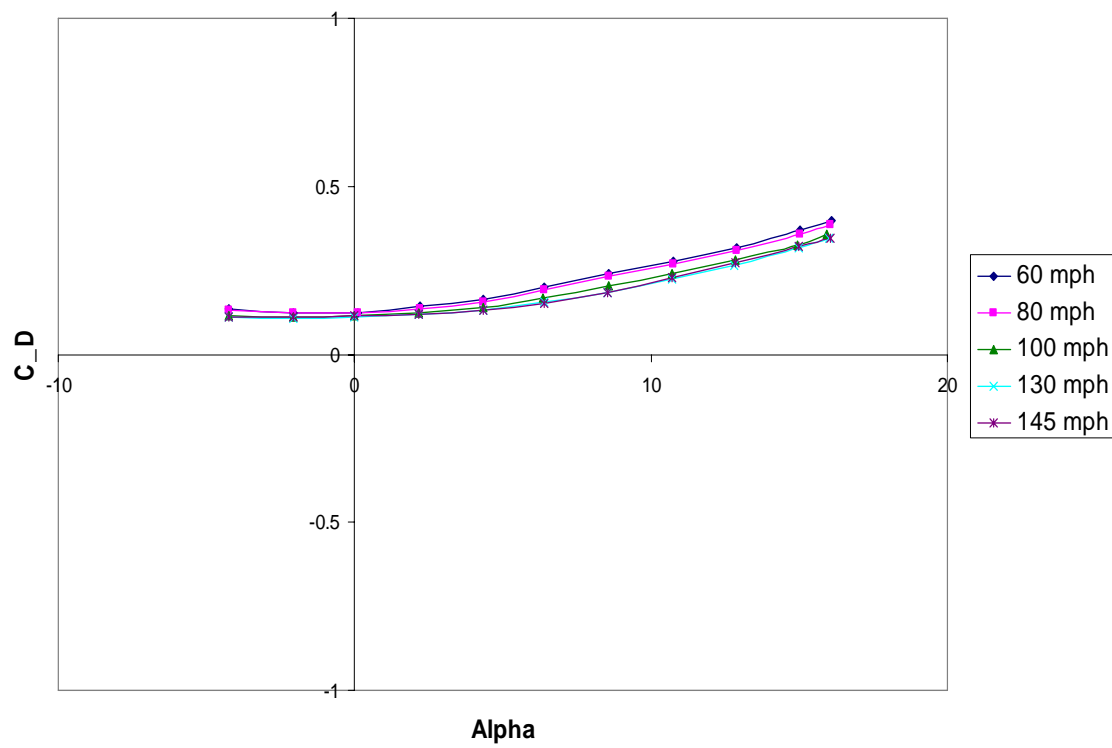


**Figure 70 Drag and pitch relations of the 45° joined wing, plastic.**

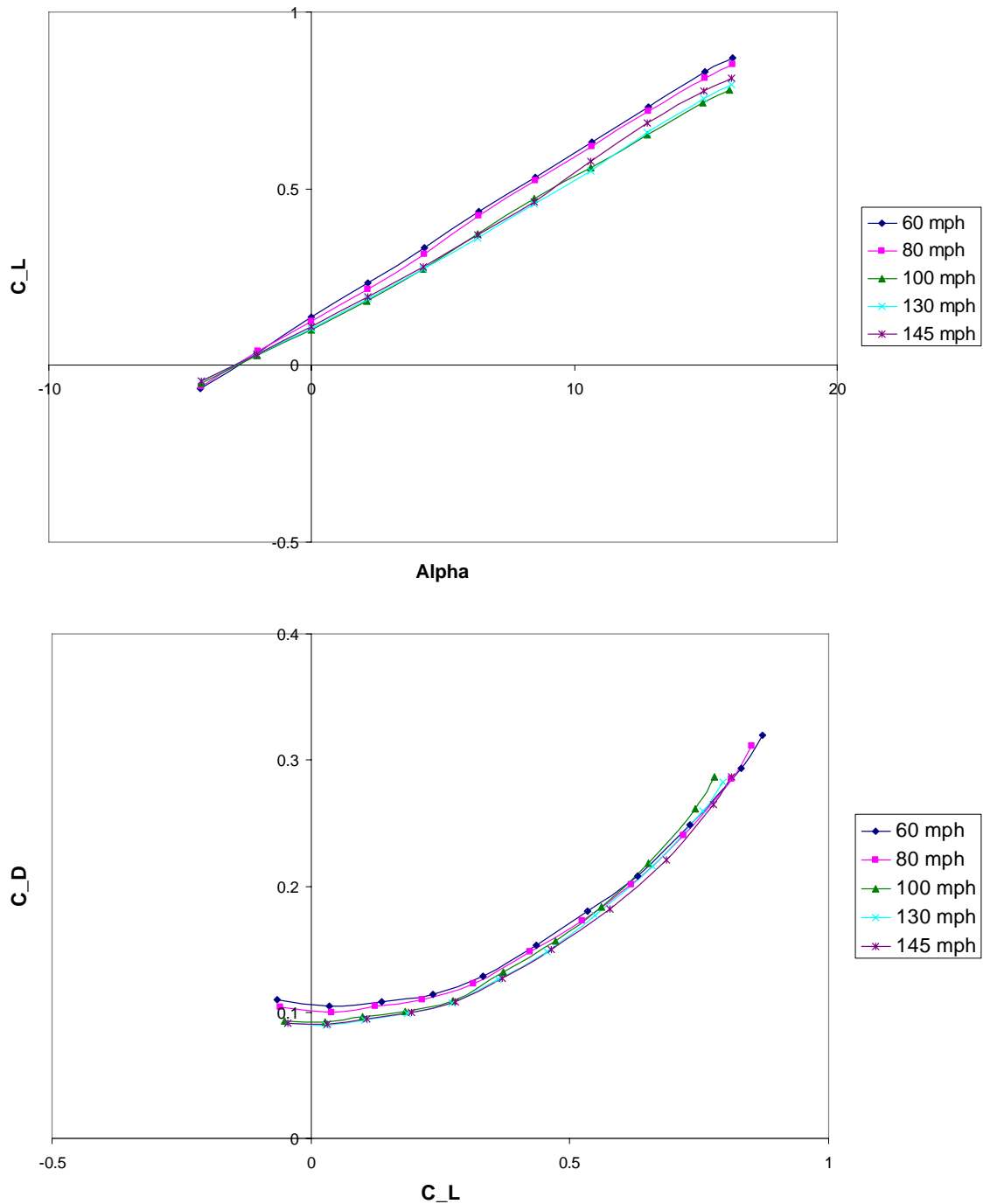


**Figure 71 Lift and drag relations of the  $60^\circ$  joined wing, plastic.**

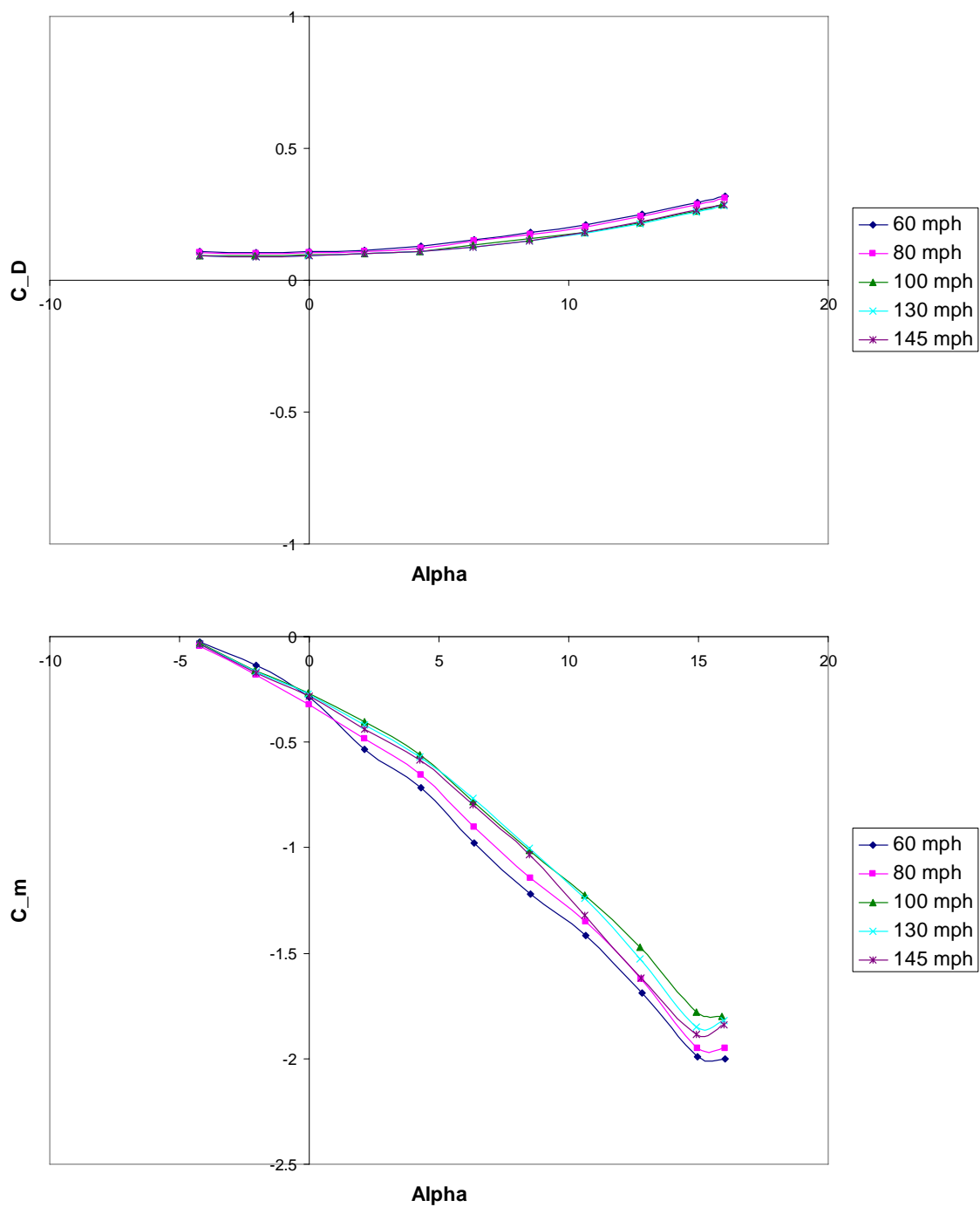


**Figure 72 Drag and pitch relations of the  $60^\circ$  joined wing, plastic.**

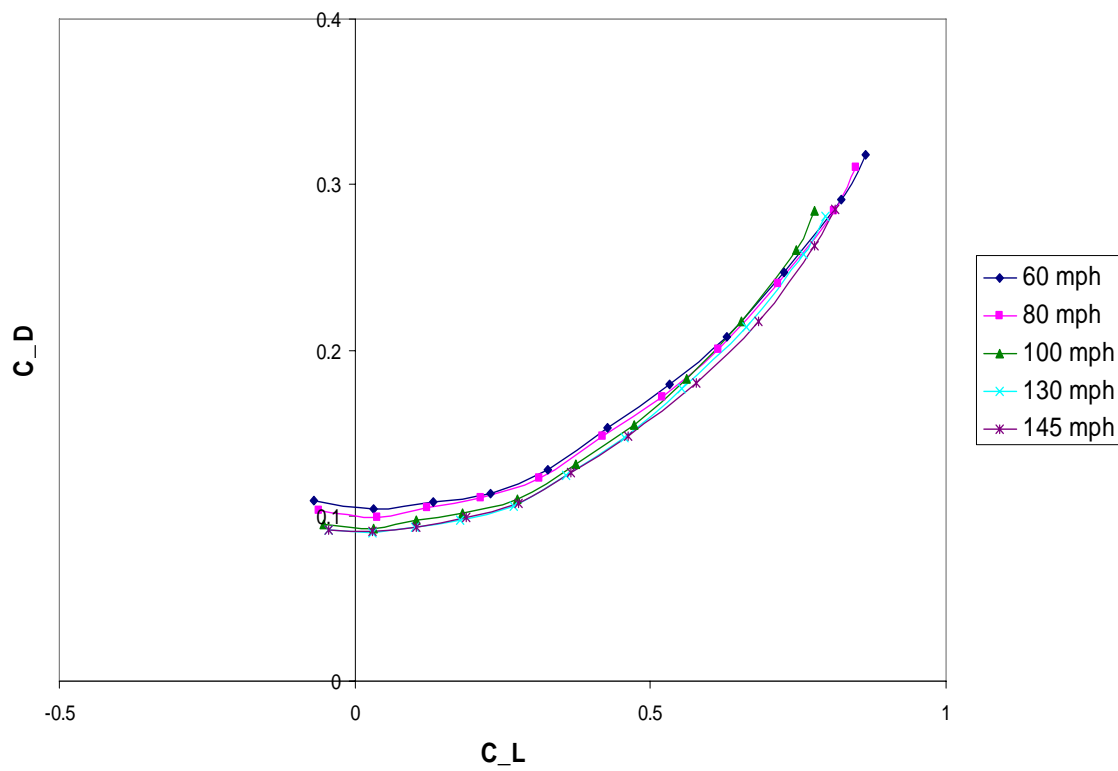
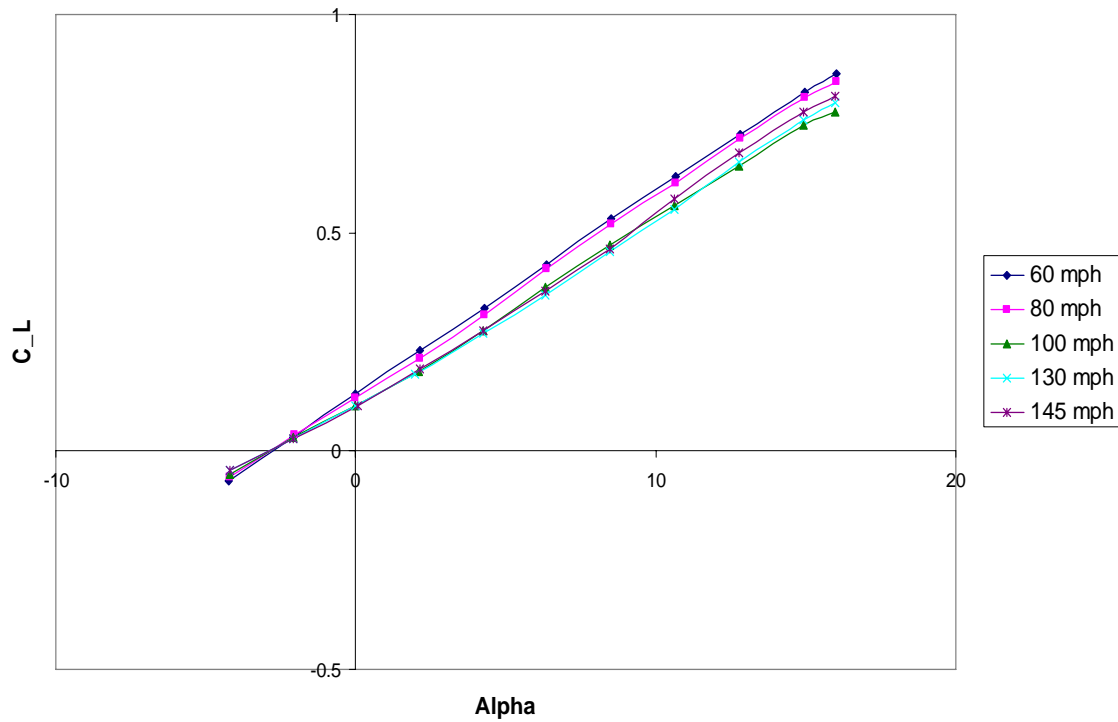


**Figure 73 Lift and drag relations of the  $60^\circ$  joined wing, plastic. Second Run.**

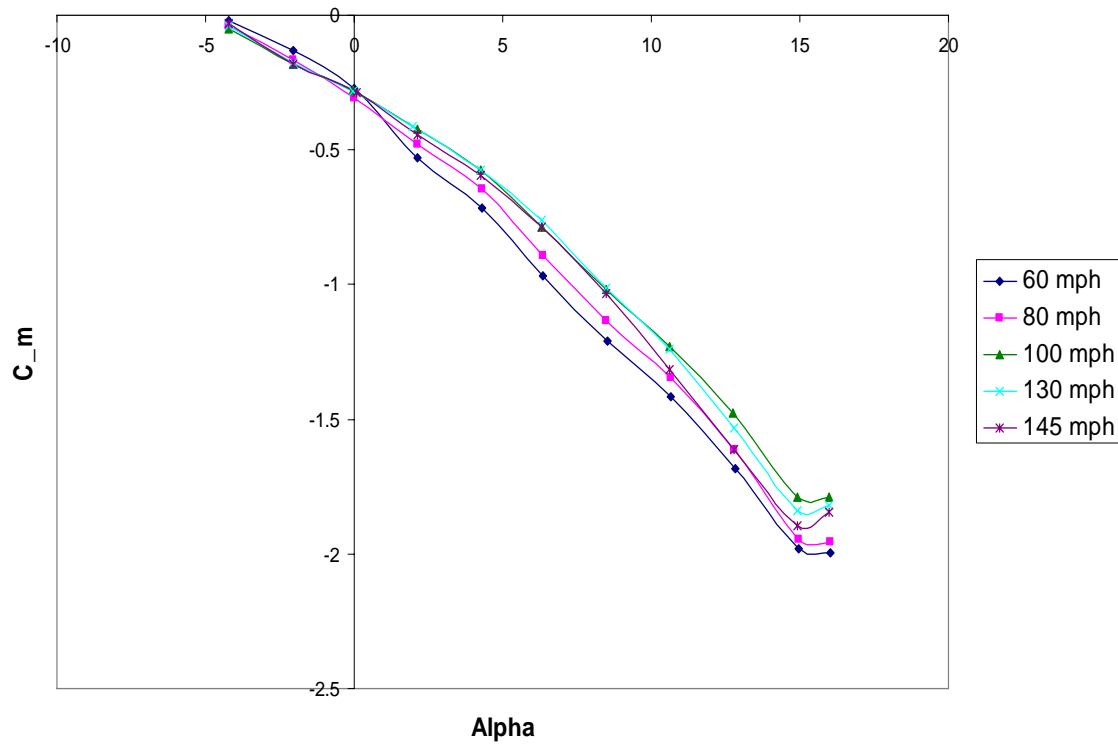
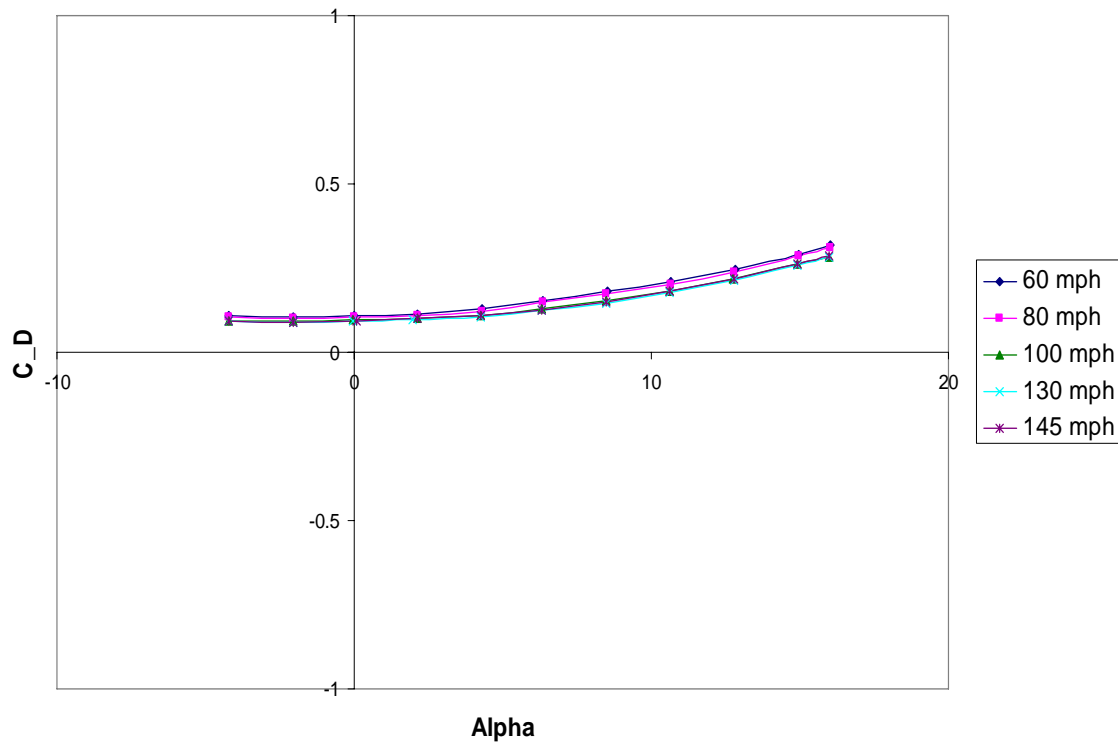


**Figure 74 Drag and pitch relations of the  $60^\circ$  joined wing, plastic. Second Run.**

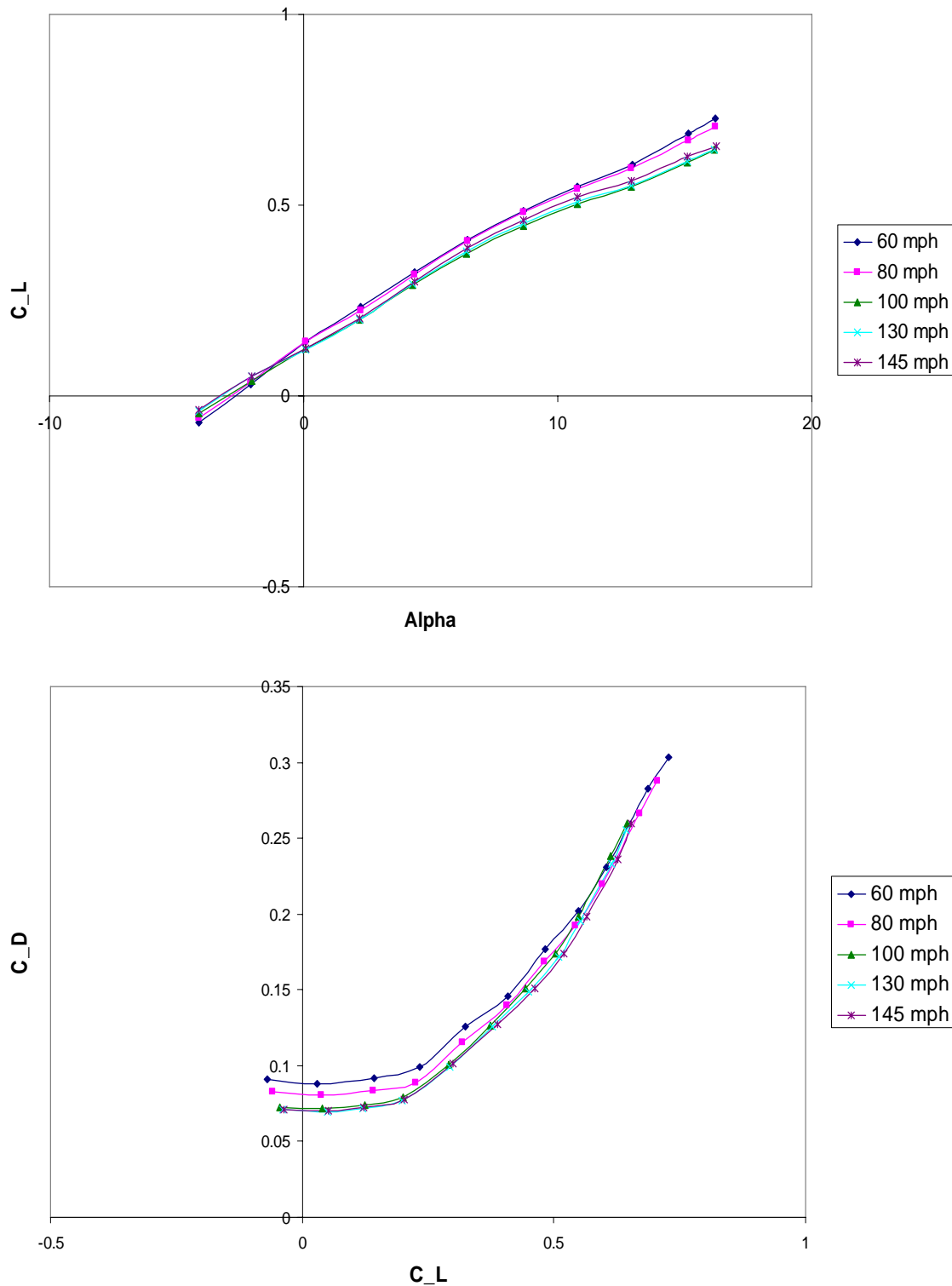


**Figure 75 Lift and drag relations of the 60° joined wing, not morphed, aluminum.**

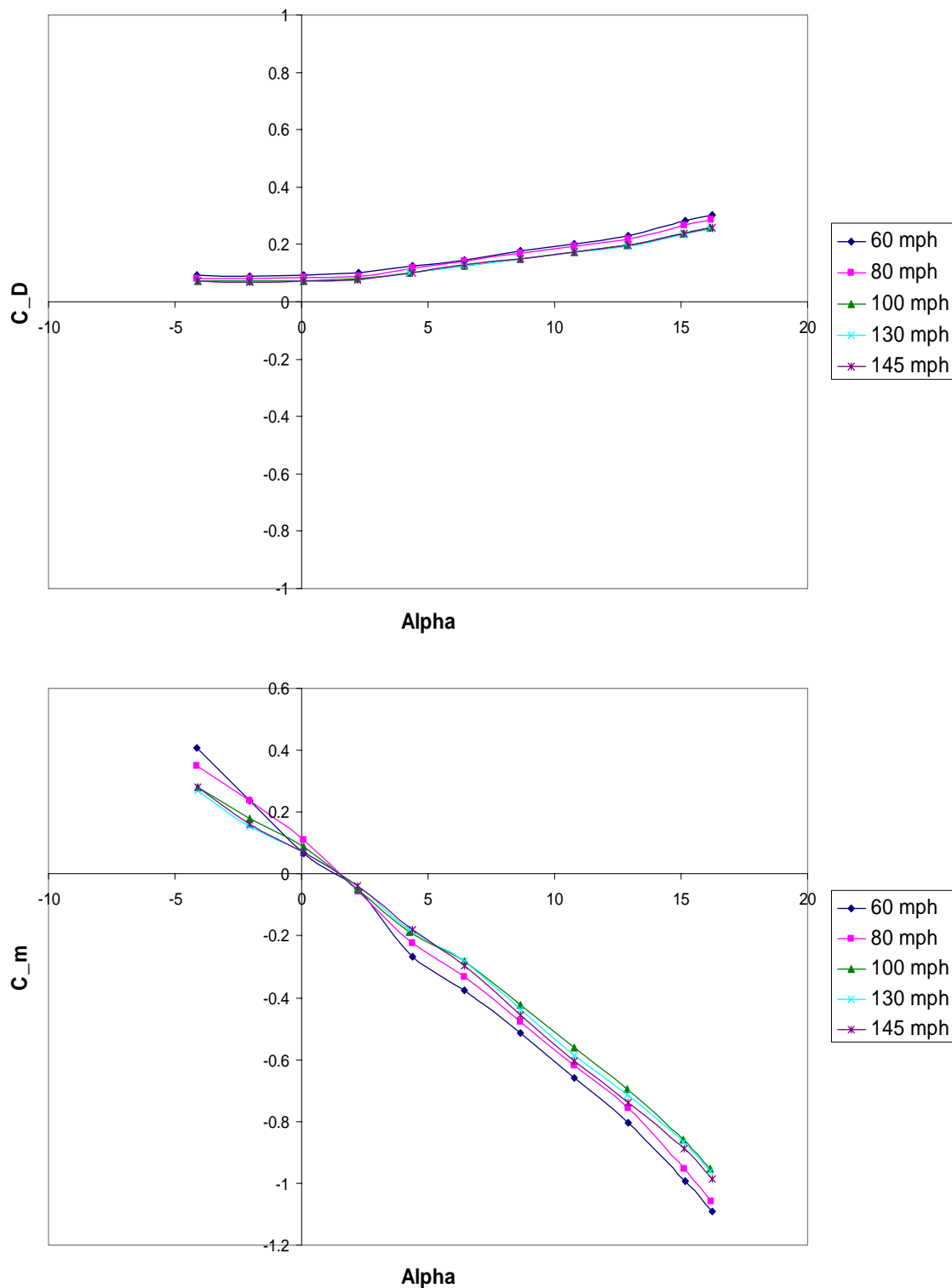


**Figure 76 Drag and pitch relations of the  $60^\circ$  joined wing, not morphed, aluminum.**

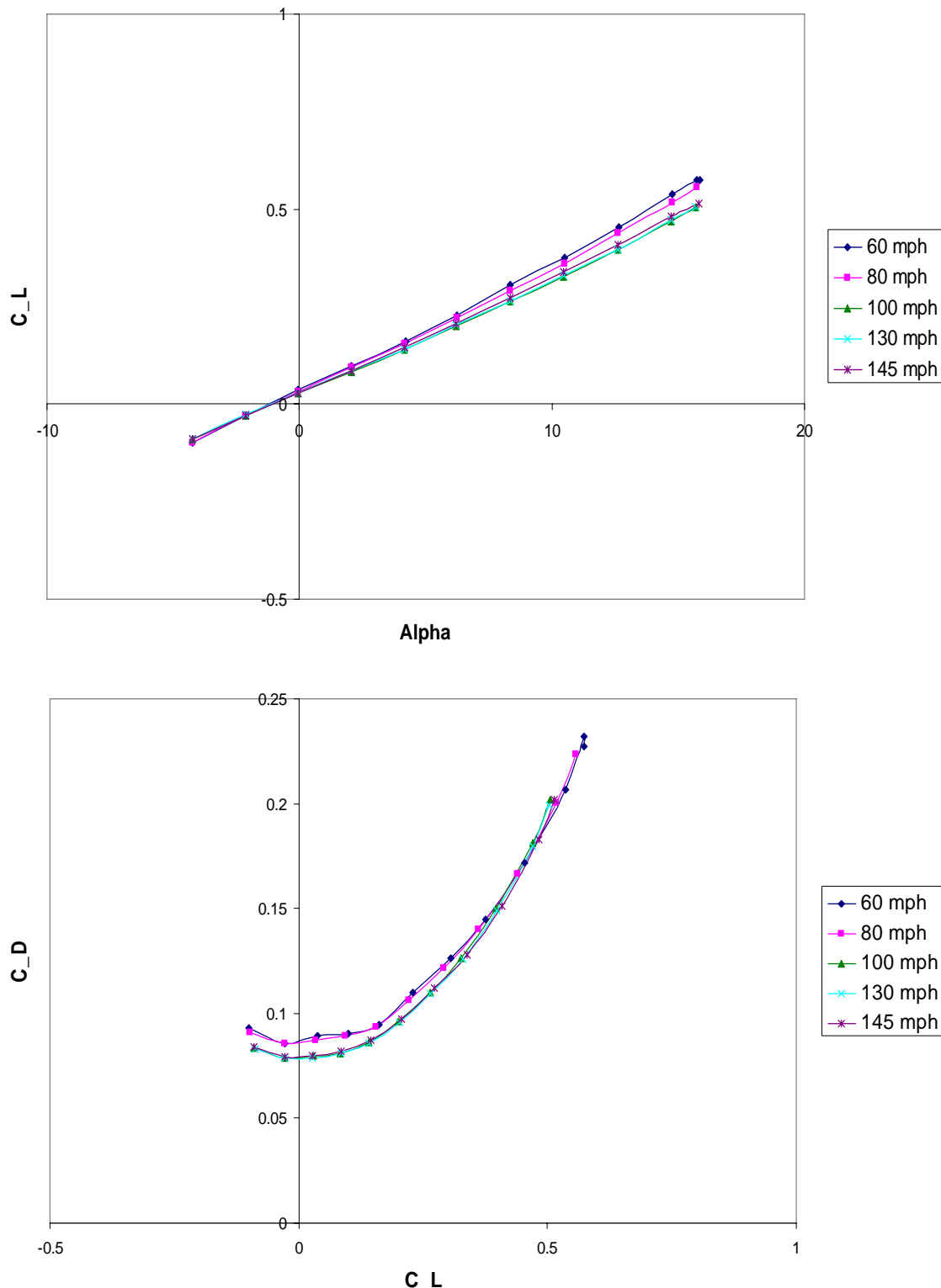


**Figure 77 Lift and drag relations of the 75° joined wing, plastic.**

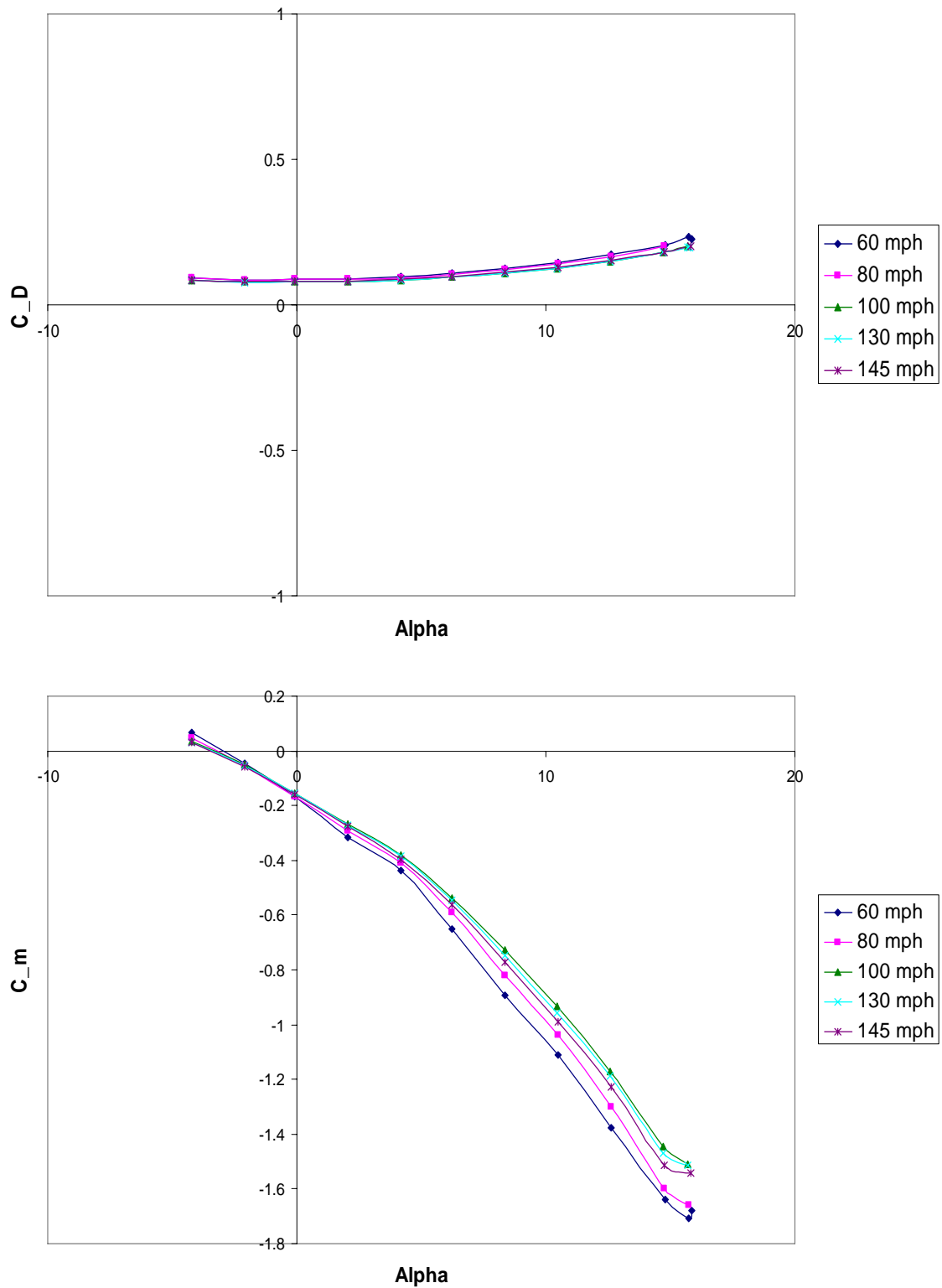


**Figure 78 Drag and pitch relations of the 75° joined wing, plastic.**

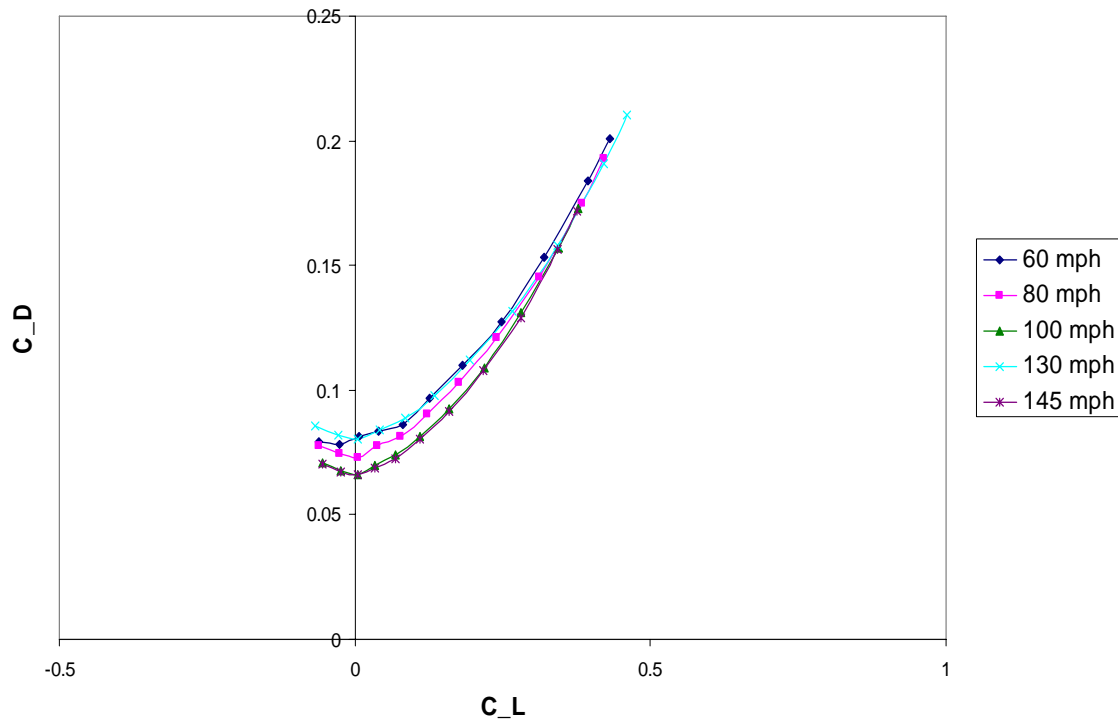
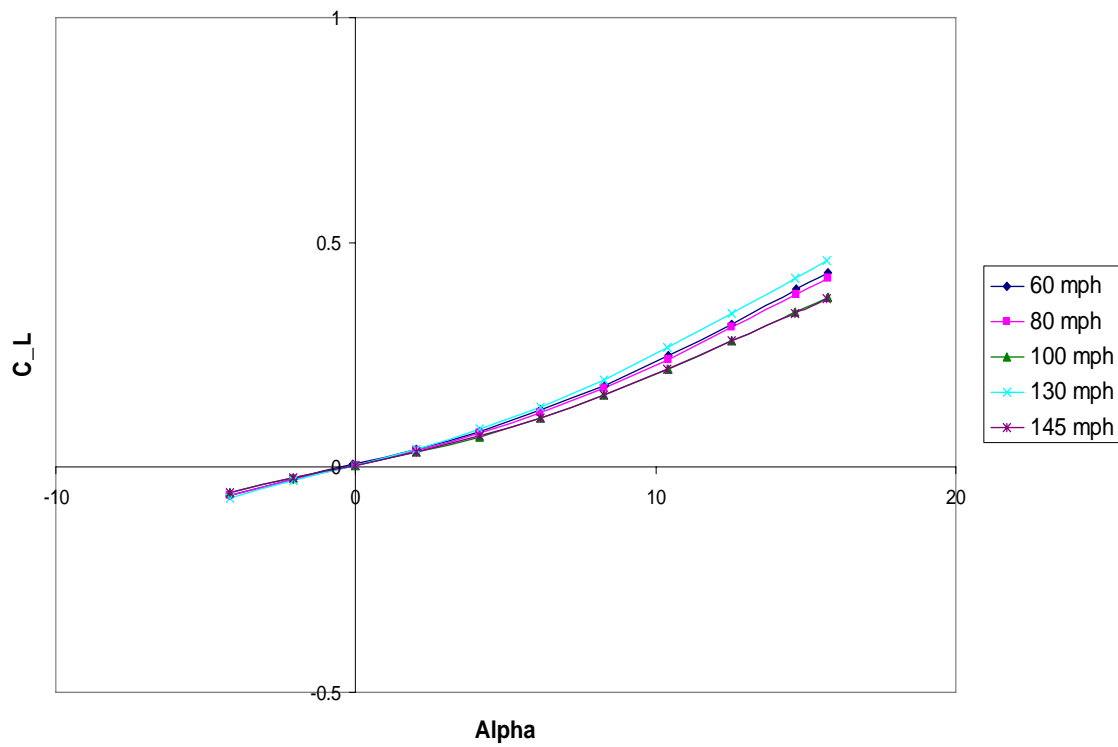


**Figure 79 Lift and drag relations of the 90° joined wing, plastic.**

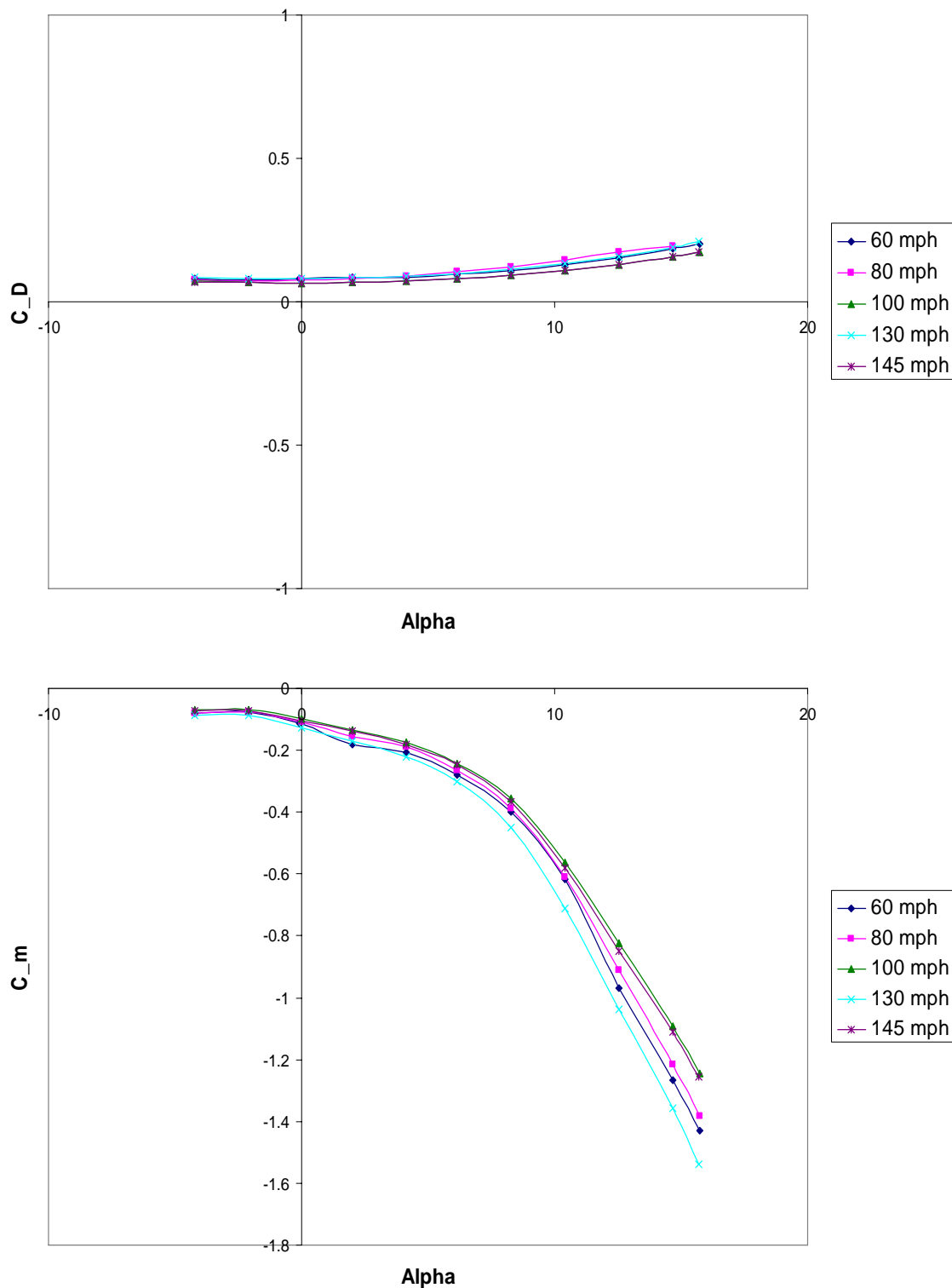


**Figure 80 Drag and pitch relations of the 90° joined wing, plastic.**

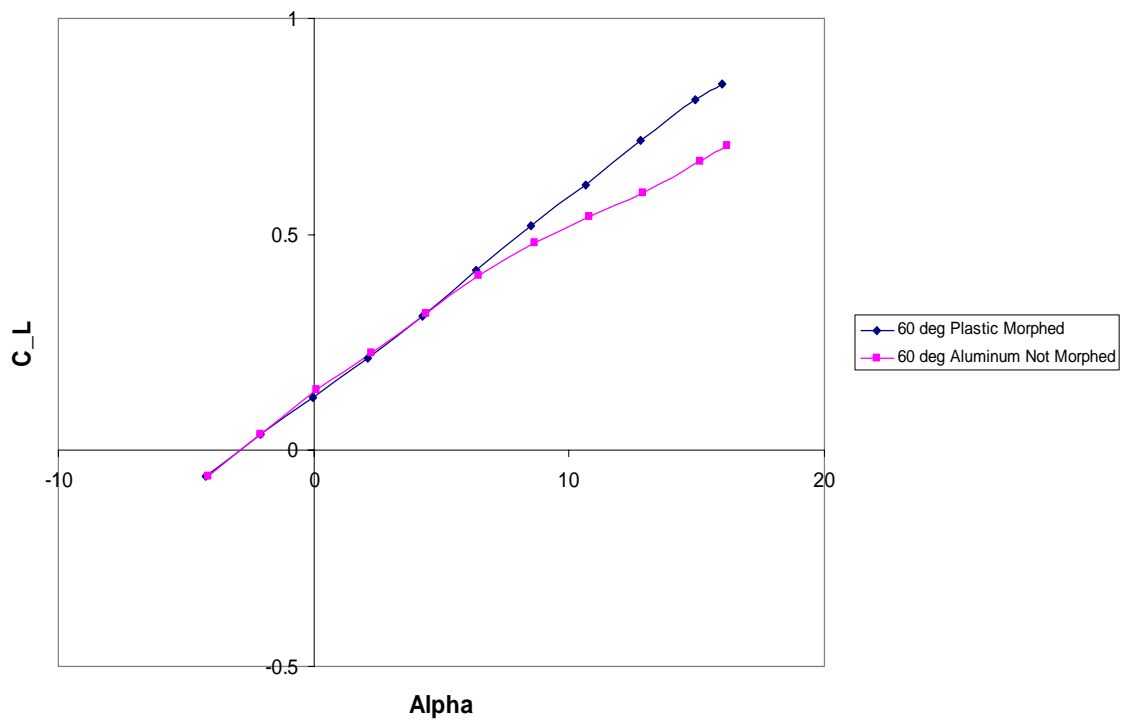


**Figure 81 Comparison of  $60^{\circ}$  joined wing between plastic morphed and the aluminum at 80 mph.**

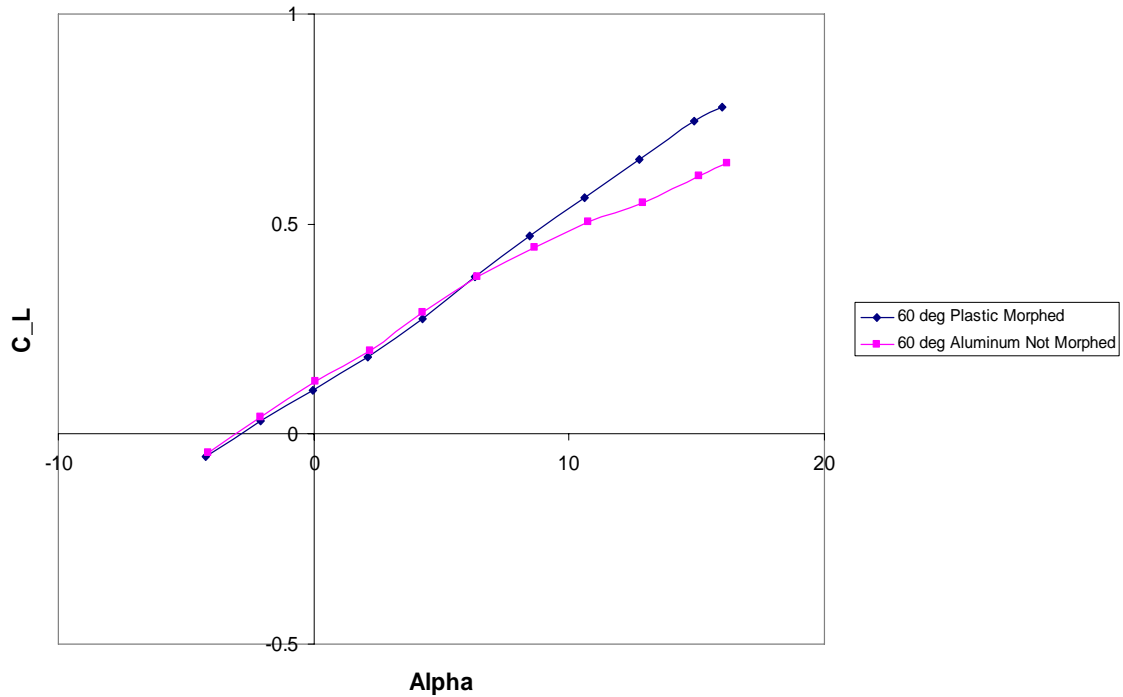


**Figure 82 Comparison of  $60^{\circ}$  joined wing between plastic morphed and the aluminum at 100 mph.**

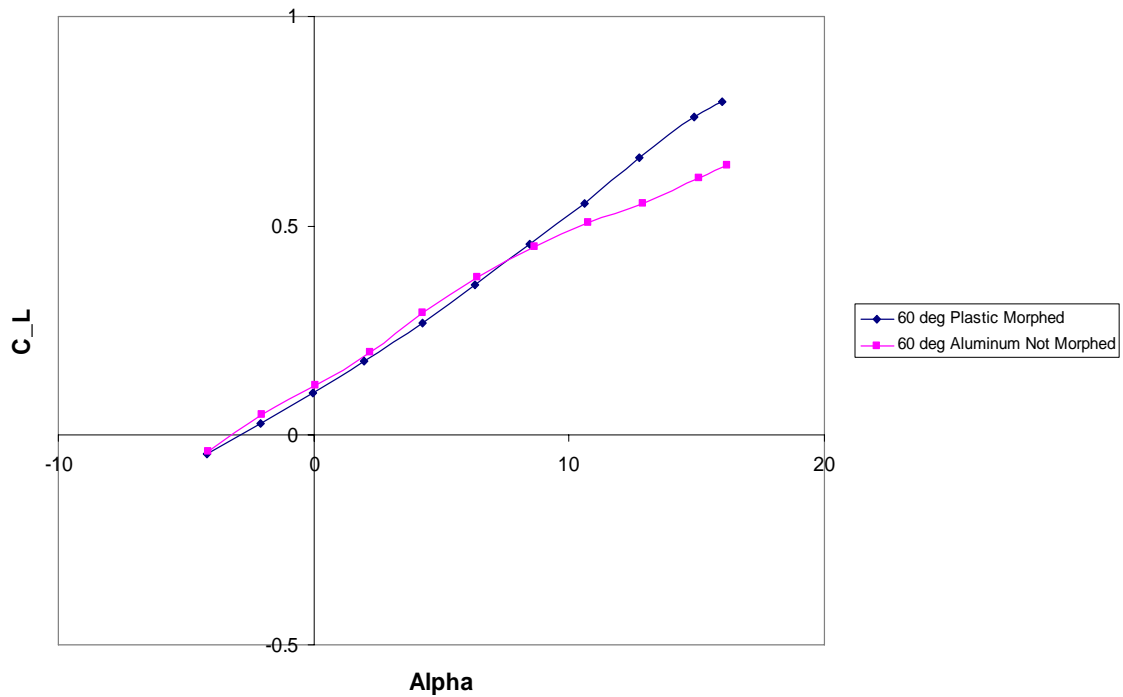


**Figure 83 Comparison of 60° joined wing between plastic morphed and the aluminum at 130 mph.**

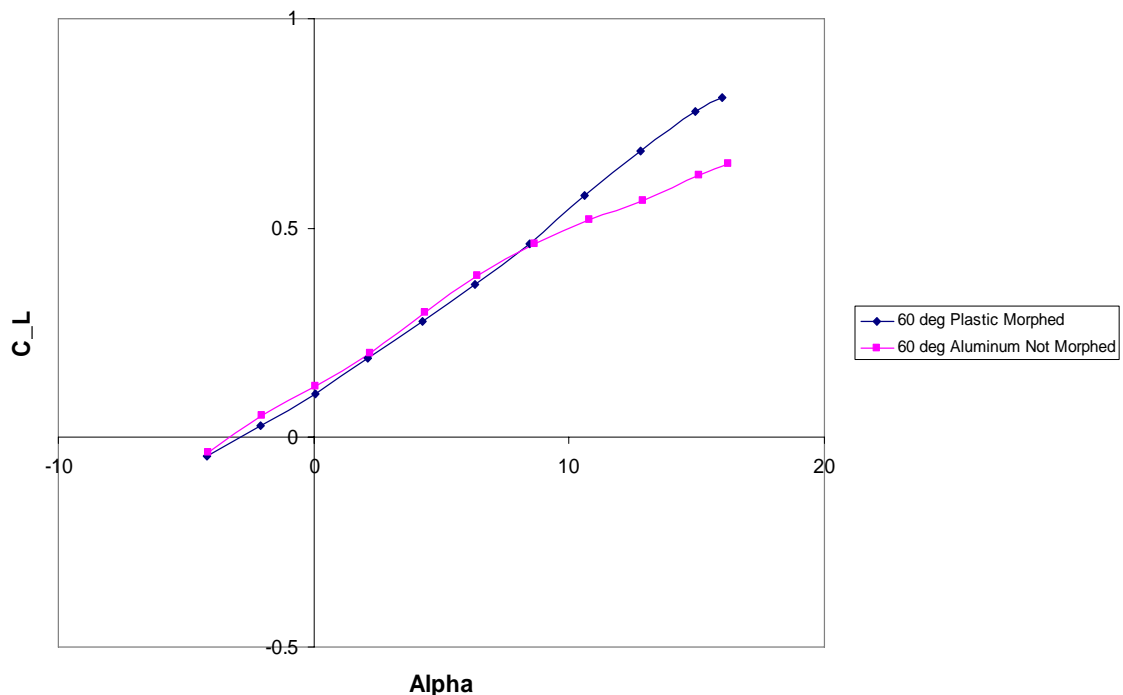


**Figure 84 Comparison of 60° joined wing between plastic morphed and the aluminum at 145 mph.**

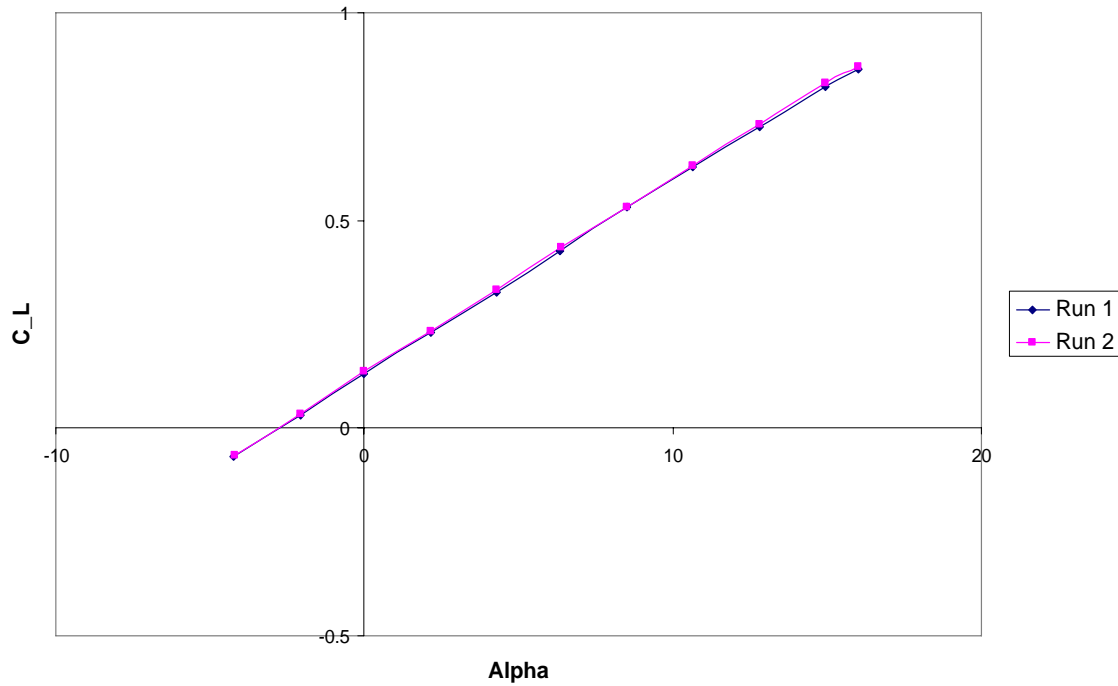


**Figure 85 Comparison between two Runs on the 60° plastic morphed wing testing for repetition at 60 mph.**

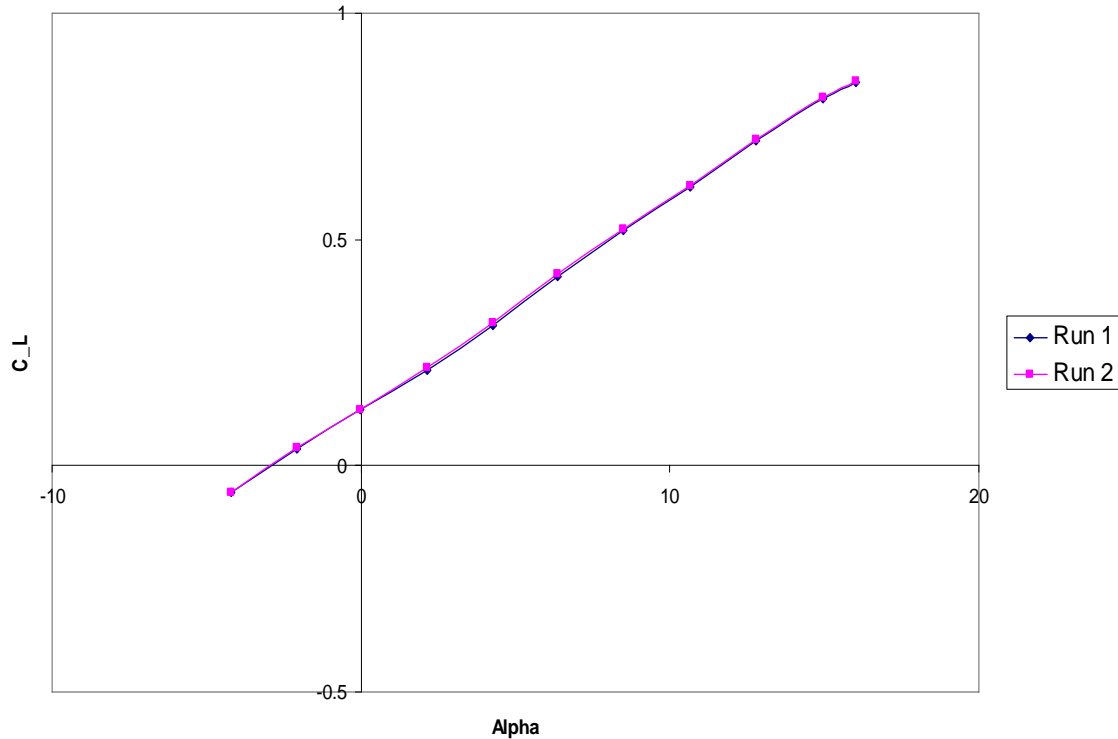


**Figure 86 Comparison between two Runs on the 60° plastic morphed wing testing for repetition at 80 mph.**

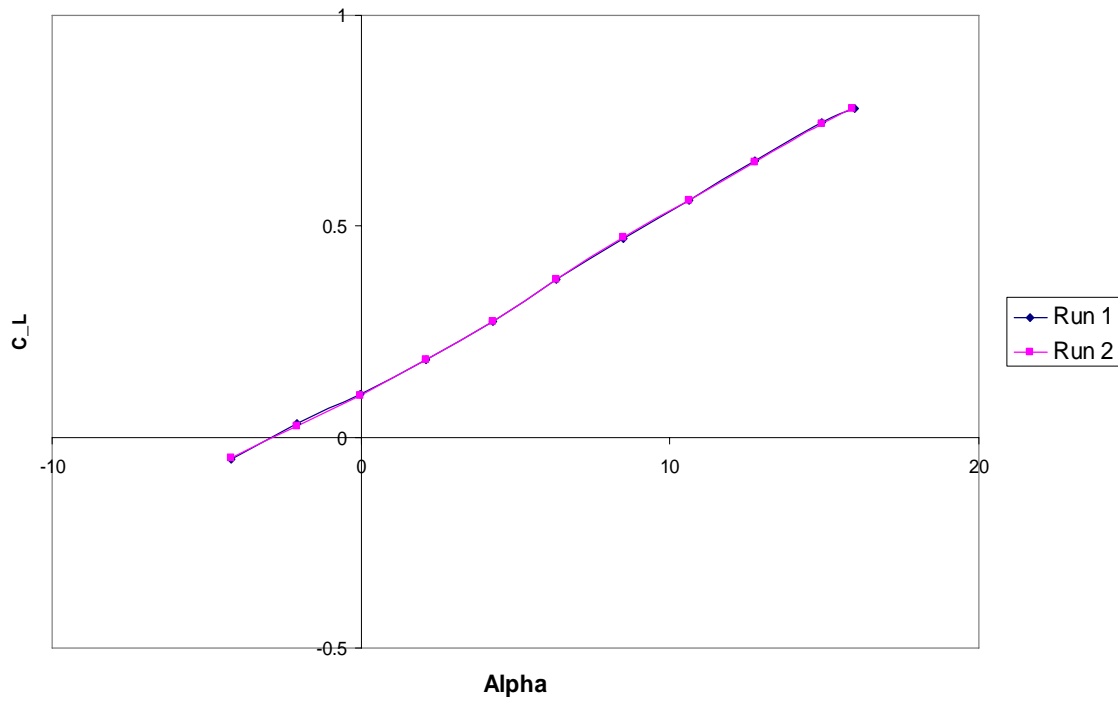


**Figure 87 Comparison between two Runs on the 60° plastic morphed wing testing for repetition at 100 mph.**

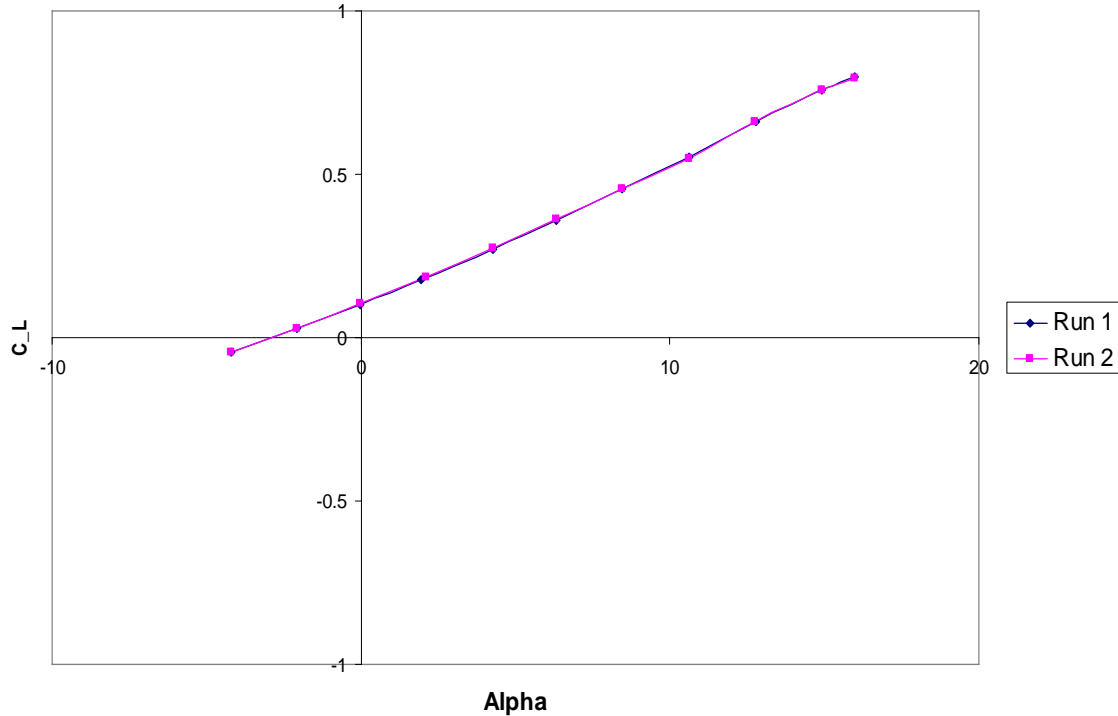


**Figure 88 Comparison between two Runs on the 60° plastic morphed wing testing for repetition at 130 mph.**

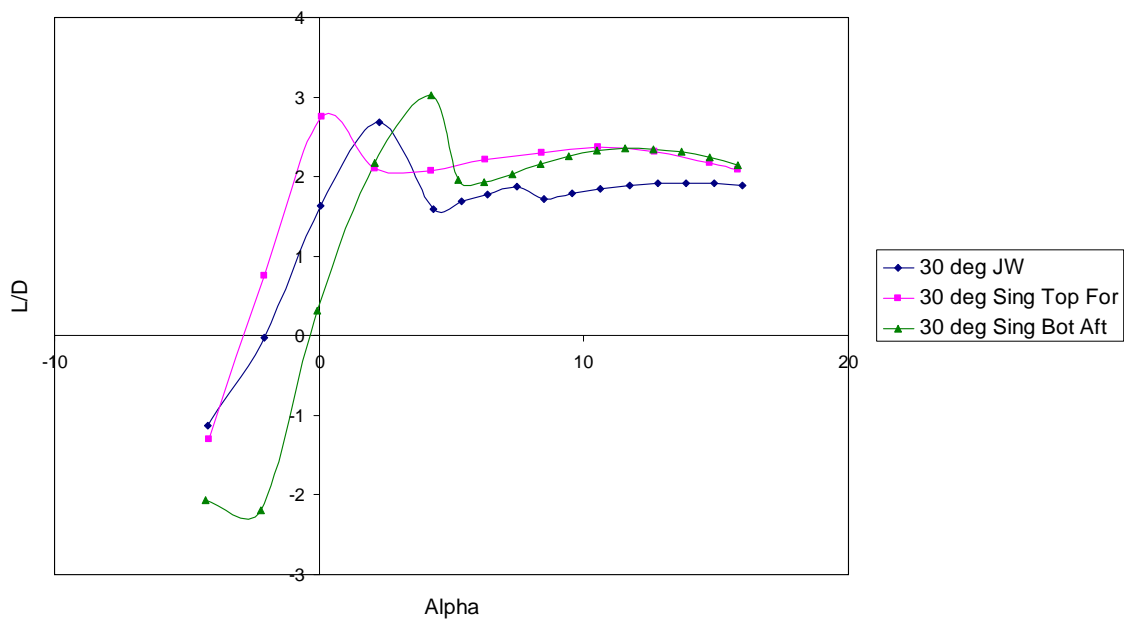


**Figure 89 Comparison of L/D vs Alpha for the 30° Joined wing and Single wings at 60 mph.**

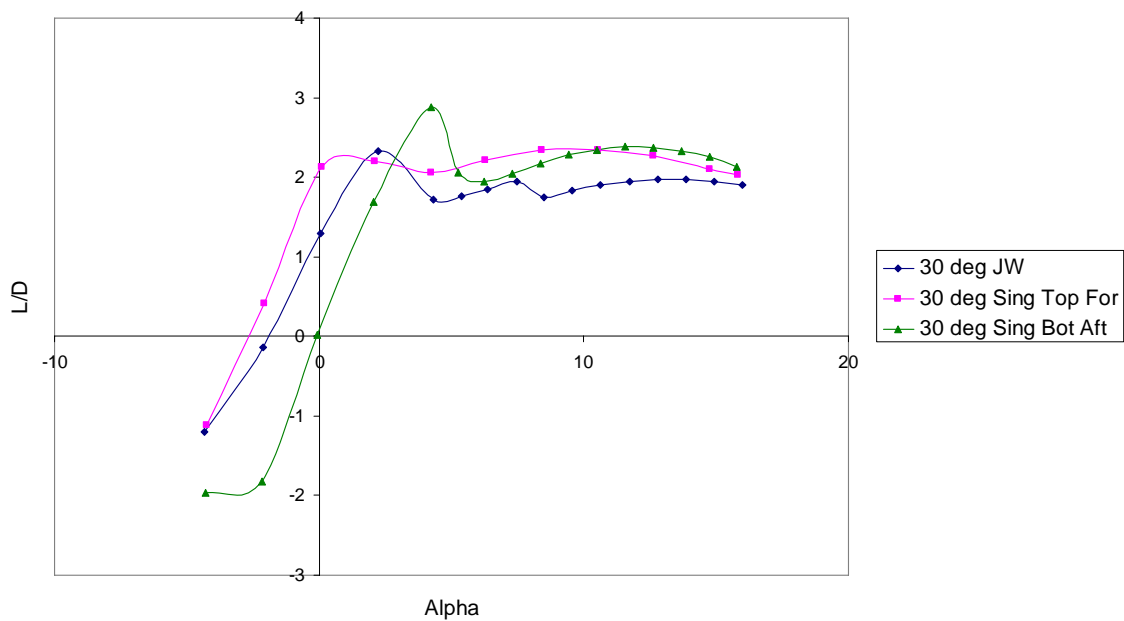


**Figure 90 Comparison of L/D vs Alpha for the 30° Joined wing and Single wings at 80 mph.**

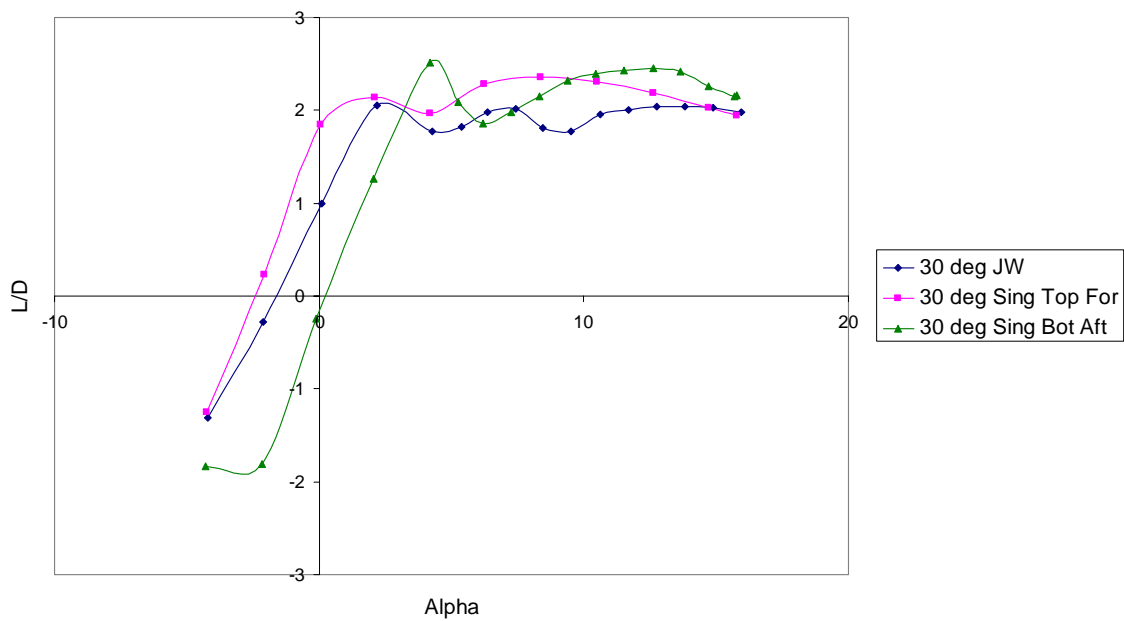


**Figure 91 Comparison of L/D vs Alpha for the 30° Joined wing and Single wings at 100 mph.**

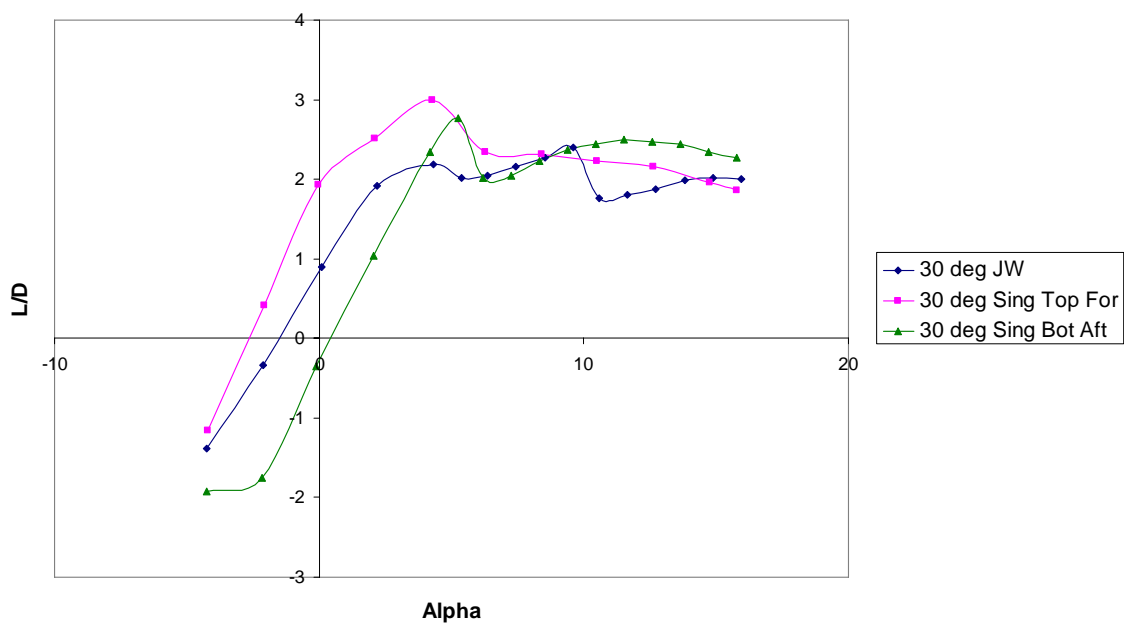


**Figure 92 Comparison of L/D vs Alpha for the 30° Joined wing and Single wings at 130 mph.**

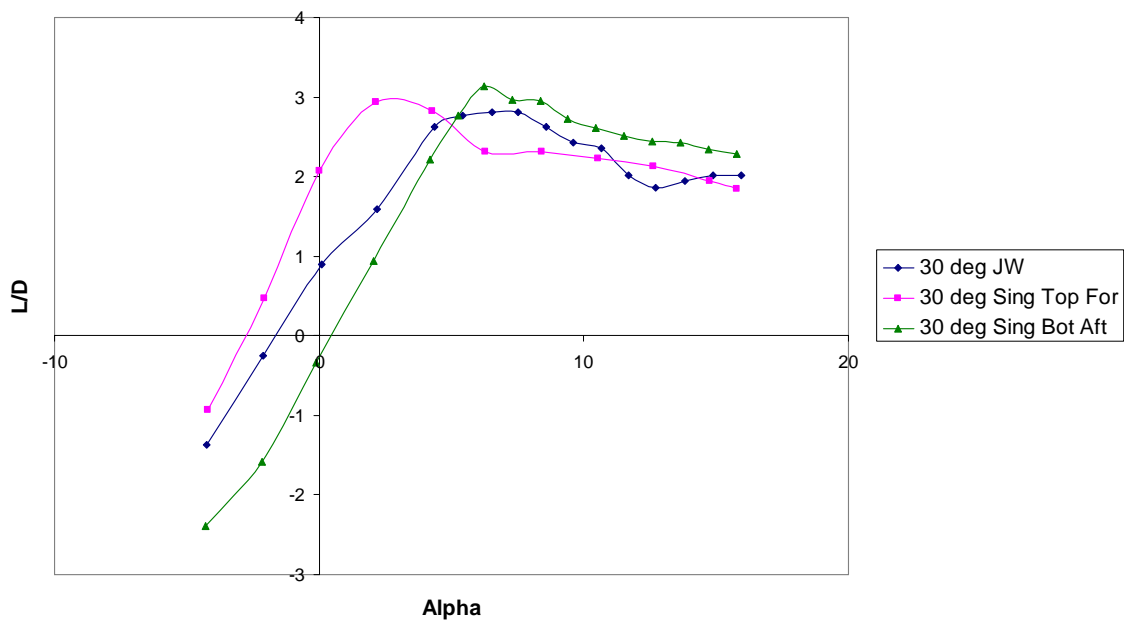


**Figure 93 Comparison of L/D vs Alpha for the 30° Joined wing and Single wings at 145 mph.**

## **Appendix B**

The following pages contain the MatLab code used to transfer measured forces and moments on the balance to wind (Earth) centered frame reference by correcting for tare effects, balance interactions, and wind tunnel irregularities, then outputting the lift, drag, roll, pitch and yaw coefficients, as well as the angle of attack.

```

%*****
%***** Lt. Dave Gebbie & Capt Anthony DeLuca *****
%***** Calculation of Lift, Drag, Moments *****
%***** AFRL Project: Strike Tanker, 11 May 2004 *****
%***** Readapted by: Ens. Christopher Dike *****
%***** for: A Wind Tunnel Investigation of Joined Wing
%***** Scissors Morphing, 04 APRIL 2006 *****
%*****
%
```

```

%This Code will transfer measured Forces and Moments on the balance to Wind
%(earth) centered frame of reference by correcting for tare effects, balance
%interactions, and wind tunnel irregularities, then plot lift and drag
%coefficients in as functions of AoA, beta, Prop speed, and elevon
%deflection angle.

```

```
clear; clc; format short g;
```

```

%*****
%***** Room Conditions and Model Specifics : *****
%***** UNITS are in Ft, Sec, lbm, Psf, Rankine, fps *****

```

Mass = 7.56;	% lbm (Missile)
Gas_Const = 1716;	% ft-lbf/Slug-R
T_room = 76 + 459.67;	% deg R ****Changed for each day of testing****
P_barro = 28.82 * 0.4911541;	% Psi ****Changed for each day of testing****
Density = (P_barro * 144)/(1716 * T_room);	% lbm/ft^3 or lbf-s^2/ft^4
Wing_Area = 0.265; Dike, 23Feb06)	% ft^2 Wing Area, (Christopher Dike, 23Feb06)
Span = 15.588; S_f= Span*1;	% in, (Christopher Dike, 23Feb06) % in^2, Front wing Area,
S_r= Span*1;	Base*Height(Christopher Dike, 23Feb06) % in^2, Rear wing Area, Base*Height (Christopher Dike, 23Feb06)
Root_Chord = 1; AR_f= Span^2/S_f;	% in (S.T.) % Front wing Aspect Ratio (Christopher Dike, 23Feb06)
AR_r= Span^2/S_r;	% Rear wing Aspect Ratio (Christopher Dike, 23Feb06)
Aspect_Ratio = (AR_f*(S_f/S_r)+AR_r*(S_r/S_f))/((S_f/S_r+1)*(S_r/S_f+1));	% From Bagwell and Selberg (Christopher Dike, 23Feb06)
Kinematic_Viscosity = .372e-6;	% slug/ft-s

```

Speed_of_Sound = sqrt(1.4 * T_room * Gas_Const); % fps

%Distances between sensors (inches) to calculate moments

D1 = (2.10 / 2); D2 = D1; D3 = (1.7 / 2); D4 = D3; %inches

%Offset distances from the Mounting Block to the Model C.G. (inches)

Y_cg = 0.0; % changed April 5 2006 >> Joined
X_cg = 1.5625; Wing Missile
Z_cg = 0.0; % inches (from origin @ balance center w/ + right)
              % inches (from origin @ balance center w/ + down)

% *****
% ***** Tunnel Correction Data *****
% *****
****

K_1 = 1.08; % From fig. 10.2 assuming 4 digit airfoil
K_3 = 0.89; % b/B, where B is 41 inches, the width of the
tunnel
delta = 0.38;
Tau_1 = 0.83;
X_Section = (32/12)*(41/12) ; % ft^2
Wing_Volume = Wing_Area * (.2/12) ; % ft^3
Body_Volume = (357.4./(12^3)); % ft^3
Epsilon_tunnel_correction=0.954742458; % Correction factor for velocity
                                         differences between Hot-wire and transducer 28 Feb 06
% For 100 > 0.955282636 , For 130 > 0.960305087 , For 145 > 0.954742458

%**** Solid body blockage corrections due to wing and fuselage ***
Epsilon_sb_w = (K_1*Tau_1*Wing_Volume) / X_Section^(3/2);
Epsilon_sb_b = (K_3*Tau_1*Body_Volume) / X_Section^(3/2);
Epsilon_tot = Epsilon_sb_w + Epsilon_sb_b+(Epsilon_tunnel_correction-1);

% *****
% ***** Tunnel Correction Data *****
% *****

%Balance Interactions with off axis elements for the 100 lb balance
%Using average of the 8 lb calibration runs for N1 & N2 and the
%6 lb calibration for S1, S2 & A then normalizing by the actual
%sensor (N1, N2,...) in question. The sensor sequence in each row vector is:

```

```

%
% [N1 N2 S1 S2 A L]N1_I = ([7.806 -.701 .447 .060 -.142 .043] + [7.803 -.702 .442 .057
-.140 .041])/2;
%   N11 = N1_I(1,1)/100;
%
% N2_I = (.183 -7.486 -.05 -.052 .047 0] + [.182 -7.485 -.053 -.056 .044 0])/2;
%   N22 = N2_I(1,2)/-100;
%
% S1_I = (.039 0 7.917 -.408 -.024 -.025] + [.036 0 7.915 -.410 -.026 -.022])/2;
%   S11 = S1_I(1,3)/50;
%
% S2_I = ([0 .013 -.124 8.16 -.067 -.017] + [0 .012 -.122 8.158 -.065 -.015])/2;
%   S22 = S2_I(1,4)/50;
%
% A_I = (.012 .008 -.025 .041 6.981 0.09] + [.012 .007 -.025 .033 7.003 .081])/2;
%   A11 = A_I(1,5)/50;
%
% L_I = ([-.082 -.061 -.023 .096 .262 8.607] + [-.09 -.072 -.009 .104 .276 8.604])/2;
%   L11 = L_I(1,6)/40;
% *****
% *****Updated Calibration for the 8 component 25 lb, Ignoring A1 & L1 because of the
similarity to A2 & L2
% and using an average of 10 lb calibration runs for N1, N2, S1, S2 & A2 and 7 lb for
L2 then
%dividing by its actual measurement to have a matrix of fractions with the diagonal of 1.

N1_I = ([1 -.010272 .01244 -.000593 .13758 .014914]); %+ [7.803 -.702 .442 .057 -.140
.041])/2; HERE NUMBERS ARE lb/lb
    N11 = N1_I(1,1);%/100;

N2_I = ([-.023 1 .00079 -.000296 .019354 .14516]); %+ [.182 -7.485 -.053 -.056 .044
0])/2;
    N22 = N2_I(1,2);%/-100;

S1_I = (.002864 .00593 1 .002963 .089481 .000099); %+ [.036 0 7.915 -.410 -.026 -
.022])/2;
    S11 = S1_I(1,3);%/50;

S2_I = ([-.001576 .003939 -.026194 1 .028065 .007287]); %+ [0 .012 -.122 8.158 -.065 -
.015])/2;
    S22 = S2_I(1,4);%/50;

A_I = (.209628 -.21866 .008038 -.007135 1 -.002077); %+ [.012 .007 -.025 .033 7.003
.081])/2;
    A11 = A_I(1,5);%/50;

```

```

L_I = ([-.253931 -.239861 -.007284 .019533 .025824 1]); %+ [-.09 -.072 -.009 .104 .276
8.604])/2;
L11 = L_I(1,6);%/40;

N1_normalized = (N1_I) .* [N11 N22 S11 S22 A11 L11].^(-1); %/100
DROPPED FOR 25LB BALANCE
N2_normalized = (N2_I) .* [N11 N22 S11 S22 A11 L11].^(-1); %/100
S1_normalized = (S1_I) .* [N11 N22 S11 S22 A11 L11].^(-1); %/50
S2_normalized = (S2_I) .* [N11 N22 S11 S22 A11 L11].^(-1); %/50
A_normalized = (A_I) .* [N11 N22 S11 S22 A11 L11].^(-1); %/50
L_normalized = (L_I) .* [N11 N22 S11 S22 A11 L11].^(-1); %/40

Interactions_Kij = [N1_normalized' N2_normalized' S1_normalized' S2_normalized'
A_normalized' L_normalized'];

```

%Load the static tare data for the alpha sweep w/o the wind , separate each  
%force from the file, and fit a 4th order poly as an x-y plot (AoA vs.  
%Force) for each of the 6 force sensors.

```

%*****Code inserted May 11, 2004*****
load Dike_Tare_30jwPl.txt; % Raw data file to be read in.
FILE=Dike_Tare_30jwPl(:,__);

j=1;
k=1;
L=length(FILE);

for i=1:L %Run for all data points # of rows
    if i~=L %if current row is not last row, go to next
        NEXT=i+1; %set next equal to the value of the next row
        VALUE2=FILE(NEXT,1); %set value2 as next row column 1
    else if i==L %unless the it is the last value
        VALUE2=50; %value2 set to 50 to end the sequence
    end
    end
    A(j,:)=FILE(i,:); %set row j of A equal to row i of FILE
    VALUE1=FILE(i,1); %set value1 equal to row i column 1 of FILE
    if VALUE1==VALUE2 %if value1 equals value2, go to next row
        j=j+1;
    else if VALUE1~=VALUE2 %if value1 and value2 are different check
        if length(A(:,1))<5 %if less than 20 values, ignored due to angle change
            j=1;
            clear A;
        else if length(A(:,1))>5 %if more than 20 values

```

```

C=length(A(:,1)); %find length of A
for m=1:9 %Average all rows of the like values in A
    B(k,m)=mean(A(4:C,m)); %disregarding first 10 for vibrations
end
j=1;
k=k+1;
clear A
end
end
end

if B(k-1,1)<B((k-2),1)
    B=B(1:(k-2),:)
end

tare=[B]
%*****End of Inserted
Code*****  

[row,col] = size(tare);

for k = 1:row

theta_tare(k,:,:)=tare(k,1).* (pi/180);
N1_tare(k,:,:)=tare(k,4);
N2_tare(k,:,:)=tare(k,5);
S1_tare(k,:,:)=tare(k,7);
S2_tare(k,:,:)=tare(k,8);
A_tare(k,:,:)=tare(k,6); %changed 13Jan05 misnamed column
L_tare(k,:,:)=tare(k,9);

end

N1_poly = polyfit(theta_tare,N1_tare,4);
N2_poly = polyfit(theta_tare,N2_tare,4);
S1_poly = polyfit(theta_tare,S1_tare,4);
S2_poly = polyfit(theta_tare,S2_tare,4);
A_poly = polyfit(theta_tare,A_tare,4) ;
L_poly = polyfit(theta_tare,L_tare,4) ;

clear ('B','C','D','L')
%Load the specific test run files, subtract the effect of the static
%weight with the tare polynomials above, and correct for cross diagonal

```

%sensor interactions.

```
%*****Code inserted May 11,  
2004*****  
%modified January 11, 2005  
load Dike_145_30jwPl.txt; % Raw data file to be read in:  
FILE=Dike_145_30jwPl(:, :);  
  
j=1;  
k=1;  
L=length(FILE);  
  
for i=1:L %Run for all data points # of rows  
    if i~=L %if current row is not last row, go to next  
        NEXT=i+1; %set next equal to the value of the next row  
        VALUE2=FILE(NEXT,1); %set value2 as next row column 1  
    else if i==L %unless the it is the last value  
        VALUE2=50; %value2 set to 50 to end the sequence  
    end  
    end  
    A(j,:)=FILE(i,:); %set row j of A equal to row i of FILE  
    VALUE1=FILE(i,1); %set value1 equal to row i column 1 of FILE  
    if VALUE1==VALUE2 %if value1 equals value2, go to next row  
        j=j+1;  
    else if VALUE1~=VALUE2 %if value1 and value2 are different check  
        if length(A(:,1))<5 %if less than 20 values, ignored due to angle change  
            j=1;  
            clear A;  
        else if length(A(:,1))>5 %if more than 20 values  
            C=length(A(:,1)); %find length of A  
            for m=1:9 %Average all rows of the like values in A  
                B(k,m)=mean(A(4:C,m)); %disregarding first 10 for vibrations  
            end  
            j=1;  
            k=k+1;  
            clear A  
        end  
    end  
end  
end  
end  
  
if B(k-1,1)<B((k-2),1)  
    B=B(1:(k-2),:)  
end
```

```

sample_data=[B]

%*****End of Inserted
Code*****


[row2,col2] = size(sample_data);

for i = 1:row2

%Angles of the model during test runs (Roll, Pitch {AoA}, Yaw {Beta}):

phi      = 0;
theta(i,:) = sample_data(i,1) .* (pi/180);           %radians
si(i,:)   = sample_data(i,2) .* (pi/180);           %radians
Wind_Speed(i,:) = sample_data(i,3) .* (5280/3600);    %fps
%pressure(i,:) = sample_data(i,(12:19)) - tare(i,12:19);

%Flight Parameters (Re#, Ma#, Dynamic Pressure):

q = (.5 * Density) .* Wind_Speed.^2;                  %lbf/ft^2
q_Corrected = q .* (1 + Epsilon_tot)^2;                %lbf/ft^2
Wind_Speed_Corrected = Wind_Speed .* (1 + Epsilon_tot); %fps
Mach_Number = Wind_Speed_Corrected ./ Speed_of_Sound;
%NonDimensional
Reynolds_Number = ((Density * Root_Chord) .* Wind_Speed_Corrected) ./ 
Kinematic_Viscosity; %NonDimensional
Flight_Parameters = [Mach_Number Reynolds_Number q_Corrected];

%individual forces for each sensor:

N1_test(i,:,:)=sample_data(i,4);
N2_test(i,:,:)=sample_data(i,5);
S1_test(i,:,:)=sample_data(i,7);
S2_test(i,:,:)=sample_data(i,8);
A_test(i,:,:)=sample_data(i,6); %changed 13Jan05 misnamed column
L_test(i,:,:)=sample_data(i,9);

%Evaluating the actual test theta angle (AoA) in the tare polynominal to
%determine the tare values for the angles tested in each run.

N1_eval = polyval(N1_poly,theta);
N2_eval = polyval(N2_poly,theta);
S1_eval = polyval(S1_poly,theta);
S2_eval = polyval(S2_poly,theta);
A_eval = polyval(A_poly,theta);

```

```

L_eval = polyval(L_poly,theta);

%The Time-Averaged (raw) forces N1, N2, S1, S2, A, L measurd in the wind
%tunnel (body axis) with the tare effect of the weight subtracted off.

N1_resolved = N1_test - (N1_eval);
N2_resolved = N2_test - (N2_eval);
S1_resolved = S1_test - (S1_eval);
S2_resolved = S2_test - (S2_eval);
A_resolved = A_test - (A_eval);
L_resolved = L_test - (L_eval);

Forces_minus_tare = [N1_resolved N2_resolved S1_resolved S2_resolved A_resolved
L_resolved]';

%Forces N1, N2, S1, S2, A, & L corrected for the balance interactions (body axis)

Corrected_Data = (inv(Interactions_Kij) * Forces_minus_tare);

%Calculation of the Axial, Side, & Normal Forces from the corrected balance
%forces in the Body Axis reference frame

Forces_b(:,i) = [Corrected_Data(5,i); Corrected_Data(3,i) + Corrected_Data(4,i);
Corrected_Data(1,i) + Corrected_Data(2,i)];

%Calculation of the Drag, Side, & Lift Forces in the Wind Axis reference
%frame

Forces_w =
[Forces_b(1,:).*cos(theta').*cos(si')+Forces_b(2,:).*sin(si')+Forces_b(3,:).*sin(theta').*co
s(si');
-Forces_b(1,:).*sin(si').*cos(theta')+Forces_b(2,:).*cos(si')-
Forces_b(3,:).*sin(theta').*sin(si');
-Forces_b(1,:).*sin(theta')+Forces_b(3,:).*cos(theta')];

%First entry is the moments calculated by the balance or direct calculation
%in the Body Reference Frame. Balance measures Roll (l), Yaw is about the
%z-axis (n), and Pitch is about the y-axis (m). Distances from strain
%gages to C.G. are in INCHES. Moments are in-lbf

m = Corrected_Data(1,i) * D1 - Corrected_Data(2,i) * D2;
n = Corrected_Data(3,i) * D3 - Corrected_Data(4,i) * D4;
Moments_b(:,i) = [Corrected_Data(6,i); m; n];

%Second entry is the conversion from the "Balance Centeric" moments to the
%Wind Reference monments with respect to the Balance Center (bc)

```

```

Moments_w_bc = [Moments_b(1,:).*cos(theta').*cos(si')-
Moments_b(2,:).*sin(si')+Moments_b(3,:).*sin(theta').*cos(si');

Moments_b(1,:).*sin(si').*cos(theta')+Moments_b(2,:).*cos(si')+Moments_b(3,:).*sin(the
ta').*sin(si');
-Moments_b(1,:).*sin(theta')+Moments_b(3,:).*cos(theta')];

%Finally, the balance centered moments are converted to moments about the
%Model's Center of Mass (cm) or Center of Gravity (CG)

cgdist=sqrt((X_cg)^2+(Z_cg)^2); %Obtaining the direct distance between the
%center of the balance and the center of mass
w=atan(-Z_cg/X_cg); %Obtaining the angle between cgdist and the x axes at
zero angle of attack

X_cm(i,:)= cos(theta(i,:)+w)*cos(si(i,:))*(cgdist);
Y_cm(i,:)= Y_cg + X_cm(i,:)*tan(si(i,:)); % appropriate for very small y_cmb
and reasonable si
Z_cm(i,:)= -sin(theta(i,:)+w)*(cgdist);

Moments_w_cg_u =
[Moments_w_bc(1,:) + Z_cm(i,:)*Forces_w(2,:) + Forces_w(3,:)* Y_cm(i,:);
Moments_w_bc(2,:) - X_cm(i,:)*Forces_w(3,:) + Forces_w(1,:)* Z_cm(i,:);
Moments_w_bc(3,:) - Y_cm(i,:)*Forces_w(1,:) - Forces_w(2,:)* X_cm(i,:)];

%Calculation of the actual Lift and Drag non-dimensional Coefficients, uncorrected for
tunnel effects, (Cl and Cd)

C_L_u = Forces_w(3,:)./(q_Corrected'.* Wing_Area); %Keuthe & Chow pg 178
C_D_u = Forces_w(1,:)./(q_Corrected'.* Wing_Area);
Coefficients = [C_L_u; C_D_u];
% Ave_Cl = mean(Coefficients(:,1));
% Ave_Cd = mean(Coefficients(:,2));

end

% *****
% ***** Tunnel Correction Data *****
% *****
***** Drag Coefficient Correction *****
C_D_o = min(Coefficients(:,2));
C_L_u_sqrd = Coefficients(:,1).^2;

```

```

Delta_C_D_w = ((delta * Wing_Area) / X_Section) .* C_L_u_sqrd;
C_D_Corrected = C_D_u' + Delta_C_D_w;

%***** Angle of Attack due to upwash Correction *****

alpha = sample_data(:,1);
Delta_alpha_w = ((delta * Wing_Area) / X_Section) .* (57.3 * C_L_u);
alpha_Corrected = alpha + Delta_alpha_w';

%***** Pitching Moment Correction *****

tau2 = .6;                                % Blockage of horizontal tail from Fig 10.40 of
                                             Wind Tunnel book
l_t = 12.26/12;                            % ft = length from tail MAC to aircraft CG
Span_t = 5/ 12 ;                           % ft = Projected horizontal span of V-tail
Tail_Area = 4.375/ 144;                     % ft^2 = Projected horizontal tail area
c_bar = 1 / 12;                            % 1.6875 13 Sept 04 Changed May 11, 2004 ft
                                           = Mean Chord of wing ***
                                           %Changed again April 4, 2006
V_bar = (Tail_Area * l_t) / (Wing_Area * c_bar);    % Horizontal tail volume ratio
eta_t = 1.0;
epsilon_o = 0;
i_t = 0;                                     % radians
i_w = 0;
Aspect_Ratio_t = Span_t^2 / Tail_Area;

D_epsilon_D_alpha = ((2 .* C_L_u) ./ (pi* Aspect_Ratio))';
epsilon = epsilon_o + (D_epsilon_D_alpha .* alpha_Corrected );
alpha_t = alpha_Corrected - i_w - epsilon + i_t;
C_L_alpha_t = ((0.1* Aspect_Ratio_t) / (Aspect_Ratio_t +2)) * 0.8;
D_Cm_cg_t_D_alpha_t = -C_L_alpha_t* V_bar * eta_t;
Delta_C_m_cg_t = ((D_Cm_cg_t_D_alpha_t) * (delta*tau2) * (Wing_Area / X_Section)
.* (C_L_u * 57.3))';
Cl_w_cg = Moments_w_cg_u(1,:) ./ (q_Corrected' .* (Wing_Area * Span*12));
Cm_w_cg_u = Moments_w_cg_u(2,:) ./ (q_Corrected' .* (Wing_Area * c_bar*12));
Cn_w_cg = Moments_w_cg_u(3,:) ./ (q_Corrected' .* (Wing_Area * Span*12));
Cm_w_cg_corrected = Cm_w_cg_u - Delta_C_m_cg_t';
Corrected_Moment_Coefficients = [Cl_w_cg' Cm_w_cg_corrected' Cn_w_cg'];

%***** Tunnel Correction Data *****
%*****
****

alpha = sample_data(:,1);

```

```

fprintf(' Mach Number Reynolds Number Dynamic Pressure(Psf)|r')
Flight_Parameters
fprintf(' \r');
fprintf(' Loads are in lbf and arranged [D S L] across the top and increments of alpha
down the side |r')
Forces_w'
fprintf(' \r')
fprintf(' Moments are in in-lbf and arranged [L M N] down the side and increments of
alpha along the top |r')
Moments_w_cg_u
fprintf(' \r')
fprintf(' Cl_u      Cd_u |r');
Coefficients
fprintf(' \r')
fprintf(' Del_CD_w   CD_u   CD_Corrected |r');
Compare_CD = [Delta_C_D_w C_D_u' C_D_Corrected]
fprintf(' \r')
fprintf(' Del_alpha_w  alpha_g  alpha_Corrected |r');
Compare_alpha = [Delta_alpha_w' alpha alpha_Corrected ]
fprintf(' \r')
fprintf(' Cl_cg_wind  Cm_cg_corrected_w  Cn_cg_wind |r');
Corrected_Moment_Coefficients
fprintf(' \r')
fprintf(' M#      Re#      q_c      Uoo      alpha_c      C_L      C_D_c
Cl_cg_w      Cm_cg_c_w  Cn_cg_w |r);
YY=[Flight_Parameters (Wind_Speed_Corrected .* (3600/5280)) alpha_Corrected
C_L_u' C_D_Corrected Corrected_Moment_Coefficients]%pressure]
%XX=[M#' Re#' q_c' Uoo' alpha_c' C_L' C_D_c' Cl_cg_w' Cm_cg_c_w' Cn_cg_w
|r];
%*****UNUSED CODE

%ZZ=[XX; YY];
wk1write('output.xls',YY,2,1)

% Max_Cl = max(Coefficients(:,1));

% figure(6);
%
% subplot ('position',[.15 .6 .3 .3]);
% plot(alpha_Corrected,Coefficients(:,1),'b-'); grid on
% legend('30 mph');
% title('\it Flex Wing MAV: C_L_u vs |\alpha'); xlabel('Angle of Attack (\alpha)');
% ylabel('Lift Coefficient (C_L_u)');
%
% subplot ('position',[.65 .6 .3 .3]);
% plot(alpha_Corrected,Coefficients(:,2),'b',alpha_Corrected,C_D_Corrected,'r'); grid on

```

```

% legend('C_D_u', 'C_D_c');
% title('\it Flex Wing MAV: C_D vs \alpha'); xlabel('Angle of Attack (\alpha)');
ylabel('Drag Coefficient (C_D)');
%
% subplot('position',[.15 .1 .3 .3]);
% plot(Coefficients(:,2),Coefficients(:,1),'b',C_D_Corrected,Coefficients(:,1),'r'); grid on
% legend('C_D_u', 'C_D_c');
% title('\it Flex Wing MAV: C_L_u vs C_D'); xlabel('Drag Coefficient (C_D)');
ylabel('Lift Coefficient (C_L_u )');
%
% subplot ('position',[.65 .1 .3 .3])
% plot(Coefficients(:,2),Coefficients(:,1).^2,'b',C_D_Corrected,Coefficients(:,1).^2,'r');
grid on
% legend('C_D_u', 'C_D_c');
% title('\it Flex Wing MAV: C_L_u ^2 vs C_D'); xlabel('Drag Coefficient (C_D)');
ylabel('Lift Coefficient (C_L_u ^2)');

% ****
% ****

%
%
%
% figure(7);
% plot(alpha,Coefficients(:,1),'b.-',...
% alpha,Coefficients2(:,1),'r.:',...
% alpha,Coefficients3(:,1),'k.-',...
% alpha,Coefficients4(:,1),'m.--');
% legend('30 mph (Re_c\approx 130K)', '60 mph (Re_c\approx 260K)', '90 mph
% (Re_c\approx 390K)', '\beta \approx 10\circ'); grid on;
% title('\it C_L vs \alpha', 'FontWeight', 'bold', 'FontSize', 11); xlabel('Angle of Attack
% (\alpha)'); ylabel('Lift Coefficient (C_L)');
%
% figure(8);
% plot(alpha,Coefficients(:,2),'b.-',...
% alpha,Coefficients2(:,2),'r.:',...
% alpha,Coefficients3(:,2),'k.-',...
% alpha,Coefficients4(:,2),'m.--');
% legend('30 mph (Re_c\approx 130K)', '60 mph (Re_c\approx 260K)', '90 mph
% (Re_c\approx 390K)', '\beta \approx 10\circ'); grid on;
% title('\it C_D vs \alpha', 'FontWeight', 'bold', 'FontSize', 11); xlabel('Angle of Attack
% (\alpha)'); ylabel('Drag Coefficient (C_D)');
%

```

```

% figure(9);
% plot(Coefficients(:,2),Coefficients(:,1),'b.-',...
%      Coefficients2(:,2),Coefficients2(:,1),'r.:',...
%      Coefficients3(:,2),Coefficients3(:,1),'k.-',...
%      Coefficients4(:,2),Coefficients4(:,1),'m.--');
% legend('30 mph (Re_c\approx 130K)', '60 mph (Re_c\approx 260K)', '90 mph
% (Re_c\approx 390K)', '\beta \approx 10\circ'); grid on;
% title('\it C_L vs C_D', 'FontWeight', 'bold', 'FontSize', 11); xlabel('Drag Coefficient
% (C_D)'); ylabel('Lift Coefficient (C_L)');
%
% figure(10);
% plot(Coefficients(:,2),Coefficients(:,1).^2,'b.-',...
%      Coefficients2(:,2),Coefficients2(:,1).^2,'r.:',...
%      Coefficients3(:,2),Coefficients3(:,1).^2,'k.-',...
%      Coefficients4(:,2),Coefficients4(:,1).^2,'m.--');
% legend('30 mph (Re_c\approx 130K)', '60 mph (Re_c\approx 260K)', '90 mph
% (Re_c\approx 390K)', '\beta \approx 10\circ'); grid on;
% title('\it C_L ^2 vs C_D', 'FontWeight', 'bold', 'FontSize', 11); xlabel('Drag Coefficient
% (C_D)'); ylabel('Lift Coefficient (C_L)^2');
%
% figure(11);
% plot(REYNOLDS_NUM, MAX_CL,'.-'); grid on
% title('\it C_L _(_M_a_x_) vs Reynolds Number (Re_c )', 'FontWeight', 'bold',
% 'FontSize', 10);
% xlabel('Chord Reynolds Number'); ylabel('Maximum Lift Coefficient (C_L
% _M_a_x_)');
%
% figure(12);
% plot(REYNOLDS_NUM, MIN_CD,'.-'); grid on;
% title('\it C_D_o _(_M_i_n_) vs Reynolds Number (Re_c )', 'FontWeight', 'bold',
% 'FontSize', 10);
% xlabel('Chord Reynolds Number'); ylabel('Minimum Drag Coefficient (C_D
% _M_i_n_)');
%
% figure(13)
% plot(REYNOLDS_NUM, CD_Lam,'.-',REYNOLDS_NUM, CD_Turb,'--'); grid on;
% title('\it C_D_(_S_k_i_n_ _F_r_i_c_t_i_o_n_) vs Reynolds Number (Re_c )',
% 'FontWeight', 'bold', 'FontSize', 10);
% xlabel('Chord Reynolds Number'); ylabel('Drag Coefficient (C_D )');
% legend('Laminar', 'Turbulent');
%
% %figure(14);
% %plot(alpha,Actual_Loads(2,:));
% %title('\it Side Force vs \alpha (60 mph & \beta = 10^o )', 'FontWeight', 'bold',
% 'FontSize', 10');
% % xlabel('Angle of Attack (\alpha)'); ylabel('Side Force (Lb_f )');

```

## Bibliography

1. Aeroelastic Analysis and Optimization on Joined-Wing Configurations. Dir. Dong-Hwan Lee and P. C. Chen. Slide Program. Zona Technology.
2. Bagwill, Tracy L., and Bruce P. Selberg. "Aerodynamic Investigation of Joined Wing Configurations for Transport Aircraft." AIAA 96-2373-CP: 30-41.
3. Bagwill, Tracy L., and Bruce P. Selberg. Aerodynamic Investigation of Twist and Cant Angles for Joined Wing Transport Aircraft. 35th Aerospace Sciences Meeting & Exhibit, 6-10 Jan. 1997. AIAA 97-0037.
4. Bertin, John J. Aerodynamics for Engineers. 4th ed. Upper Saddle, New Jersey: Prentice Hall, 2002. 413-417.
5. Cole, Stanley R. "Divergence Study of a High-Aspect Ratio, Forward Swept Wing." AIAA 86-0009.
6. Corneille, Jennifer. Wind Tunnel Investigation of Joined Wing Configurations. Dept. of the Air Force Air University. Wright-Patterson AFB, Ohio: Air Force Institute of Technology, 1999.
7. Gall, Peter D. "Aerodynamic Characteristics of Biplanes with Winglets." Journal of Aircraft 2nd ser. 24 (1987): 518-522.
8. Guiler, Richard, and Dr. Wade Huebsch. Wind Tunnel Analysis of a Morphing Swept Wing Tailless Aircraft. Applied Aerodynamics Conference, 6-9 June 2005. AIAA 2005-4981.
9. Hixenbaugh, John W. Digital image. [Hotwire Test Pattern]. 2006. Air Force Institute of Technology. 15 Apr. 2006.
10. Hoang, Ty, and Danielle S. Soban. Technology Advancements as Applied to Six Subsonic Transports. Aircraft Design, Systems and Operations Meeting. AIAA 93-3950.
11. Jones, Brent L. Experimental Investigation into the Aerodynamic Ground Effect of a Tailless Chevron-Shaped UCAV. Dept. of the Air Force Air University. Wright-Patterson AFB, Ohio: Air Force Institute of Technology, 2005.
12. Katz, Joseph, Shaun Byrne, and Robert Hahl. "Stall Resistance Features of Lifting-Body Airplane Configurations." Journal of Aircraft 2nd ser. 36 (1999): 471-474.
13. Kress, Robert W. "Variable Sweep Wing Design." AIAA 83-1051: 43-61.

14. Kroo, Ilan, John Gallman, and Stephen Smith. "Aerodynamic and Structural Studies of Joined-Wing Aircraft." Journal of Aircraft 28 (1991): 74-81.
15. Kulhman, J M., and T J. Ku. "Numerical Optimization Techniques for Bound Circulation Distribution for Minimum Induced Drag of Non-Planar Wings: Computer Program Documentation." NASA CR-3458 (1982).
16. Mostaccio, Jason. Digital image. [Placement of Hotwire Anemometer]. 2006. Air Force Institute of Technology. 3 Apr. 2006.
17. Nelson, Robert C. Flight Stability and Automatic Control. 2nd ed. WCB/McGraw-Hill, 1998.
18. Perkins, J N., F M. Cheatwood, R J. Vess, and R A. Wahls. The Design and Testing of Several Joined Wing RPV's. AIAA 23rd Aerospace Sciences Meeting, 14-17 Jan. 1985. AIAA 85-0275.
19. Raymer, Daniel P. Aircraft Design: a Conceptual Approach. 3rd ed. AIAA, 1999.
20. Ron Dupas Collection. 29 Aug. 2002. 4 Apr. 2006  
<<http://1000aircraftphotos.com/Biplanes/1737L.jpg>>.
21. Selberg, B P., and D L. Cronin. Aerodynamic - Structural Optimization of Positive/Negative Stagger Joined Wing Configurations. Aircraft Systems, Design, & Technology Meeting. AIAA 86-2626.
22. Wolkovitch, Julian. Application of the Joined Wing to Cruise Missiles: Final Report for Phase 1. Contract N00014-79-C-0953, Rancho Palos Verdes, CA: Aeronautical Consultant Associates, November 1980 (AD-A096450).
23. Wolkovitch, Julian. The Joined Wing: an Overview. AIAA 23rd Aerospace Sciences Meeting, 14-17 Jan. 1985. AIAA 85-0274.

<b>REPORT DOCUMENTATION PAGE</b>				<i>Form Approved OMB No. 074-0188</i>
<p>The public reporting burden for this collection of information is estimated to average 1 hour per response, including the time for reviewing instructions, searching existing data sources, gathering and maintaining the data needed, and completing and reviewing the collection of information. Send comments regarding this burden estimate or any other aspect of the collection of information, including suggestions for reducing this burden to Department of Defense, Washington Headquarters Services, Directorate for Information Operations and Reports (0704-0188), 1215 Jefferson Davis Highway, Suite 1204, Arlington, VA 22202-4302. Respondents should be aware that notwithstanding any other provision of law, no person shall be subject to an penalty for failing to comply with a collection of information if it does not display a currently valid OMB control number.</p> <p><b>PLEASE DO NOT RETURN YOUR FORM TO THE ABOVE ADDRESS.</b></p>				
1. REPORT DATE (DD-MM-YYYY) 13-Jun-2006		2. REPORT TYPE Master's Thesis		3. DATES COVERED (From – To) Jun 2005 – Jun 2006
4. TITLE AND SUBTITLE  A Wind Tunnel Investigation of Joined Wing Scissors Morphing		5a. CONTRACT NUMBER 5b. GRANT NUMBER 5c. PROGRAM ELEMENT NUMBER		
6. AUTHOR(S)  Dike, Christopher C., Ensign, USN		5d. PROJECT NUMBER 5e. TASK NUMBER 5f. WORK UNIT NUMBER		
7. PERFORMING ORGANIZATION NAMES(S) AND ADDRESS(S)  Air Force Institute of Technology Graduate School of Engineering and Management (AFIT/EN) 2950 Hobson Way WPAFB OH 45433-7765			8. PERFORMING ORGANIZATION REPORT NUMBER  AFIT/GAE/ENY/06-J02	
9. SPONSORING/MONITORING AGENCY NAME(S) AND ADDRESS(ES)  N/A			10. SPONSOR/MONITOR'S ACRONYM(S) 11. SPONSOR/MONITOR'S REPORT NUMBER(S)	
12. DISTRIBUTION/AVAILABILITY STATEMENT APPROVED FOR PUBLIC RELEASE; DISTRIBUTION UNLIMITED.				
13. SUPPLEMENTARY NOTES				
14. ABSTRACT The Air Force Research Laboratory's Munitions Directorate has been looking to extend the range of its small smart bomb. Corneille [6] has conducted tests to determine the aerodynamic characteristics of joined wings on a missile and determine if joined wings are more beneficial than a single wing configuration. The concept of retrofitting wings on the bomb introduced an interesting problem: storage before deployment. This study conducted steady-state low speed wind tunnel testing of a joined wing configuration that morphed from a compact configuration for storage to a full extension. These steady-state tests examine differing sweep angles of the same joined wing configuration. The lift and drag as well as pitching moments and rolling moments were determined and analyzed for the effects of morphing.				
15. SUBJECT TERMS Morphing; Variable Sweep; Extended Range Missile; Wind Tunnel Testing; Joined Wing;				
16. SECURITY CLASSIFICATION OF:  REPORT U		17. LIMITATION OF ABSTRACT  UU	18. NUMBER OF PAGES  128	19a. NAME OF RESPONSIBLE PERSON Milton Franke, Dr. (ENY) 19b. TELEPHONE NUMBER (Include area code) (937) 786-3636, ext 4720; e-mail: Milton.Franke@afit.edu

**Standard Form 298  
(Rev: 8-98)** Prescribed by ANSI Std Z39-18